FORECASTING OF THE ELECTROMAGNETIC WAVES IN IONIZED MEDIA RELATED TO AEROSPACE APPLICATIONS

A THESIS SUBMITTED TO
THE GRADUATE SCHOOL OF NATURAL AND APPLIED SCIENCES
OF
MIDDLE EAST TECHNICAL UNIVERSITY

BY

EMRE ALTUNTAŞ

IN PARTIAL FULFILLMENT OF THE REQUIREMENTS
FOR
THE DEGREE OF MASTER OF SCIENCE
IN
AEROSPACE ENGINEERING

SEPTEMBER 2007

Approval of the thesis:

FORECASTING OF THE ELECTROMAGNETIC WAVES IN IONIZED MEDIA RELATED TO AEROSPACE APPLICATIONS

submitted by **EMRE ALTUNTAŞ** in partial fulfillment of the requirements for the degree of **Master of Science in Aerospace Engineering Department, Middle East Technical University** by,

Prof. Dr. Canan Özgen
Dean, Gradute School of **Natural and Applied Sciences** _______________

Prof. Dr. İ. Hakkı Tuncer
Head of Department, **Aerospace Engineering** _______________

Prof. Dr. Yurdanur Tulunay
Supervisor, **Aerospace Engineering Dept., METU** _______________

Dr. Yıldırım Bahadırlar
Co-supervisor, **Marmara Research Center, TÜBİTAK** _______________

Examining Committee Members:

Assoc. Prof. Dr. Serkan Özgen
Aerospace Engineering Dept., METU _______________

Prof. Dr. Yurdanur Tulunay
Aerospace Engineering Dept., METU _______________

Assoc. Prof. Dr. Altan Kayran
Aerospace Engineering Dept., METU _______________

Assoc. Prof. Dr. Tolga Çiloğlu
Electrical and Electronics Engineering Dept., METU _______________

Dr. Güçlü Seber
Aerospace Engineering Dept., METU _______________

Date: _______________

I hereby declare that all information in this document has been obtained and presented in accordance with academic rules and ethical conduct. I also declare that, as required by these rules and conduct, I have fully cited and referenced all material and results that are not original to this work.

Name, Last Name: EMRE ALTUNTAŞ

Signature :

ABSTRACT

FORECASTING OF THE ELECTROMAGNETIC WAVES IN IONIZED MEDIA RELATED TO AEROSPACE APPLICATIONS

Altuntaş, Emre

MSc., Department of Aerospace Engineering

Supervisor : Prof. Dr. Yurdanur Tulunay

Co-Supervisor : Dr. Yıldırım Bahadırlar

September 2007, 105 pages

The dominant natural electromagnetic (EM) radiation in the extremely low frequency (ELF) range is due to global lightning activity. Radio waves of ELF band traveling along the surface of the ground are able to circle the globe and return to the starting point. Schumann Resonances (SR) are the EM phenomena which occur in the cavity formed by the conducting Earth and the ionosphere, with peak frequencies close to 8, 14, 20, 26 Hz, etc. The spectral characteristics of the SR modes are defined by their resonant mode amplitudes, center frequencies and half-widths. The characteristics of the SR became important in aerospace, marine applications, atmospheric studies, in addition to their relevance to global lightning studies due to their frequency band. The objective of this work is two fold: *(i)* to investigate the characteristics of SR parameters obtained at Şarköy in Turkey; *(ii)* to model the nonlinear characteristics of the Near Earth Space Processes by forecasting the 1^{st} SR mode intensities different time steps in advance using neural network modeling approach. The results show that the SR amplitudes exhibit the characteristics of Tropical African lightning activity and have maxima around 1400 UT. The neural network results show that the proposed model is able to forecast SR amplitudes from 0.5 to 36 hours in advance within reasonable error limits. Furthermore, a fuzzy neural network model with a non–linear optimization algorithm for the

training phase is proposed and tested for the future work.

Keywords: Neural Networks, Signal Processing, Optimization, Electromagnetic Waves, Schumann Resonances

ÖZ

HAVA UZAY UYGULAMALARINDA İLGİLİ ELEKTROMANYETİK
PARAMETRELERİN ÖNGÖRÜSÜ

Altuntaş, Emre
Yüksek Lisans, Havacılık ve Uzay Mühendisliği Bölümü
Tez Yöneticisi : Prof. Dr. Yurdanur Tulunay
Ortak Tez Yöneticisi : Dr. Yıldırım Bahadırlar

Eylül 2007, 105 sayfa

Ekstra düşük frekanstaki doğal elektromanyetik radyasyonun kaynağı evrensel şimşek etkinliğidir. Yer'in yüzeyinde hareket eden düşük frekanslı radyo dalgaları Dünya'nın çervresini dolaşıp başlangıç noktalarına dönebilmektedirler. Schumann Rezonansları (SR), Dünya ile İyonosfer arasındaki boşlukta görülen elektromanyetik bir fenomendir. SR'ların itibari ortalama frekansları, çok az bir günlük değişimle birlikte, $7.8-45$ Hz arasında görülmektedir. SR modlarının spectral özellikleri resonant mod büyüklükleri, merkez frekansları ve yarı-genişlikleri (Q-factor) ile tanımlanır. SR'ların özellikleri evrensel şimşek aktivitesiyle ilişkilerinin yanında ait oldukları frekans bantları nedeni ile havacılık ve uzay ve denizaltı uygulamalarında, atmosfer çalışmalarında ve iletişim endüstrisinde de önem kazanmaktadırlar. Bu tezin amacı *(i)* Türkiye, Şarköy'de ölçülen SR parametreleri'nin özelliklerini araştırmak ve *(ii)* elde edilen 1. SR modunun büyüklüklerini yapay sinirsel ağ modellemesi yöntemleri ile öngörerek Yer'e Yakın Uzay parametrelerinin doğrusal olmayan özelliklerini modellemektir. Elde edilen sonuçlar, SR modlarının evrensel şimşek aktivesiyle uyumlu olduğunu ve saat 1400 ES' de maksimum büyüklüklerine ulaştıklarını göstermiştir. Yapay sinirsel ağ sonuçları uygulanan modelin SR büyüklüklerinin 0.5 saatten 36 saate kadar ilerisinin makul hata limitleri içerisinde öngörebildiğini göstermiştir. Bunun yanında, gelecekteki çalışmalar

için doğrusal olmayan bir optimizasyon algoritması kullanan bir bulanık sinirsel ağ modellemesi ileri sürülmüş ve test edilmiştir.

Anahtar Kelimeler: Yapay Sinirsel Ağlar, Sinyal İşleme, Optimizasyon, Elektromagnetik Dalgalar, Schumann Rezonansları

To my family and Zeynep...

ACKNOWLEDGMENTS

I would like to thank my supervisor, Prof. Dr. Yurdanur Tulunay who has been extremely helpful during the preparation of the thesis.

I would also like to thank Prof. Dr. Ersin Tulunay for his support with his great intelligence and knowledge about the Neural Networks.

I would like to acknowledge Assoc. Prof. Dr. Tolga Çiloğlu with appreciation who gave me important clues about signal processing.

I would also like to acknowledge Dr. Yıldırım Bahadırlar for his kind help and suggestions during the preliminary data analysis.

I would like to thank my friend Tolga Yapıcı and Zeynep Kocabaş for their valuable supports during my graduate work and preparation of this thesis.

I would also like to acknowledge Mr. Erdem Türker Şenalp for his suggestions during the data driven modeling.

This work is partial fulfillment of EU COST 724 Action and TUBITAK.

TABLE OF CONTENTS

APPENDICES

LIST OF TABLES

TABLES

LIST OF FIGURES

FIGURES

LIST OF ABBREVIATIONS

ROMAN SYMBOLS

a	Radius of Earth
c	Speed of light
f_n	Frequency of n^th lateral resonance
F_p	Frequency of p^th transverse resonance
h	Transverse height of Earth–ionosphere cavity
k_n	Wavelength of n^{th} resonance
n	Lateral resonance number
p	Transverse resonance number
$\vec{E}$	Electric field vector
$\vec{H}$	Magnetic field vector
$\vec{D}$	Magnetic induction vector
$X(f)$	Continuous function of frequency f
$x(t)$	Continuous function of time t
$r_x(k)$	Autocorrelation function of discrete signal $x(k)$
$\hat{P}$	Periodogram function
$TANSIG$	Tangent sigmoid function
$PURELIN$	Pure linear function
$\hat{y}$	Estimated value of a function y
y_d	Desired value of a function y
$\mathbf{E}$	Error value
L_i	Lorentzian fit to i^{th} resonance mode
A_i	Amplitude of i^{th} resonance mode

GREEK SYMBOLS

ε_0	Permittivity of space
ε	Permittivity
μ_0	Permeability of space
φ	Geographic latitude
ψ	Geographic longitude
θ	$\varphi - 90^o$
ω	Angular frequency
ϕ	Pay–off function
λ	Lagrange multipliers

SUBSCRIPTS

d	Desired valued
i	Resonance number

CHAPTER 1

INTRODUCTION

The environment surrounding our planet is mostly composed of plasma, ionized gas, a neutral atmosphere, magnetic and electric fields and energetic particles [13]. These media are continuously under the influence of solar effects [13]. The complex dynamical interactions among these media and the generated electric fields in the Near Earth Space create complicated interrelated current systems in the magnetosphere, ionosphere and atmosphere of Earth [13].

The space between our Earth and the Sun is called the "Near Earth Space" (NES). Sun generates electromagnetic (EM) energy and highy energetic particles of millions of degrees. The stream of energetic particles called the "solar wind", accelerate to million kilometers per hour in the NES. These particles create the most critical element of NES, called the "space weather".

1.1 Space Weather

There are more than one definitions of the space weather. As an example, the US National Space Weather Plan defines space weather as "the conditions on the sun and in the solar wind, magnetosphere, ionosphere, and thermosphere that can influence the performance and reliability of space-borne and ground-based technological systems and can endanger human life or health" [14]. The National Oceanic and Atmospheric Administration (NOAA) Space Environment Center (SEC) defines the space weather as "a consequence of the behaviour of the Sun, the nature of Earth's magnetic field and atmosphere" [15]. Space Weather has an enourmous influence on daily lives, mostly on modern telecommunication systems [16].

Dynamic conditions in Earth's space environment, driven by processes on the Sun gives rise to space weather effects [17]. These effects are created by the interaction of the solar wind with the terrestrial magnetic field and plasma environment. Quoting from [17]: "as the utilization of space has become part of our everyday lives, and as our lives have become increasingly dependent on technological systems vulnerable to space weather influences, understanding and predicting hazards posed by the active solar events has grown in importance". The space weather and space sciences added a practical research subject to academic research communities because the rapid time variations in space plasma systems create a hazard to technological systems and humans in space as well as on Earth [17]. For these reasons, we need engineering and life sciences to evaluate the hazards and risks on a variety of technological systems and humans in space, onboard high-altitude aircraft, and on ground [17].

Some examples of services open to Space Weather Effects are: telecommunication, corrosion of pipelines, electrical power line disruption, GSM services, global positioning system (GPS) based services, surveys based on magnetic measurements, hazards for airplane crew and passengers, climatic and metrological effects, risk for astronauts and satellite design. Figure 1.1 shows the effects of solar variability on different branches of engineering and space sciences.

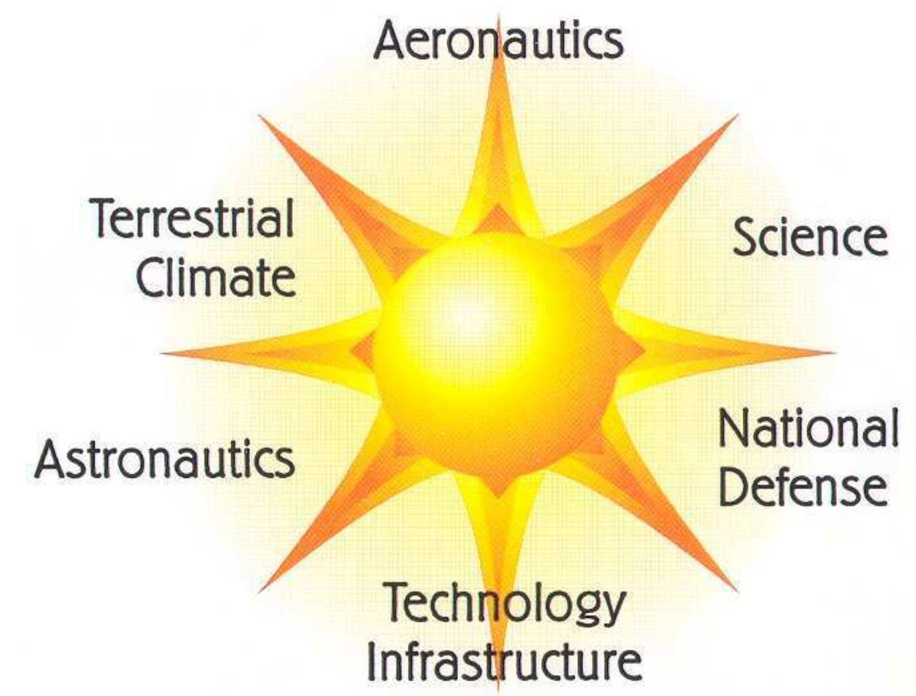

Figure 1.1: Effects of Solar Variability on various research areas [6]

1.2 Earth's Magnetosphere

The neutral atmosphere is composed of mainly neutral gases (up to about 100 km, the major components are N2:O2 in 4:1). Above 100 km, diffusive separation according to mass becomes important and then, layers of atomic gasses are formed.

The Earth is a giant magnet and to a first approximation, the Earth's magnetic field can be represented by the field of a magnetic dipole. The field theoretically is expected to extend for infinity. However, the magnetic field of Sun carried by the solar wind creates interplanetary magnetic field (IMF) and the IMF encounters with the Earth's magnetic field head on at about 60-70 thousand kilometres to the Earth. This interaction interrupts the extension of the Earth's magnetic field as it had been before the merging [17, 18]. Theoretically, when the IMF with southward polarity merges with the northward geomagnetic field, the energy transfer mechanisms from the corpuscular energy (solar wind) into the Earth system is maximum [7, 18, 16]. Consequently, the Earth's magnetic field is confined to a magnetic cavity which is referred as the Magnetosphere [7, 18, 16]. The outer boundary of the cavity is referred as the magnetopause, by analogy with tropopause, stratopause, mesopause, etc.

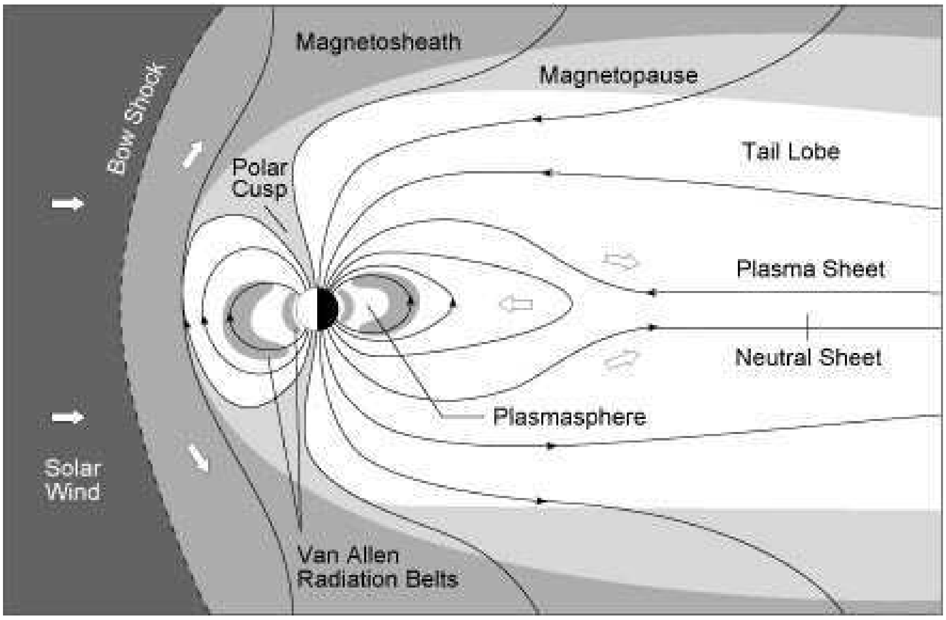

Figure 1.2: Earth's Magnetosphere

1.3 Earth's Ionosphere

Above about 50–60 km of the Earth's surface, the presence of ions and electrons becomes extremely important in determining the chemical or physical properties of atmosphere [7]. This region of the Earth's atmosphere is called *the ionosphere*. Ionosphere is composed of a mixture of thermal and gravitationally bound charge carrier gases [18]. The Ionosphere plays an important part in communication sciences since "every electromagnetic wave is altered during its passage through plasma" [18]. The ionosphere modifies electromagnetic waves, by reflection or refraction, attenuation or rotation of the plane polarization [18].

Ionospheric layers are created by solar radiation ionizing the atmosphere and these layers are identified in terms of the vertical electron density profile. Figures 1.4 and 1.3 show ionospheric layers and the vertical electron density profile of the ionosphere. The sun modulates ionospheric layers and some layers disappear at night and reappear at sunrise. D and F_1 regions disappear at night while E and F_2 layers become much weaker than the day–time. The ionospheric density profile is governed with the density balance equation of Equation 1.1 [18]. In Equation 1.1, n_s is the number density of a gas species s, q_s is the production term, l_s is the loss term and d_s is the transport term. $\overrightarrow{\phi}_s$ is the particle flux and $\overrightarrow{u}_s$ is the velocity carrying the flux.This equation states that, the change in density with time is equal to the density gain by production, minus the density loss by destruction, plus/minus the density gain/loss by transportation [18].

$$\frac{\partial n_s}{\partial t} = q_s - l_s + d_s = q_s - l_s - \nabla \cdot \overrightarrow{\phi}_s = q_s - l_s - \nabla \cdot (n_s \overrightarrow{u}_s) \tag{1.1}$$

In the lower ionosphre the density variations due to transport are negigibly small since the strong friction in the termosphere prevents any independent motion of the charge carriers [18]. During the daytime the change of density with time is small; $\partial n_s/\partial t \rightarrow 0$ and the density reaches its diurnal maximum [18];

$$Daytime: \qquad \frac{\partial n_s}{\partial t} \simeq -l_s$$

During night the production rate is negligibly small [18];

$$Nighttime: \qquad q_s \simeq l_s$$

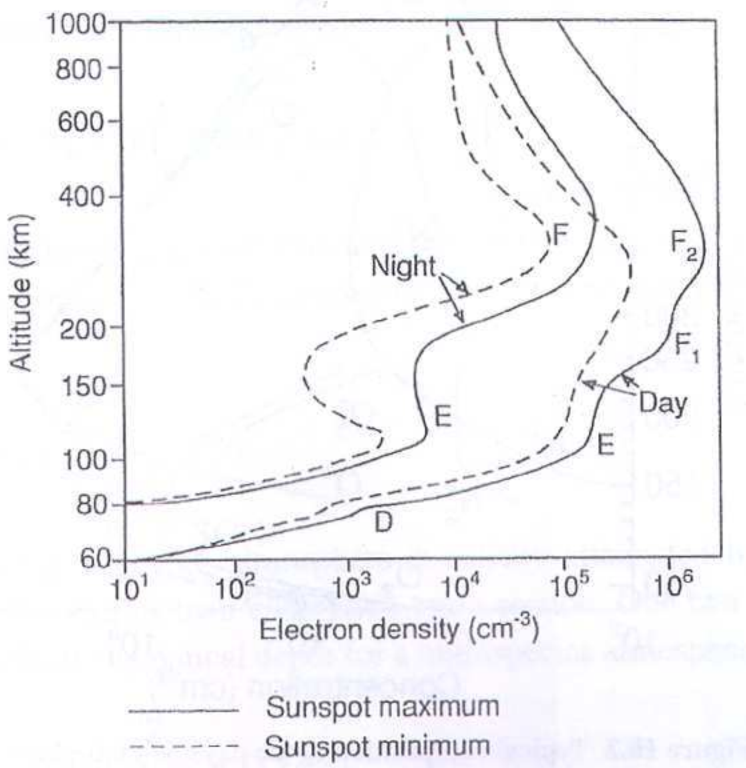

Figure 1.3: Ionospheric electron density profile [7]

Ionosphere and magnetosphere are coupled via magnetic field lines. Magnetospheric electric fields map down to the ionosphere, creating, e.g., plasma convection, frictional heating and plasma instabilities [19]. Particle precipitation ionizes the high latitude atmosphere during nighttime, and heat can be conducted from the magnetosphere down to the ionosphere [19]. In addition, cold ionospheric electrons and ions evaporate into the plasmasphere which can have large effects on some important magnetospheric processes [19].

Since the conductivity of air increases by six orders in magnitude when one enters the region of ionosphere, this layer of atmophere plays an important role in electromagnetic phenomena [1]. The rapid increase in the conducivity enables the lower atmosphere to be treated as a dielectric layer between the conducting Earth and ionosphere. When we think of our planet Earth as a solid conducting sphere covered by a thin dielectric atmosphere, the thickness of the dielectric layer is thin when compared with the radius of the sphere [1]. As a result, the surface of the Earth and the ionosphere create a cavity where radio waves of different

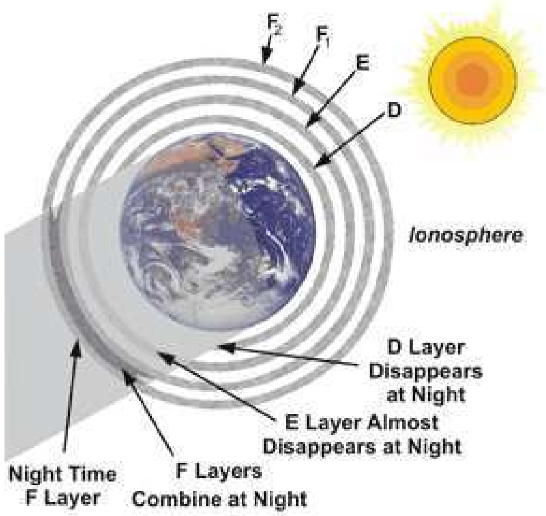

Figure 1.4: Ionospheric Layers [8]

frequencies are guided. These kinds of cavities are called waveguides. When the wavelength of the guided EM wave becomes comparable with the Earth's circumference, that is let the wavelength of a wave be λ and $\lambda = 2\pi a$ approximately equal to a mean radius of earth, then the cavity is called a "resonator" cavity [1]. Recent studies have shown that the source of the transient EM waves in the Earth–ionosphere cavity are the thumderstorm activity and lightning strikes that produce luminious structures in the mesosphere under thunderclouds [1]. Figure 1.5 illustrates the interaction of solar wind with the ionosphere and the ionospheric EM wave propogation.

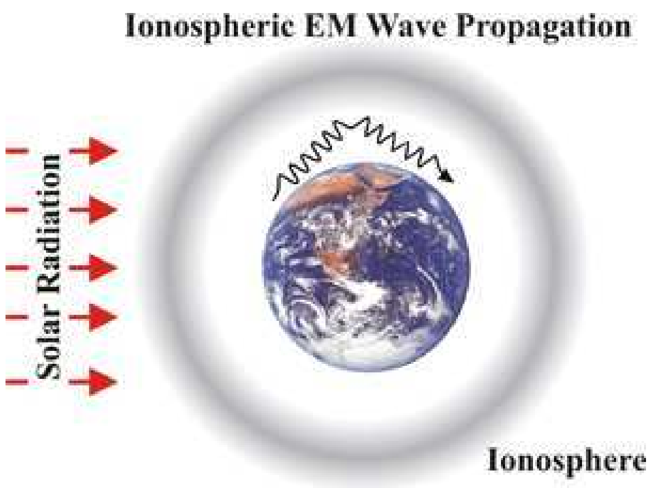

Figure 1.5: Ionospheric EM wave propagation [8]

Figure 1.6 illustrates the sketch of the Earth ionosphere cavity [9]. The sparks in the figure near equatorial Africa indicates the main center of global thunderstorm activity and the arrows indicate the vertical electric field components in the extremely low frequency band [9, 20, 1]. The diagram in the lower part demonstrates the two different kinds of resonances formed in the cavity. The longitudinal dimension of this cavity is $2\pi a = 40Mm$ and the corresponding resonant frequency may be calculated from the condition that the Earth's circumference is equal to wavelength [1];

$$f_n = \frac{c}{2\pi a} = 7.5 \cdot n \quad Hz \tag{1.2}$$

where c is the speed of light, $n = 1, 2, etc.$ is the lateral resonance number and f_n is the frequency of n^th lateral resonance. A radio wave of adequate wavelength can circle the globe in this cavity and return back to its starting point [1].

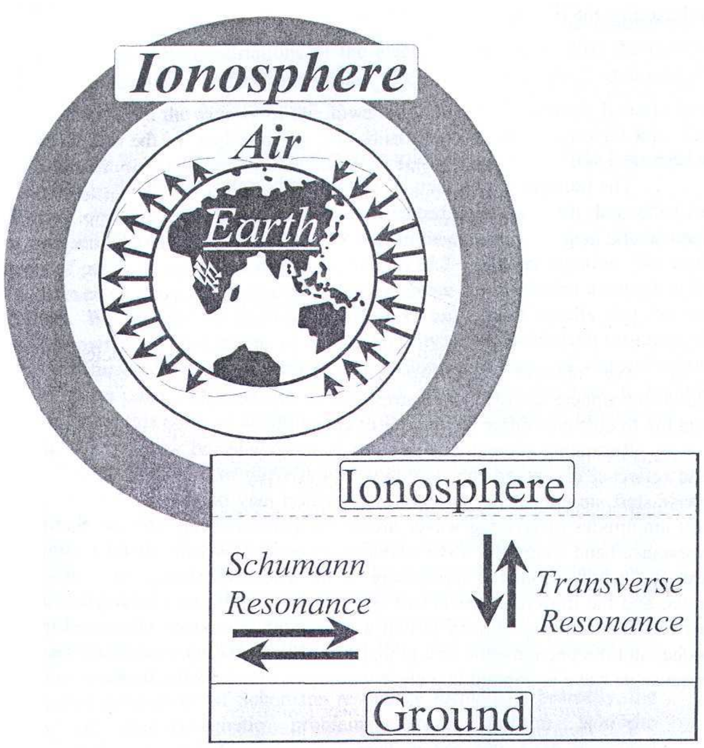

Figure 1.6: Diagram of Earth–Ionosphere cavity. The lower scheme demonstrates two kinds of EM resonance [9]

The transverse height of the Earth–ionosphere cavity, h, is much more smaller ($h/a \simeq 10^{-2}$) and the relevant frequencies are found from a similar demand that the height of ionosphere is equal to integer number of half the wavelength [1].

$$F_p = \frac{c}{2h} p \simeq 2 \cdot 10^3 \cdot p \quad Hz \tag{1.3}$$

Where $p = 1, 2, etc.$ is the transverse resonance number and F_p is the frequency of $p^t h$ transverse resonance. It is to be noted that the two different resonances in the Earth–ionosphere cavity correspond to two different propagation directions.

1.4 Summary

Figure 1.7 shows the space weather effects on our lives. Quoting from [17], "the dynamic processes associated with the solar wind-magnetosphere-ionosphere coupling processes can have significant effects in the near-Earth space environment, in the atmosphere, and on the Earth's surface [21]. As our lives have become increasingly dependent on technological systems that are vulnerable to electromagnetic disturbances and bombardment by energetic electrons and ions, understanding these processes is important both for the design, maintenance and operation of these systems" [17].

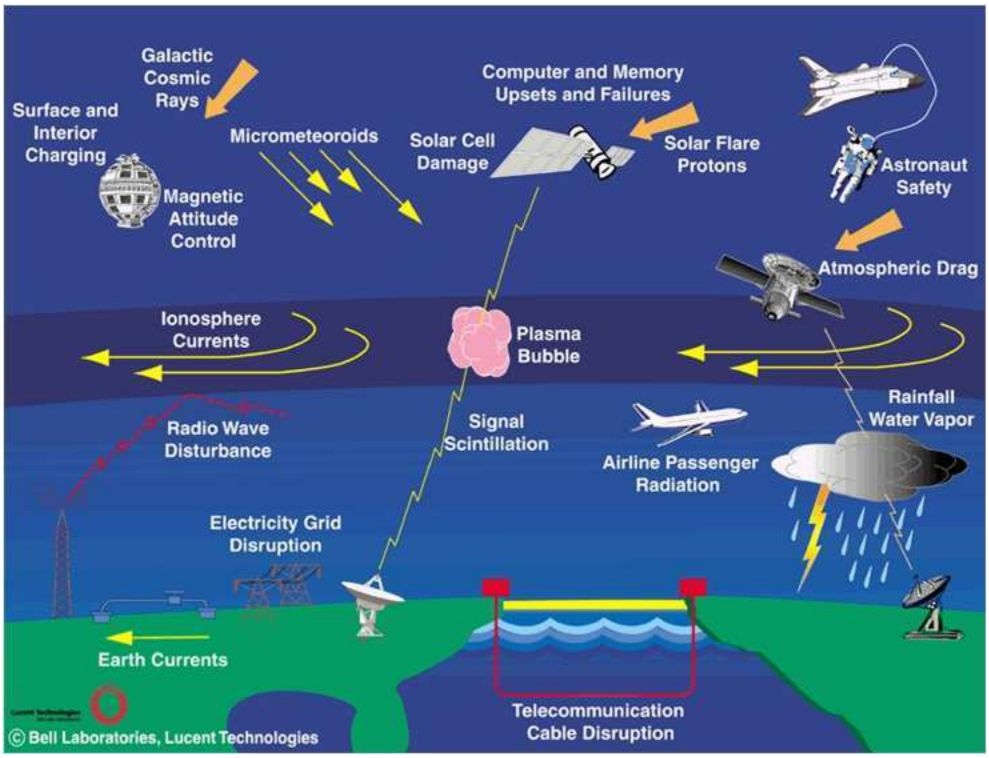

Figure 1.7: Illustration of the chain of events from the Sun to the Earth related to ground-based space weather effects [10]

CHAPTER 2

THEORETICAL BACKGROUND

2.1 Extremely Low Frequency Band

Extremely low frequency (ELF) EM waves (frequencies in the range of 1 Hz to 3kHz) are in interest in science and communication for a number of reasons. The most important one is lightning. Lightning is a powerful natural source of EM radiation in this ELF range and characteristics of lightning can be studied in considerable detail by making measurements of the waves it generates [22]. In communication, the naturally–occurring lightning–generated waves constitute a background noise that can corrupt an ELF communication link [22]. In addition, ELF waves travel with little attenuation to large distances in the space between the Earth's surface and the ionosphere and thus they can provide communication over large regions of the Earth [22]. Moreover, when compared with other higher–frequency modes of EM waves used for communication, ELF waves are relatively unaffected by the ionospheric disturbances and thus can provide a more reliable link of communication during the times of high Solar activity periods [22]. Furthermore, Quoting from [22] "ELF waves penetrate well through conducting materials typically encountered on the Earth's surface and thus they can be used for probing the surface, in prospecting work and for certain forms of communication through the Earth and sea".

2.2 Resonances in the Earth–ionosphere Cavity

As explained in Chapter 1, Earth's surface and the lower wall of ionosphere create a resonator and the atmosphere in between these two layers acts as a dielectric in just like the spherical capacitors. This cavity has resonant frequencies as an analogy to spherical capacitors. The attempt to predict the existence of the resonant waves within the Earth-ionosphere wave guide by Schumann dates back to 15^{th} century [23, 1]. ELF waves at 3 Hz to 300 Hz are propagated as more or less strongly attenuated waves in the space between the earth and the ionosphere, which provides a waveguide for the signals. Certain wavelengths circumnavigate the Earth with little attenuation due to the fact that standing waves are formed within the cavity [1, 20].

The resonant modes of the ELF waves between 1-100 Hz frequency are called Schumann Resonances (SR). The Schumann resonances manifest themselves as spectral peaks in the natural background EM noise levels. Most easily detected are the first 4 modes which occur at roughly 7.8 Hz, 14 Hz, 20 Hz and 26 Hz with slight diurnal variations [2]. Such dominant natural EM radiation in the ELF band or the main excitation source of the SR, is due to the global lightning activity [2, 3]. When a lightning strikes it creates EM waves with different frequencies. Lightning discharges have a "high-frequency component", involving frequencies between 1 kHz and 30 kHz, followed by a "low-frequency component" consisting of waves and frequencies below 2 kHz and gradually increasing amplitude [1]. This produces EM in the very low frequency (VLF) and ELF ranges. Figure 2.1 and Figure 2.2 illustrate the natural cavity and some characteristics and the formation of SR.

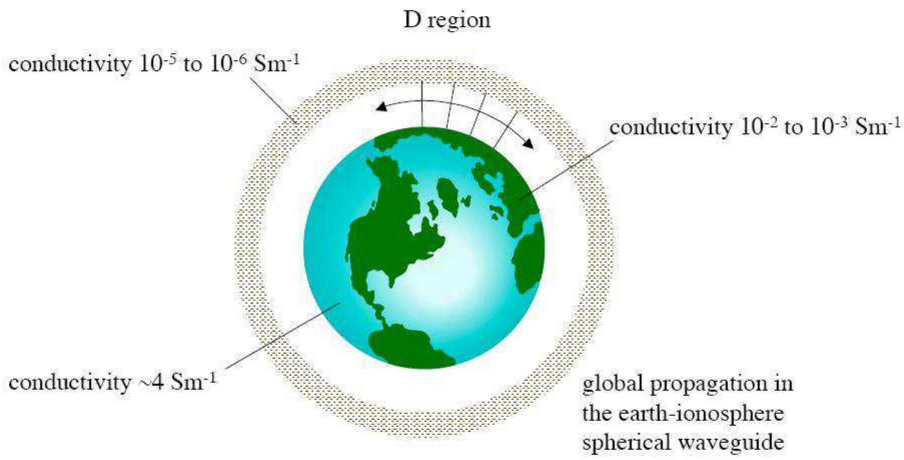

Figure 2.1: Earth-ionosphere waveguide, formation of Schumann resonances [11]

Figure 2.3 shows two important sources contributing to the SR Data. One is the complex interaction of the Earth's ionosphere and magnetosphere with the plasma stream ejected from the Sun (the Solar wind). The other one is the electromagnetic waves that propagate in the Earth-ionosphere cavity from lightning discharges. The two sources provide a rich spectrum of natural electromagnetic fields. Among the other interests to SR, in recent years the SR

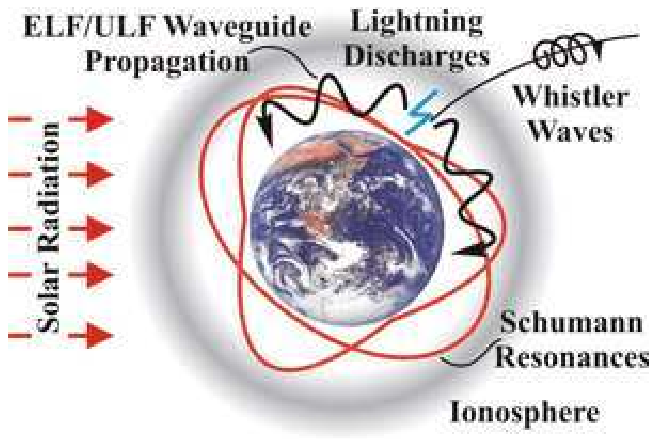

Figure 2.2: Lightning discharges release large amounts of electromagnetic energy into the atmosphere. The resulting electromagnetic waves interact with the earth's magnetic field, and create so called Whistler Waves [8]

have become popular due to the possible connections between the Earth‘s climate and global lightning activity [24, 2, 25, 26]. The characteristics of the SR may be important in aerospace, marine applications or on earthquake predictions in addition to their relevance to global and local lightning studies. For example, for the communication between submerged submarines aircrafts, the ELF band is employed, because, due to their longer wavelengths the attenuation of an ELF wave decreases.

2.3 Basic Formulation

To calculate the resonant frequencies between Earth's surface and ionosphere theoretically one must solve the Maxwell's equations in the coordinate systems give in Figure 2.4 [1]. In figure 2.4, φ denotes the geographic latitude, ψdenotes the geographic longitude, θ is calculated as $\varphi - 90^o$ and r is the distance from the center of the Earth.

$$\nabla \times \overrightarrow{E} = -\mu_0 \frac{\partial \overrightarrow{H}}{\partial t} \tag{2.1}$$

$$\nabla \times \overrightarrow{H} = \frac{\partial \overrightarrow{D}}{\partial t} \tag{2.2}$$

$$\nabla \cdot \overrightarrow{D} = 0 \tag{2.3}$$

$$\nabla \cdot \overrightarrow{H} = 0 \tag{2.4}$$

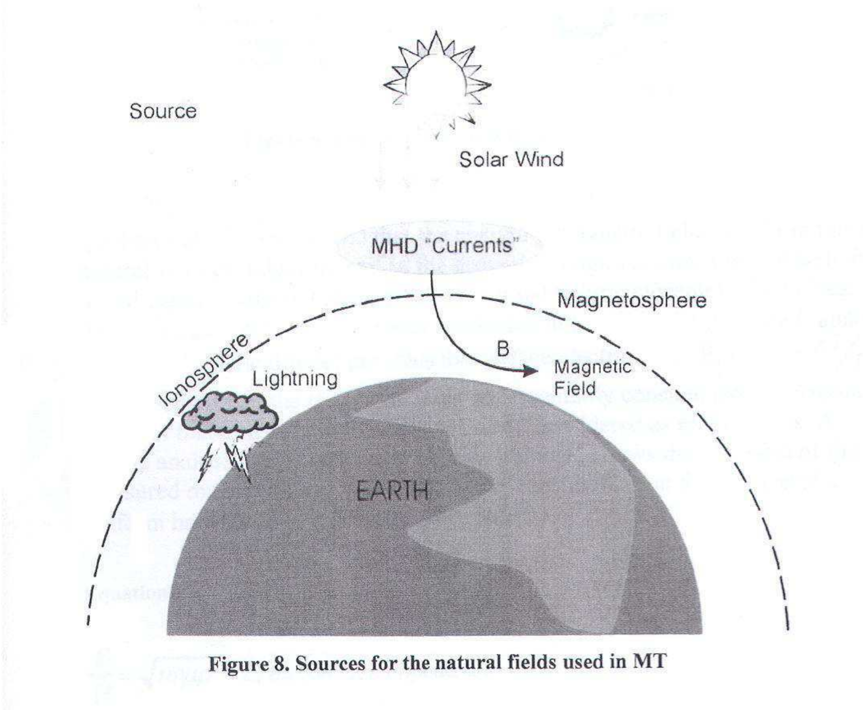

Figure 2.3: Sources for the natural fields [4]

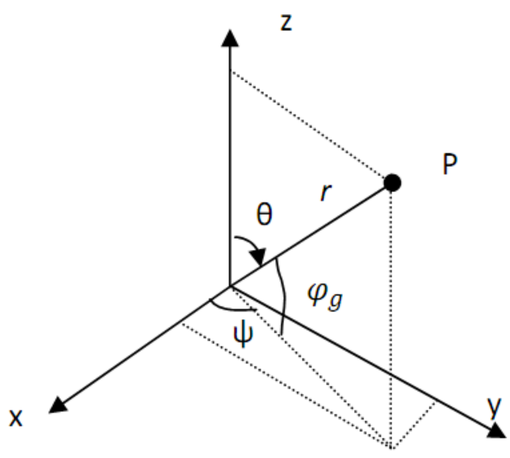

Figure 2.4: Cartesian coordinate systems used in evaluating the Maxwell's Equations

In Equations 2.1 to 2.4, $\overrightarrow{D}$ is the electric induction vector of the form $\overrightarrow{D} = \varepsilon_0 \varepsilon \overrightarrow{E}$. In Equations 2.1 through 2.4, μ_0 is the free space permeability and ε_0 is the free space permittivity. The Equations 2.1 through 2.4 must be solved using the boundary conditions at the Earth and at the ionosphere. The solution of these equations even for the simplest model of ideal spherical cavity is a tedious procedure and is explained in [1]. The boundary conditions at the Earth ($r = a$) for perfectly conducting surface are constructed such that the tangential components of the electric field becomes zero [1];

$$E_\theta(r = a) = E_\varphi(r = a) = 0$$

At the ionosphere, the boundary conditions state that the tangential components of the electric and magnetic fields must be continuous [1].

After solving these equations for an ideal spherical cavity, one finds the equations for characteristic frequencies to be [23];

$$k_n a = \sqrt{n(n+1)} \quad or \quad f_n = \frac{c}{2\pi a} \sqrt{n(n+1)} \tag{2.5}$$

In Equation 2.5, k_n is the wavelength of n^{th} resonance. The resonant frequencies found from this formula are $f_1 = 10.6\ Hz,\ f_2 = 18.3\ Hz,\ f_3 = 25.9\ Hz,\ f_4 = 33.5\ Hz$. One must remember the fact that Equaion 2.5 includes certain assumptions and is only an approximation. For example, as Equation 2.5 is valid for perfectly conducting walls, it only includes the vertical electric field component and horizontal magnetic field component.

In the literature one can find more exact fomulae, such as the one suggested in reference [20];

$$k_n a = \sqrt{n(n+1)\left[1 - \frac{b-a}{a}\right]} \tag{2.6}$$

Equations 2.1 through 2.4 can be solved for more realistic models and combined with the experimental results to end up with more exact formulae. Since the primary aspect of this thesis is to work with the experimental SR data, more detailed explanation on the theoretical SR studies are not given. For more detailed theoretical studies the reader may refer to [1] and [20].

CHAPTER 3

DATA

3.1 Introduction

In this work, SR and ionospheric F2 layer critical frequency (foF2) data are the main data of interest. In addition, 3h-Kp, and some meteorological data are referred in order to complement the objective of the tasks.

The SR data are obtained at the ultra low frequency (ULF)/ELF sites in Turkey. Some meteorological data pertinent to the SR behaviour and foF2 are obtained from the World Data Centers. Throughout this chapter, the main characteristics of the data of interest will be illustrated and the methods of obtaining them will be explained briefly.

3.2 Earth's Magnetic Field (ELF) and SR Data

In recent years many publications have appeared indicating that EM observations in different frequencies may be used as precursors to earthquakes. Following the devastating 1999 earthquake, in 1999, Tulunay, Y., Tulunay, E. and Price C. have taken some initiative and have done the initial work in setting up two ULF/ELF Receiver Stations around the sea of Marmara. The stations were erected in 2004 and the SR data were collected during 2004 and 2005 [27]. The SR data were obtained from the measurements of the geomagnetic field at the Şarköy and Gönen stations via the magnetotellurics method. Figure 3.1 shows exact places of the stations at Şarköy and Gönen on the map of Marmara/Turkey.

Figure 3.1: Map of Marmara/Turkey, showing the stations at Şarköy and Gönen

3.2.1 A Brief Introduction to Experimental Method and the MT24/LF Measurement System [4]

The data were obtained via using the MT24/LF Receiver which uses the magnetotellurics method.

The magnetotellurics (MT) method is a low frequency EM induction method for determining the subsurface distribution of electrical resistivity using measurements of naturally occurring magnetic and electric fields on the surface of the Earth. Natural variations in the Earth's magnetic field induce electric currents (or telluric currents) under the Earth's surface. Concurrent measurements of orthogonal components of the electric and magnetic fields allow the calculation of the impedance tensor [28], which is complex and frequency-dependent. Using this tensor, it is possible to gain insight into the resistivity structure of the surrounding material. The method has been under active development since the 1950's. In the last few years, advances in instrumentation, processing and interpretation have increased the method's use in petroleum exploration, etc. The two souces contributing to SR, as explained in Figure 2.3, are the main elements used in MT method [4].

One of the first observations indicating precursor signals in the ULF range ($f < 1Hz$) were made in California before the Loma Prieta earthquake on 18 October, 1989. Anomalous ULF activity started on 4 October, two weeks prior to the earthquake. Many such measurements have now been made using this method. Although the ULF detectors generally have to be within 50-100 km of the epicenter to receive these anomalous signals, the precursor signals appear days to weeks before the earthquake [27].

The MT24/LF System consists of three sensitive induction coil magnetometers (x,y,z components) together with a data logger for continuous measurements (See Figure 3.2).

MT24/LF Receiver accepts input from the sensors and performs amplification, filtering, power distribution, analog to digital (A/D) conversion and storage of time series.

In general, electrically noisy areas should be avoided when selecting a site for collecting MT data. MT stations should be away from cultural features such as power lines, buildings and roads. Noise from these features can often overwhelm the desired field signals. The result is noisy data.

The minimum distance of the stations from power lines and railroad tracks should be at least 200 meters and distance from buildings (with electric power) and roads with vehicular traffic should be 100 meters. It is possible to collect useful data closer to these sources but the data acquisition time is greatly increased and data quality often suffers.

Sensor sites should be selected in areas sheltered from wind, away from large trees. Even moderate winds can degrade data quality because the motion of sensors and cables in the Earth's direct current (DC) magnetic field induces noise that is not easily differentiated from the signal. The motion of the trees in the wind is another source of noise because trees effectively transfer wind energy to the roots, thereby causing ground motion.

A typical field setup for MT requires two magnetic sensors positioned orthogonally and two electric dipoles, usually but not necessarily, aligned with the magnetic sensors. A sample configuration for MT24/LF is shown in Figure 3.2.

The three sets of x and y positions ensure that the desired data collection would be uninterrupted in case one of the sensors shown in Figure 3.3 fails.

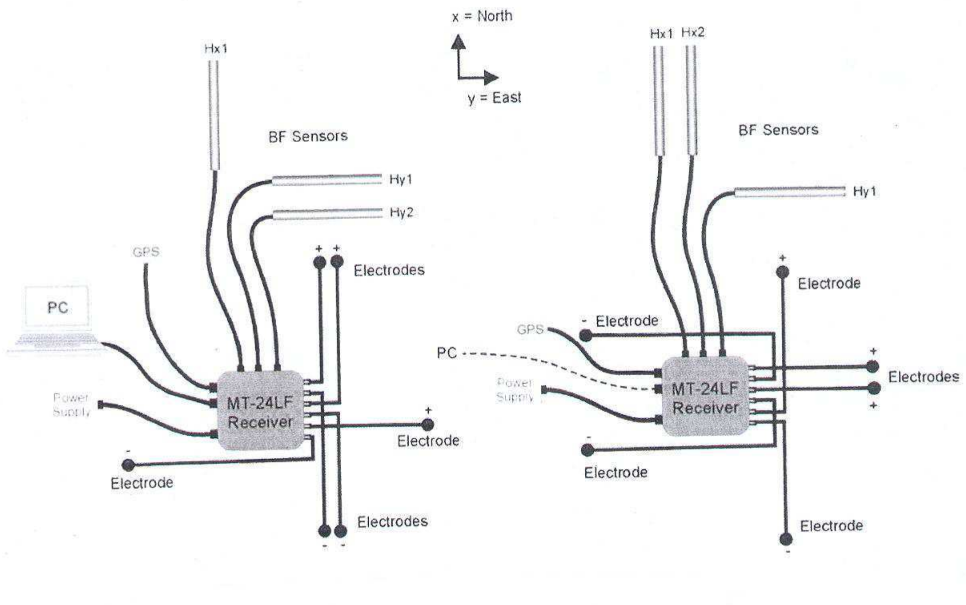

Figure 3.2: Recommended setup for a land-based remote reference station for marine MT [4]

Figure 3.3: Sensors used in the experiment

3.2.1.1 Data Acquisation and Management

The station monitored the three EM components (north–south magnetic [$\overrightarrow{H}_{ns}$], east–west magnetic [$\overrightarrow{H}_{ew}$] and the vertical electric [$\overrightarrow{E}_z$]). However, in this work only the $\overrightarrow{H}_{ew}$ data are employed. The reason behind this selection will be explained in detail in Chapter 5.

The location of the Turkish SR Stations shown in Figure 3.4 and the orientation of the magnetic coils relative to the arrival azimuth of ELF waves indicated that the east–west horizontal magnetic detector is dominated by the lightning sources from Africa mostly [27]. The sampling frequency of the geo–magnetic field data is 100 Hz and the data are recorded every two hour for the period of 5 minutes. The frequency of 100 Hz enabled us to analyze the frequency range of [0,50] Hz, which included the first four SR frequencies of interest.

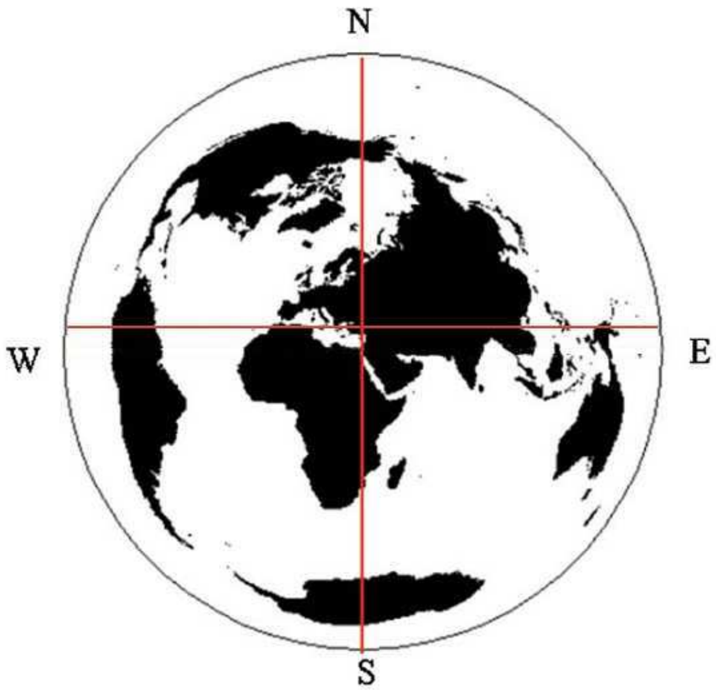

Figure 3.4: Global map showing the experimental site, the direction denotes the great circle path traveled by radio waves originated in different regions of the Earth [2]

The data are originally stored in an internal flash memory on a raw binary data format. These binary files were transfered into ASCII format by employing a simple JAVA program written by Mr. Emre Altuntaş is explained in Appendix A. Finally, the mean of the data is subtracted from all individual datum to end up with a zero mean signal. This procedure will be useful for signal processing applications explained in Chapter 4. Figure 3.5 shows the sample time-domain signal for the station of Şarköy. Then, the data sets have become ready to be studied using some signal processing techniques to calculate the SR characteristic parameters which are resonant mode amplitude, center frequency and half-width [2].

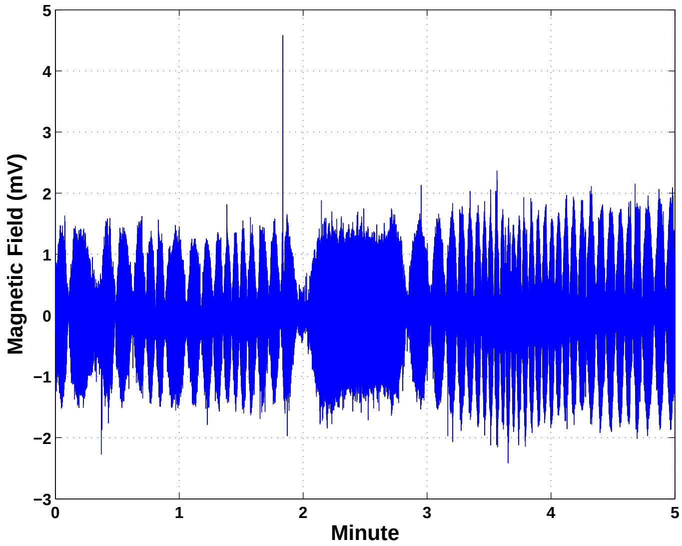

Figure 3.5: (a) Sample geo-magnetic field data in time domain for Şarköy

As an exercise, the author E. Altuntas computed the SR frequencies in terms of the SR mode numbers purely on theoretical gounds for a perfect Earth–Ionosphere cavity. Then, he computed the SR frequencies in mode numbers by using the 1–month long Şarköy (October 2004) data. Figure 3.6 illustrates the SR frequency variations vs. mode numbers *(a)* the theoretical curve; *(b)* from [1] conducted by Nickoloenka et al. based on some experimental data; *(c)* by E. Altuntas based on the Şarköy SR data.

Since, the long-term climate oscillations affecting global lightning activity are reported to be relevant to the main source of the SR, the meteorological parameters are employed [26]. Quoting from the published work of [26], "Tropical lightning activity is closely related to regional continental climatic parameters related to convection: surface temperature, large scale updrafts and upper tropospheric water vapor". "Continental deep-convective thunderstorms transport large amounts of water vapor into the upper troposphere and thereby dominate the variations of global upper-tropospheric water vapor while producing most of the lightning on Earth" [29]. In this work, in particular, the African Tropical Region precipitable water (PW) values for the entire atmospheric column, specific humidity (SH) and relative humidity (RH)

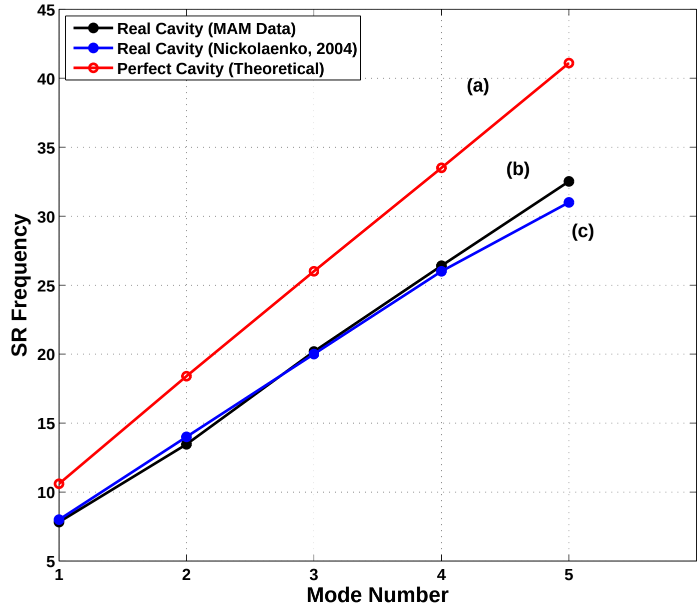

Figure 3.6: Resonance Frequencies for Real and Perfect Cavities

data are employed as relevant data to SR. The meteorological data are National Center for Environmental Prediction (NCEP) Reanalysis data provided by the NOAA/OAR/ESRL PSD, Boulder, Colorado, USA, from NOAA Web site [30].

3.3 Ionospheric F2 layer critical frequency, foF2

The ionosphere is a dynamic system controlled by many parameters including acoustic motions of the atmosphere, electromagnetic emissions, and variations in the geomagnetic field [18, 16, 7]. Because of its extreme sensitivity to atmospheric changes, the ionosphere is a very sensitive monitor of atmospheric events [18, 7].

Ionospheric parameters play essential roles in ionospheric and trans-ionospheric communication and navigation systems including radio propagation in all the frequency ranges. Ionospheric F layer critical frequency, foF2, is a parameter designating the maximum usable frequency in the F2 layer, so it is an important parameter in HF communication. Ionospheric structure and foF2 are highly spatially variable, in addition to diurnal, seasonal and solar-cycle variations [31].

The ionospheric critical frequencies are obtained from the data bases of the world data centers. In particular, the ionospheric stations; Chilton (51^o 06’ N; 1^o 03’ W), Juliusruh (54^o 06’ N; 13^o 04’ E) and Sofia (42^o 07’ N; 23^o 04’ E) are chosen for this work after a search of quantity and quality of the measurements.

3.3.1 The 3 hour K-indices

The K-indices are derived from the maximum fluctuations of horizontal components observed on a magnetometer during a three-hour interval [15]. The K-index quantifies disturbances in the horizontal component of earth’s magnetic field with an integer in the range 0-9 with 1 being calm and 5 or more indicating a geomagnetic storm [15]. Therefore, the magnetic state of the period of data coverage is quantified in terms of the Planetary 3h-Kp indices.

The official planetary Kp index is derived by calculating a weighted average of K-indices from a network of geomagnetic observatories. Since these observatories do not report their data in real-time, various operations centers around the globe estimate the index based on data available from their local network of observatories [32].

Figures 3.7 and 3.8 shows the sample 3h Kp record and foF2 data for 4-28 November 2003 at the Chilton vertical ionosonde (VI) station in order to illustrate that there were magnetically disturbed periods and the foF2 values show the effect of the storms.

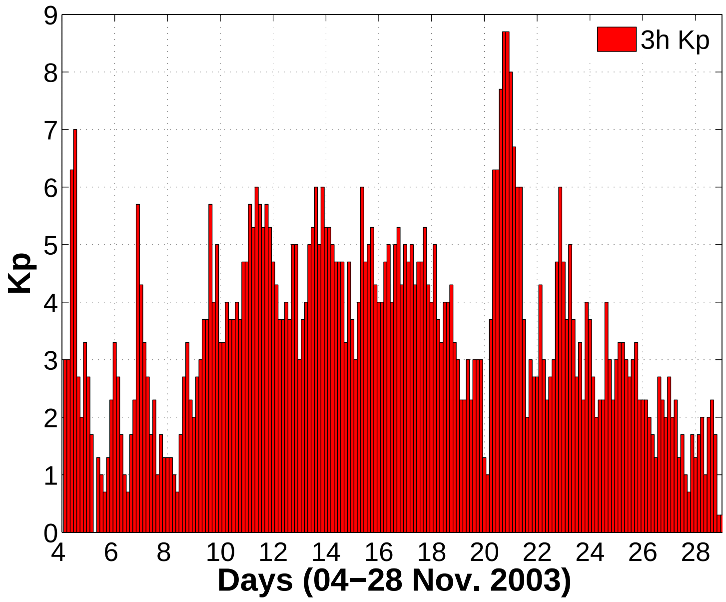

Figure 3.7: 3h Kp indices of Chilton VI station between 4-28 November 2003

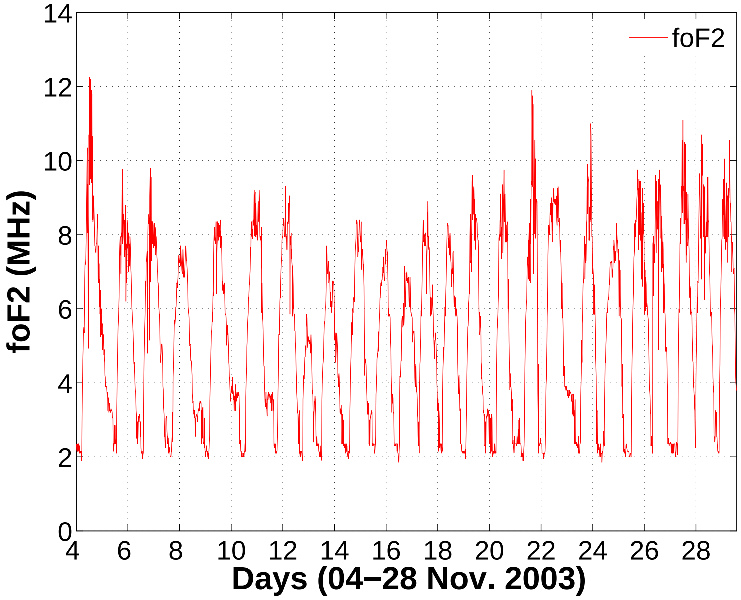

Figure 3.8: 3h foF2 indices of Chilton VI station between 4-28 November 2003

CHAPTER 4

METHOD OF ANALYSIS

In this work, signal processing techniques and data driven modeling techniques are employed in order to analyze the data of interest. In addition, the data driven modeling is confined to the forecasting of SR and the ionospheric critical frequency. The sections below will explain the method of analysis briefly.

The ELF magnetic field components considered in this work are assumed to represent a typical sample of a hypothetical parent population. The ELF data are recorded as electrical signals in terms of voltages. Each data record in time is termed as a signal. In other words, the "signal" means in this context the variation of a physical quantity with respect to one or more independent variable. In this case, it is considered that there is one independent variable, that is time.

4.1 Signal Processing

The signal processing consists of some processing, amplification and interpretation of any signal, and it deals with the analysis and manipulation of signals [33, 34, 35]. Some typical signal types include sound, images, biological signals such as ECG (electro-cardiogram), radar signals, and many others. Processing of such signals includes storage and reconstruction, separation of information from noise (e.g., aircraft identification by radar), compression (e.g., image compression), and feature extraction [5, 33].

Signals can be categorized in various ways. For example, discrete or continuous (see Figure 4.1); random or deterministic, etc. The most common way of making distinction between any two signals is to recognize whether the function representing the signal is defined over a discrete or continuous space. The continuous-time signals are often referred to as continuous signals even when the signal functions are not continuous; an example is a square-wave signal [36].

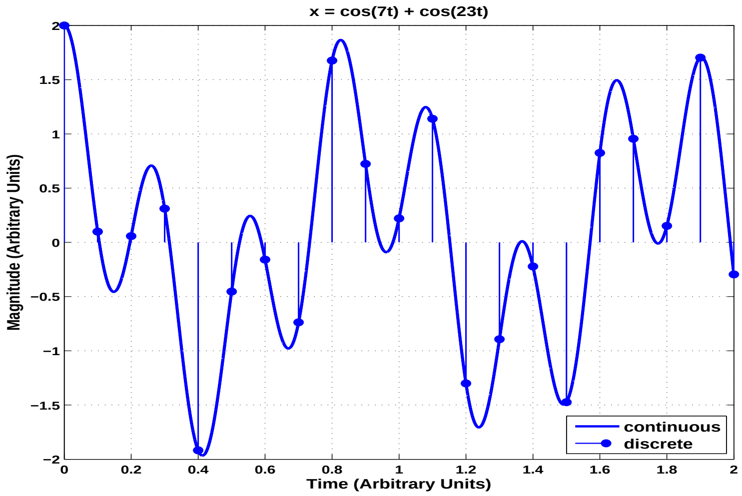

Figure 4.1: The continuous and discrete time signals of function $y = \cos 7t + \cos 23t$

4.1.1 Digital Signal Processing

Digital signal processing (DSP) is the study of signals in a digital representation and the processing methods of these signals [35].

A deterministic signal is a signal that may be reproduced exactly with repeated measurements. A random signal, or random process, on the other hand, that is not repeatable in a predictible way [33].

Natural processes such as the Near-Earth Space **(NeS)** processes are highly complex, nonlinear and time varying. Therefore, looking at its characteristics, the geomagnetic field data may be identified as a discrete time random signal.

The next subsection is the most common technique in dealing with any type of signals, i.e. Fourier Transform.

4.1.1.1 Fourier Transfrom Method

Fourier transform decomposes a function into a continuous spectrum of its frequency components, and the inverse transform combines a function from its spectrum of frequency components [33, 5].

There are several common conventions for defining the Fourier transform of a complex-valued Lebesgue integrable[1] function, x. In communications and signal processing, for instance, it is often the function [37]:

$$X(f) = \int_{-\infty}^{\infty} x(t)\, e^{-j2\pi f t}\, dt, \quad for\ every\ real\ number\ f \tag{4.1}$$

When the independent variable t, represents time (with SI unit of seconds), the transform variable f, represents ordinary frequency (in Hz.). The complex-valued function, X, is said to represent x, in the frequency domain. I.e., if x, is a continuous function, then it can be reconstructed from X, by the inverse transform [37]:

$$x(t) = \int_{-\infty}^{\infty} X(f)\, e^{j2\pi f t}\, df, \quad for\ every\ real\ number\ t, \tag{4.2}$$

4.1.1.2 Discrete Time Fourier Transform Method

Frequency analysis of discrete-time signals and systems provide an important analysis and design tool and often provides insights into the solution of problems that would not otherwise be possible [33]. DTFT is a very powerful tool for analysis of discrete-time signals. The DTFT of a signal $x(n)$ is the complex-valued function of the continuous (frequency) variable, ω, defined by [33];

$$X(e^{j\omega}) = \sum_{n=-\infty}^{\infty} x(n) e^{-jn\omega} \tag{4.3}$$

Since DTFT is a function of a continuous variable, ω, it is not directly applicable to digital computation. For finite length sequences, there is another representation called the *Discrete*

[1] a mathematical construction that extends the integral to a larger class of functions [37]

Fourier Transform (DFT) that is a function of an integer variable, k, is therefore easily evaluated with a digital computer [33]. For a finite-length sequence of *x(n)* of length N, that is equal to zero outside the interval $[0, N-1]$, the $N - point$ *DFT* is [33];

$$X(k) = \sum_{n=0}^{N-1} x(n) e^{-j2\pi kn/N} \tag{4.4}$$

An $N - Point$ (DFT) requires N^2 complex multiplications and $N^2 - N$ complex additions [33]. Therefore, by employing any one of a number of *Fast Fourier Transform (FFT)* algorithms [33], this number can be reduced significantly [33]. Therefore, during the analysis of geomagnetic field data it is reasonable to use *FFT*.

4.1.1.3 Filtering and Windowing

A digital filter is an electronic filter that performs some mathematical operations on a digital signal and filters it. A low pass filter is a filter that passes low frequencies and attenuates frequencies higher than the cut–off frequency. A band-pass filter is a device that passes frequencies within a certain range and attenuates frequencies outside that range. An example of an analogue electronic band-pass filter is an RLC circuit (a resistor-inductor-capacitor circuit). These filters can also be created by combining a low-pass filter with a high-pass filter. Figure 4.2 shows the symbolic representation of a band-pass filter. In this figure f_1 and f_2 represents the lower and upper cutoff frequencies of the filter, while $f_1 - f_2$ will be the frequency bandwidth.

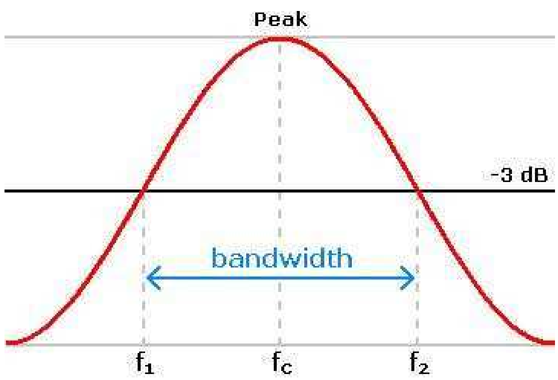

Figure 4.2: A symbolic representation of a band-pass filter

A band–stop filter is the opposite of a band–pass filter. It passes all frequencies but attenuates frequencies in a specific range. A notch filter is a band–stop filter with a narrow range (stopband).

In signal processing, a window function is a function that is zero-valued outside of some chosen interval. For instance, a function that has constant value on an interval and zero elsewhere is called a rectangular window, which describes the shape of its graphical representation. As expected, when another function or a signal (data) is multiplied by a window function, the product is also zero-valued outside the interval specified.

Another example that is employed in this work is the Hamming Window Function. Figure 4.3 shows Hamming window function and its frequency response.

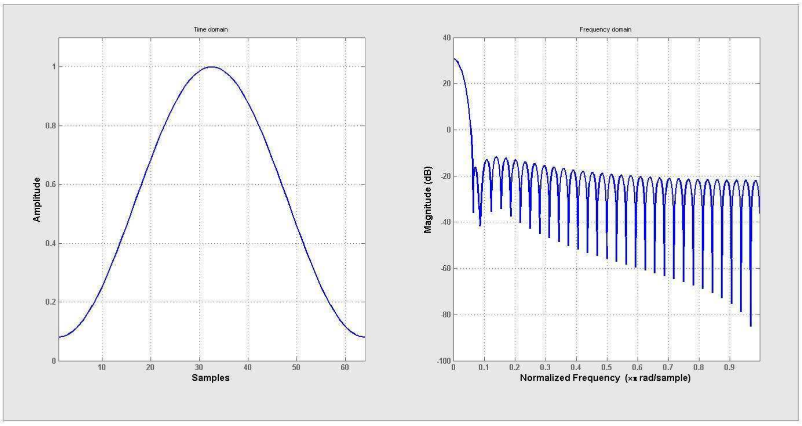

Figure 4.3: The Hamming window and its frequency response

4.1.2 Spectrum Estimation

The power spectrum of a signal represents the contribution of every frequency of the spectrum to the power of the overall signal. Power spectrum analysis of a signal is useful because many signal processing applications, such as noise cancellation and system identification, are based on frequency-specific modifications of signals [33, 34, 35]. Power spectral density (PSD) describes how the power of a signal or time series is distributed with frequency. The power spectral density of a signal exists if and only if the signal is a wide-sense stationary process.

The power spectrum is the Fourier Transform of the autocorrelation sequence for a wide-sense stationary process. Therefore, estimating the power spectrum is equivalent to estimating the autocorrelation. For an autocorrelation ergodic process [33];

$$\lim_{N\to\infty}\left\{\frac{1}{N+1}\sum_{n=-N}^{N} x(n+k)x^*(n)\right\} = r_x(k) \tag{4.5}$$

Thus, if $x(n)$ is known for all n, estimating the power spectrum is straightforward [33].

To calculate the power spectrum of the signal it is possible to use different methods. The approaches for spectrum estimation may me generally categorized into one of two classes; that is, parametric and non–parametric methods.

4.1.2.1 Non-Parametric Methods

Nonparametric methods are those in which the PSD is estimated directly from the signal itself. The most simple method in this category is the periodogram method. An improved version of the periodogram method is known as the Welch's method [33, 34, 38].

The Periodogram: Periodogram method is a special method of estimating the power spectrum by [33];

$$\hat{P}_{per}(e^{j\omega}) = \sum_{k=-N+1}^{N-1} \hat{r}_x(k)e^{-jk\omega} \tag{4.6}$$

Where $\hat{r}_x(k)$ is the estimated autocorrelation sequence [33]. It is clear that the periodogram is proportional to the squared magnitude of signal's discrete time Fourier Transform (DTFT).

Welch's Method: The Welch method [38], splits a set of data into smaller sets of data and calculates the modified periodogram (the power spectrum) of each set, which produces an array of power measurements vs. frequency [33]. Welch's method is succeeded in two steps:

- The modified periodogram is calculated by applying a window function to the time-domain data, computing the discrete Fourier transform, and then computing the squared magnitude of the result.

- Quoting from [33] “most window functions afford more influence to the data at the center of the set than to data at the edges, which represents a loss of information. To mitigate that loss, the individual data sets are commonly overlapped in time” [33].

The individual periodograms are then time-averaged, which reduces the variance of the individual power measurements.

4.1.2.2 Parametric Methods

Parametric methods are those which are based on using a model for the process in order to estimate the power spectrum [33]. In this work, the Yule-Walker autoregressive (AR) method is employed as an example to parametric methods. Parametric methods estimate the PSD by first estimating the parameters of a linear system that hypothetically “generates” the signal [33]. They produce better results than classical non–parametric methods when the data length of the available signal is relatively short [33].

As mentioned before, parametric methods are those which are based on using a model for the process in order to estimate the power spectrum [33]. The most commonly used linear system model for the signal is *the all-pole model*, “a filter with all of its zeroes at the origin in the z-plane” [33]. The output of such a filter for white noise input is an AR process. For this reason, these methods are sometimes referred to as AR methods of spectral estimation [5].

During this thesis to model the geomagnetic field signal, and *“all-pole modeling using autocorrelation method”* is employed, therefore a brief introduction to these methods are presented herewith.

The autocorrelation method finds the poles of the model by minimizing the error;

$$\varepsilon = \sum_{n=0}^{\infty} \left|e(n)\right|^2$$

The normal equations and the minimum error for the autocorrelation method are [33];

$$\sum_{i=1}^{p} a_p(l) r_x(k,l) = -r_x(k) \; : \; k = 1, 2, \ldots p$$

$$r_x(k,l) = \sum_{n=p}^{N} x(n-l)x^*(n-k) \; : \; k,l \geq 0$$

$$\epsilon_p = r_x(0) + \sum_{k=1}^{p} a_p(k) r_x^*(k)$$

Where a's are the poles of the model.

Autoregressive Spectrum Estimation: All AR methods yield a PSD estimate given by [35, 33, 5];

$$\hat{P}_{AR}(f_s) = \frac{1}{f_s} \frac{\varepsilon_p}{\left| 1 + \sum_{k=1}^{p} \hat{a}_p(k) e^{-2\pi jkf/f_s} \right|}$$

Yule-Walker Method: The Yule Walker Method estimates AR spectrum of a signal using autocorrelation method. Quoting from [33, 5], "the Yule-Walker AR method of spectral estimation computes the AR parameters by forming a biased estimate of the signal's autocorrelation function, and solving the least squares minimization of the forward prediction error". This results in the Yule-Walker equations [34, 35];

$$\begin{bmatrix} r(1) & r(2)^* & \cdots & r(p)^* \\ r(2) & r(1) & \cdots & r(p-1)^* \\ \vdots & \ddots & \ddots & \vdots \\ r(p) & \cdots & r(2) & r(1) \end{bmatrix} \begin{bmatrix} a(2) \\ a(3) \\ \vdots \\ a(p+1) \end{bmatrix} = \begin{bmatrix} -r(2) \\ -r(3) \\ \vdots \\ -r(p+1) \end{bmatrix}$$

The Yule-Walker equations can be solved efficiently via Levinson's algorithm [5]. Yule Walker Method performs as well as other methods for large data records and always produces a stable model [35]. However, in Yule-Walker Method there is a frequency bias for estimates of sinusoids in noise [34].

4.2 Data Driven Modeling

Near-Earth Space processes including the Space Weather are highly complex and non-linear. Therefore, mathematical modeling based on first physical principles is usually difficult or impossible. For such cases data driven modeling methods are recommended to be used in parallel with mathematical modeling approach [39]. It was demonstrated by previous works of Tulunay Y. and Tulunay E. [12, 40, 39] that data-driven (data based) modeling such as Neural Network (NN) based approach when used with mathematical modeling, has advantages in dealing with highly non-linear processes in the Near-Earth Systems. In this work, various data driven modeling techniques are used and explained below.

4.2.1 Artificial Neural Network (ANN) Modeling

An artificial neural network is a system of interconnected computational elements operating in parallel, arranged in patterns similar to biological neural nets and modeled after the human brain [41]. The earliest roots of the parallel distributed processing can be found in the works of neurologists [42, 43]. Neural network research has been popular since 1960s. However, since 1990's, interest in this field has increased mainly because of the developments in very large scale integrated circuit technology, optical devices and new learning paradigms which make rapid and inexpensive implementation possible [44]. Neural Networks (NN) are finding applications in various fields including adaptive pattern recognition, adaptive signal processing, adaptive dynamic modeling, adaptive control, optimization, expert systems and Earth System Science modeling applications. Some other specific applications include the control of robot arm, diagnosis and numeric to symbolic conversion [45].

A general exposition of NN's was given in [40]. A neuron is an information processing unit consisting of connecting links, adder and activation function. The adder is for summing bias and the input signals weighted in neuron's connecting links. It follows an activation function for limiting the amplitude of the neuron's output [44].

Neural computing is an alternative to programmed computing which is a mathematical model inspired by biological models. This computing system is made up of a number of artificial neurons and a huge number of interconnections between them [46]. According to the structure of the connections, we identify different classes of network architectures.

In feedforward neural networks, the neurons are organized in the form of layers. The neurons in a layer get input from the previous layer and feed their output to the next layer [46]. In this kind of networks connections to the neurons in the same or previous layers are not permitted [46]. The last layer of neurons is called the output layer and the layers between the input and output layers are called the hidden layers. The input layer is made up of special input neurons, transmitting only the applied external input to their outputs [46, 44]. In a network if there is only the layer of input nodes and a single layer of neurons constituting the output layer then they are called single layer network. If there are one or more hidden layers, such networks are called multilayer networks [46].

The structures, in which connections to the neurons of the same layer or to the previous layers are allowed, are called recurrent networks [46]. For a feed-forward network always exists an assignment of indices to neurons resulting in a triangular weight matrix [46, 44]. Furthermore if the diagonal entries are zero this indicates that there is no self-feedback on the neurons [46, 44]. However in recurrent networks, due to feedback, it is not possible to obtain a triangular weight matrix with any assignment of the indices [46, 44]. The general representation of feed-forward and recurrent neural networks are given in Figure 4.4.

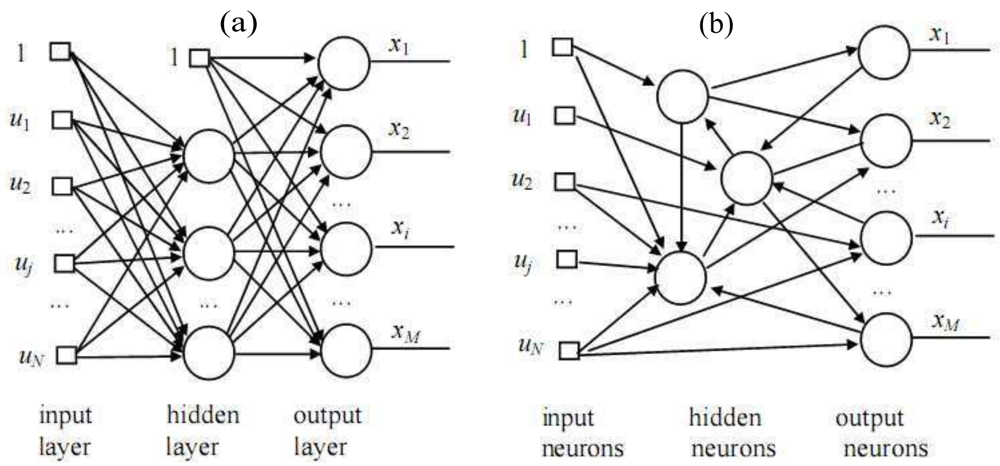

Figure 4.4: (a) Layered feedforward neural network (b) Non–layered recurrent neural network [46]

One of the neural network models used in this work, the METUNN, is a feed-forward NN with one hidden layer, using a Levenberg Marquadt Backpropagation algorithm with validation stop during the training process. Validation stop procedure is integrated into the model to prevent memorization by terminating the training process when the gradient of validation set error becomes zero and the validation error is about to increase [45].

The METUNN Model, has got one input layer, one hidden layer and one output layer. The activation function of the hidden layer is the hyperbolic tangent sigmoid function as given in Eqnuation 4.7 , and the transfer function of the output layer is linear as given in Equation 4.8 [12]. Figure 4.5 shows the general representation of METUNN model.

$$f^1(n) = TANSIG(n) = \frac{2}{1 + e^{-2 \cdot n}} + 1 \tag{4.7}$$

$$f^2(n) = PURELIN(n) = a \cdot n \tag{4.8}$$

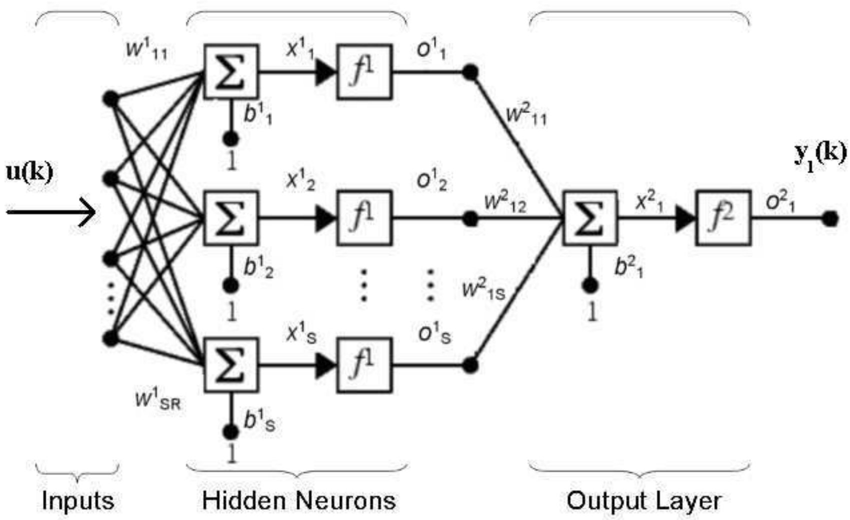

Figure 4.5: General representation of METUNN model [12]

In order to improve the contribution of initial parameter selection to learning convergence and system performance, a new parameter initialization, or initialization of layer weights, method was integrated to the METUNN model. This new procedure is almost the same as that of [47]. The underlying idea that [47] used is to initialize the parameters of the network so that all activation functions can always be operated in an active region. Quoting from [47] “Since the derivative of activation functions within the active region has a more significant change than the one in the saturation region, it is highly possible to rapidly reach a local minimum for parameter optimization algorithms. In addition, the initialized parameters can prevent the network from getting stuck in the beginning of the training phase. Such an initialization algorithm yields faster training, and prevents the network from getting stuck in the beginning of the training phase and guides the training algorithm to search particular regions of the parameter space” [47].

4.2.2 Fuzzy Neural Network Modeling

An attempt to combine the computational power of neural networks with the inference attributes of the fuzzy logic systems has led to the fuzzy neural network (FNN), an intelligent tool where expert knowledge is incorporated in the form of IF-THEN rules [48].

The fuzzy neural network model used in this work consists of two parts, the feedforward neural network part and the fuzzy inference part. Figure 4.6 shows the general structure of the whole system (fuzzy neural network).

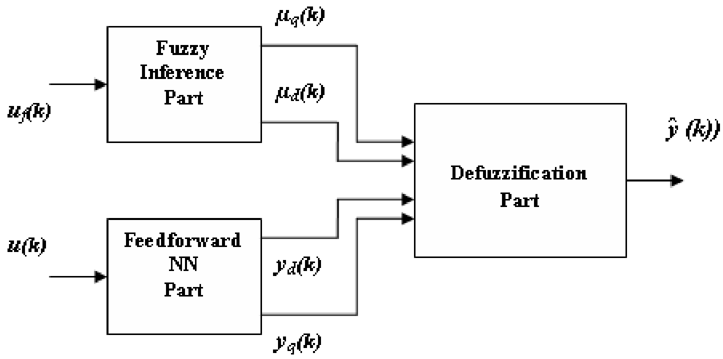

Figure 4.6: General representation of the fuzzy neural network

The fuzzy inference part of the model simply gives the firing strength of each IF-THEN rule which are used to divide the input/output space into several sub-clusters. The fuzzy rules and the membership functions may be found by various clustering methods or by expert information. Clustering is used for the cases when it is not exactly known how many clusters there should be for a given set of data [48, 49]. For this work the author had used Mamdani type of fuzzy rules which is one of the most common types. In Mamdani type of fuzzy rules, there is a fuzzy set for each output variable that needs defuzzification [50, 5].

The whole model can be divided into three major parts: the premise, the consequent and the defuzzification part, as shown in 4.6. The premise part implements the algebraic product conjunction in [51], providing the rule firings [48, 49]. The premise partition is determined either by the expert, based on prior knowledge about the system being modeled or using a data-driven clustering method [48, 49]. The defuzzification part implements the defuzzification routine [52]; it combines the rule firings and the outputs of the recurrent sub-models of the rules, and produces the overall output of the fuzzy model at each time instant.

After getting the individual neural network outputs and the firing strength of the neural networks, the defuzzified output of the whole model is calculated by weighted averages;

$$\hat{y}(k) = \frac{\sum_{l=1}^{r} \mu_l(k) \cdot \hat{y}_l(k)}{\sum_{l=1}^{r} \mu_l(k)} \tag{4.9}$$

4.3 Training and Optimization Algorithms

The next step in modeling is the training phase and the identification of an optimization algorithm for the system.

The optimization algorithm employed is a constrained optimization algorithm for dynamically driven fuzzy neural networks, namely FUNCOM (Fuzzy Neural Optimization Method), which is adapted from [49]. The FUNCOM method aims at transforming the learning process to a constrained optimization problem, using methods based on optimal control theory and the calculus of variations [48]. Quoting from [48, 49], "in this algorithm, the training task is formulated as a constrained optimization problem, whose objective is twofold: (i) minimization of an error measure, leading to successful approximation of the input-output mapping and (ii) optimization of an additional functional, which aims at formulating suitable internal representations of the fuzzy model. The detailed explanation of the method can be found in [48] or [49], however, in short, in this algorithm, one tries to minimize the relative mean square error function [48];

$$\mathbf{E} = \frac{1}{k_f} \sum_{k=1}^{k_f} [\hat{y}(k) - y_d(k)]^2 \tag{4.10}$$

and on the other hand tries to optimize another function, called *the pay-off function* [48],

$$\phi = (\theta - \theta_{cur})^T (\theta_{cur} - \theta_{prev}) \tag{4.11}$$

where θ is defined as the control vector; $\theta = [\mathbf{w_1^T w_2^T w_3^T w_4^T w_5^T w_6^T} ...]^{\mathbf{T}}$, holding all the weights and biases. Again the details may be found in [48] and [49], but in short, at each epoch the parameters are updated by the following formula [48, 49];

$$d\theta = \mathbf{\Delta^2} \sqrt{\frac{I_{EE} - (\delta E)^2}{I_{\Phi\Phi} \cdot I_{E\Phi}^2}} \cdot [\mathbf{\Delta_\Phi^T} - \mathbf{\Delta_E^T} \frac{\mathbf{I_{E\Phi}}}{\mathbf{I_{EE}}}] + \mathbf{\Delta^2 \Lambda_E^T} \frac{\mathbf{\delta E}}{\mathbf{I_{EE}}} \tag{4.12}$$

where [48];

$$\Lambda_\Phi = \frac{\partial \Phi}{\partial \theta},\ \Lambda_E = \lambda^T \cdot \frac{\partial f}{\partial \theta}$$

$$I_{EE} = \Lambda_E \Delta^2 \Lambda_E^T,\ I_{\Phi\Phi} = \Lambda_\Phi \Delta^2 \Lambda_\Phi^T,\ I_{E\Phi} = \Lambda_\Phi \Delta^2 \Lambda_E^T$$

and [48];

$$\delta E = -\xi \cdot \sqrt{I_{EE}}$$

Finally, λ are the Lagrange Multipliers determined below and ξ is a constant over [0, 1]. Having calculated the corrective $d\theta_i$ terms, the consequent parameters are updated as follows [48, 49]:

$$\theta(t+1) = \theta(t) + d\theta \tag{4.13}$$

where, t represents the index of the epoch. The Lagrange multipliers are determined through the recursive equations [48, 49]:

$$\lambda^{\mathbf{T}} = [(\lambda^{\mathbf{1}})^{\mathbf{T}}\ (\lambda^{\mathbf{2}})^{\mathbf{T}}] \tag{4.14}$$

$$\lambda_l^2(k) = \frac{2}{k_f} \cdot [y(k) - y_d(k)] \cdot \frac{\mu_l(k)}{\sum_{i=1}^r \mu_i(k)} + \sum_{j=1}^{Oy_2} \left[\lambda_l^2(k+j) \cdot f_2\prime(k+j) \cdot w_j^{5(l)}\right] \tag{4.15}$$

$$\lambda_{li}^1(k) = \sum_{j=1}^{Oy_1} \left[\lambda_{li}^2(k+j) \cdot f_1\prime(k+j) \cdot w_{ij}^{2(l)}\right] + \sum_{q=0}^{Oy_3} \left[\lambda_l^2(k+q) \cdot f_2\prime(k+q) \cdot w_{iq}^{4(l)}\right] \tag{4.16}$$

(4.17)

The equations above are solved by backward differences using the boundary conditions given in [49].

Once the stepsize is found, the whole procedure is repeated again and at the end the optimum is reached by using a derivative criteron or maximum number of iteration criteron [48, 49].

In this work all these methods have contributed to the results which are presented in the next chapter.

CHAPTER 5

RESULTS OF ANALYSIS

In this chapter, the results based on the “spectral signal processing” and “data driven modeling” will be presented.

The SR power amplitudes of the first four modes, 8, 14, 20, 26 Hz are studied by using spectral estimation, signal modeling and curve fitting techniques.

Then the data driven models, in particular, the neural networks (NN) and neural fuzzy models (NFN) are employed. The results of the forecast of the SR power amplitudes and the forecast of ionospheric critical frequencies will be presented in order to demonstrate the methods and techniques which can be used successfully in characterization of the aerospace medium at this different frequency bands of communication. That is the SR at ELF, the foF2 at HF ranges.

5.1 Preliminary Statistical Analysis of the Şarköy and Gönen SR data

The initial objective of this work is to make use of all the ELF data returned by two stations, Gönen and Şarköy on the coasts of Sea of Marmara, Turkey. Therefore, the task had started by a preliminary statistical data analysis of the ELF data in order to achieve the quality and quantity of useful data to be used for this work.

The normal background levels of natural ULF and ELF EM waves in the atmosphere are from 10^{-12} T (pT) to 10^{-9} T (pT). If the background noise levels from power lines, motors, factories, traffic, trains, etc. is high, the natural signal gets buried in the noise and it will be very difficult to monitor the natural signals. However, the anthropogenic noise travels many kilometers, and the sources of possible noise cannot always be seen with eyes.

For this reason, some technical instruments were brought to the experimental sites to investigate the background noise levels at the sites [27]. The sampling frequency of 250 Hz, while performing these experiments allows one to observe frequencies up to 125 Hz. Then the spectral measurements are processed with two different preamplifiers, each with a different frequency response and different filters, the first with a low pass filter (LPF) and the other with only a notch (N) filter.

Figures 5.1 and 5.2 show the spectral results for the site in Gönen. The site is a military vacation site which is on the waterfront, and only has vacationers during summer months of the year. As seen in the Figures 5.1 and 5.2, 100 Hz signal at the station is quite large, relative to the 50 Hz signal for both the LPF and N filters.

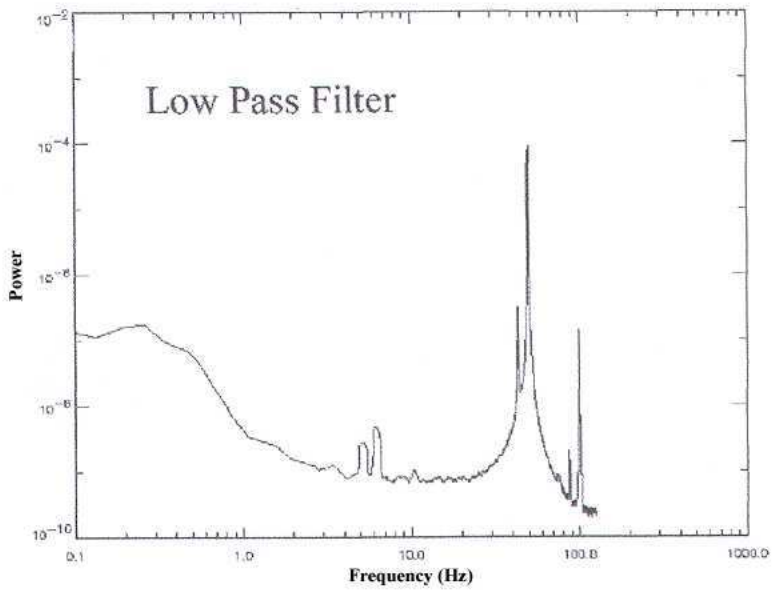

Figure 5.1: The spectral measurements at the experimental site in Gönen using a LP filter

At the site in Şarköy, 50 Hz magnetic field intensity is found to be 15.2 nT, while the electric field density was 1.45 V/m [27]. The spectra for the experimental site are shown in Figures 5.3 and 5.4. With the LPF, the background signals appear to be low relative to the site in Gönen. Furthermore, the 100 Hz signal is much more smaller relative to the 50 Hz signal, compared to the site in Gönen. Using the notch filter shows only a relatively large 35 Hz signal. Both spectra show some source of noise around 10 Hz.

The preliminary experiments done at the sites show that the data from the Şarköy station is better than that of Gönen from quality considerations. Observations and experimental mea-

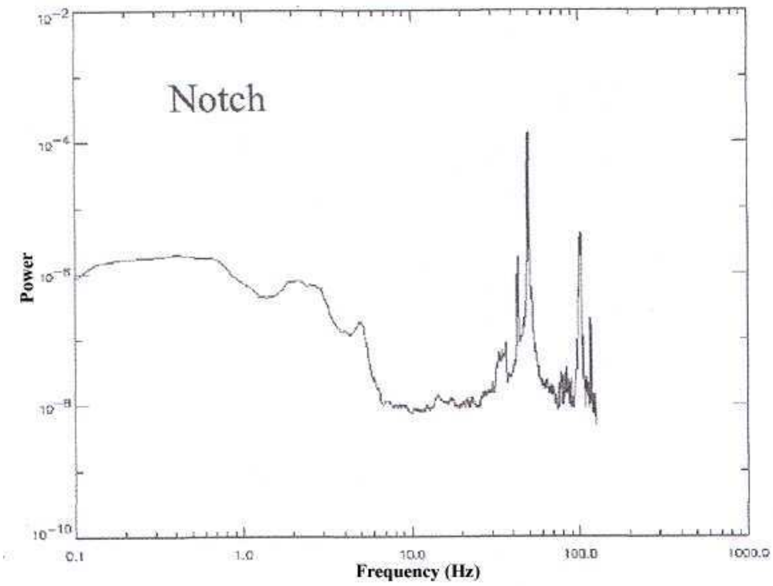

Figure 5.2: The spectral measurements at the experimental site in Gönen using a N filter

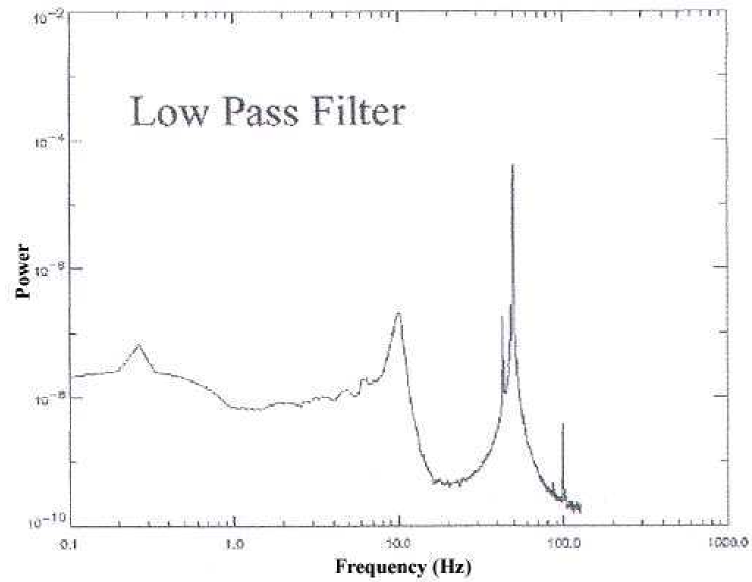

Figure 5.3: The spectral measurements at the experimental site in Şarköy using a LP filter

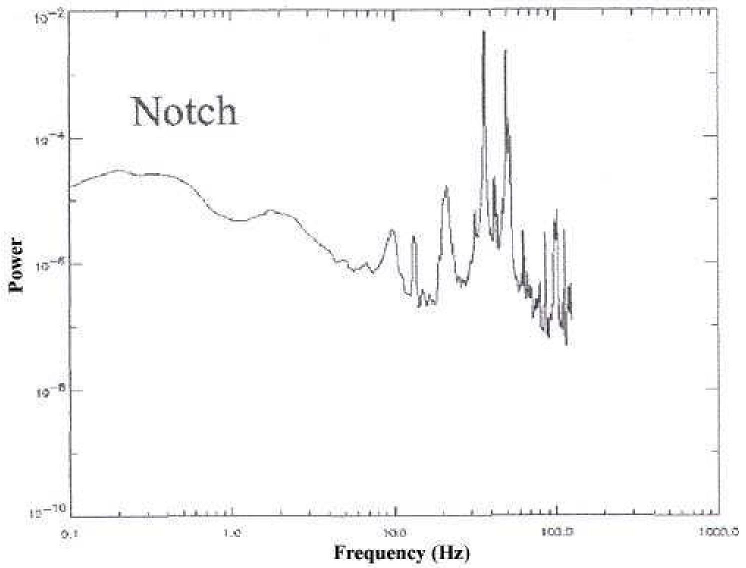

Figure 5.4: The spectral measurements at the experimental site in Şarköy using a N filter

surements show that this site is more isolated from anthropogenic noise compared to the site in Gönen.

Figures 5.5 and 5.6 illustrate the number of data points for local times of September, October, November and December 2004 for Gönen and Şarköy respectively. It is clear that the Şarköy data is better in quantity.

Based on the experience gained by these exercises, both from quality and quantity considerations, the Şarköy data are shortlisted. Therefore, SR dimension of this work is based on the original Şarköy data.

5.2 Results Based on Signal Processing

As explained in Chapter 3 The Şarköy geomagnetic field data were sampled automatically at a frequency of 100 Hz. The frequency of 100 Hz enabled us to analyze the frequency range of [0,50] Hz, which included the first four SR frequencies of interest. The geomagnetic field data sets were processed by using a series of signal processing techniques including band-pass filtering; median filtering; Fast Fourier Transform, some spectral estimation methods including the Welch's Periodogram Analysis and signal modeling techniques including Yule Walker method, in order to obtain the SR spectral parameters; power amplitudes, frequencies

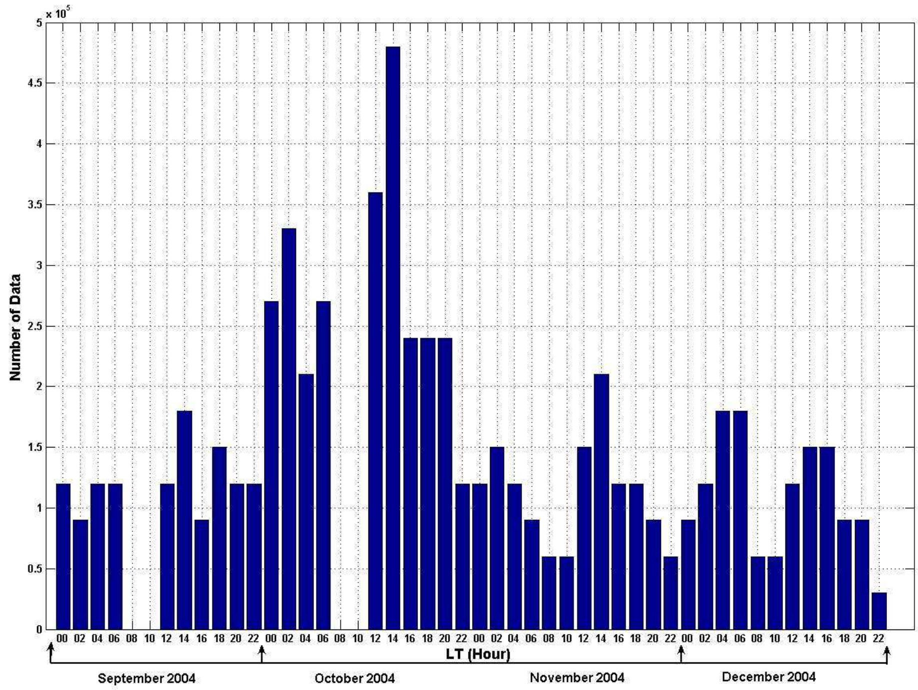

Figure 5.5: Number of data statistics for Gönen 2004 data

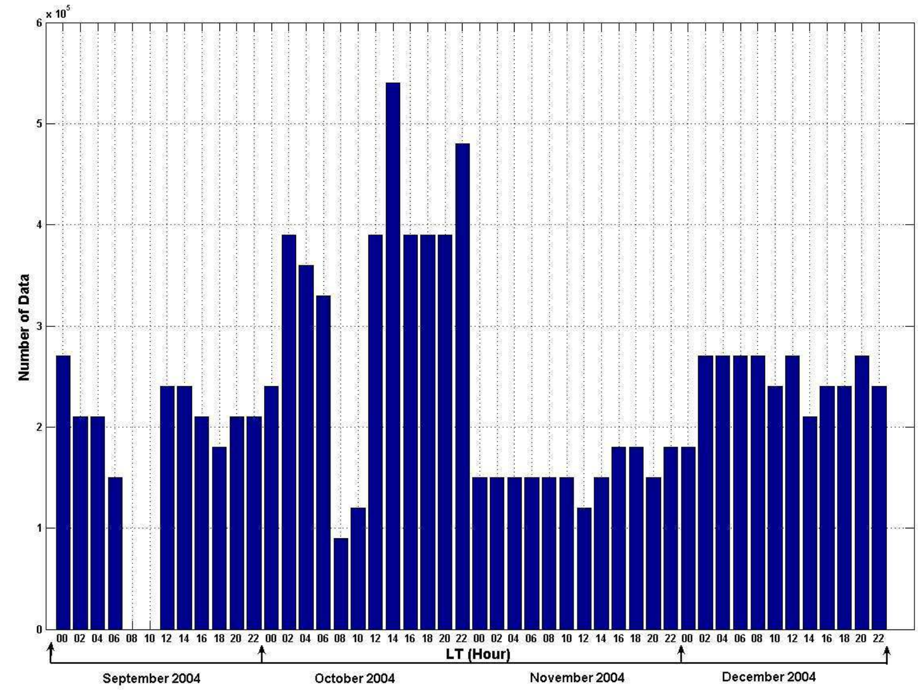

Figure 5.6: Number of data statistics for Şarköy 2004 data

and half-width.

Figure 5.7-(a) illustrate the raw Şarköy geomagnetic field data in time domain and Figure 5.7-(b) shows the first 11 sample of data presented in Figure 5.7. This Figure reveals that there is a 50 Hz periodicity in the geomagnetic field data. Since the first step in data analysis was to estimate the spectrum of the data, in the process of obtaining the SR characteristics, the elimination of the ”utility frequency” component at 50 Hz became necessary.

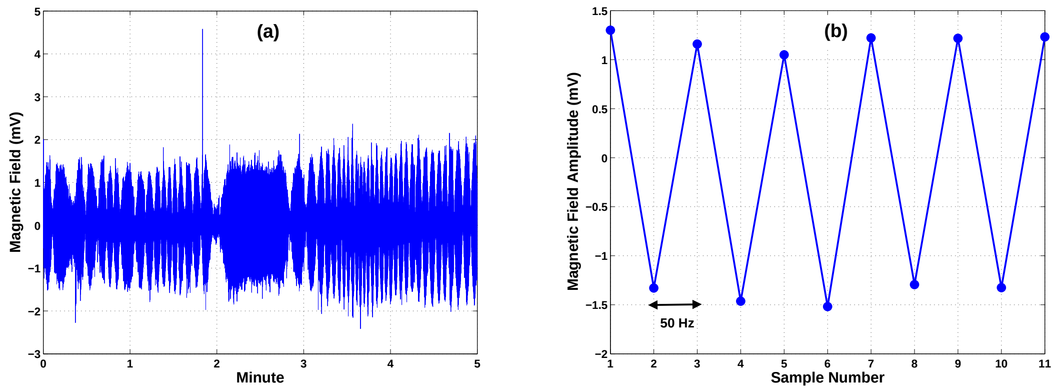

Figure 5.7: (a) Sample geo–magnetic field data in time domain for Şarköy (b) The close-up picture of geo-magnetic field data in time domain for Şarköy

In order to eliminate this frequency component from the spectrum, a bandpass filter was designed using MATLAB Software. The $3dB$ cut–off frequencies of the filter were chosen as 2 and 40 Hz, which contained the first four SR frequencies as well. The Magnitude response and phase response of the designed filter are shown in Figures 5.8-(a) and (b).

The band–pass filter constructed is a finite impulse response (FIR)[1] filter. The filter is called “finite” because its response to an impulse settles to zero eventually of 70^{th} order, with Chebyshev window (of length 71 and with a Fourier transform sidelobe magnitude is 90 dB below the mainlobe magnitude) [5].

The band-pass filtered signal is shown in Figures 5.9-(a) and 5.9-(b). Without the utility frequency at 50 Hz, the periodicity in the geomagnetic field data is removed.

The next step is to verify computationally if the band pass filtered geomagnetic data are sufficiently stationary over the 5 minute sampling interval. In other words, to computationally verify if the power spectrum of the signal exists. The power spectrum of a signal exist, *if and*

[1] a type of a digital filter

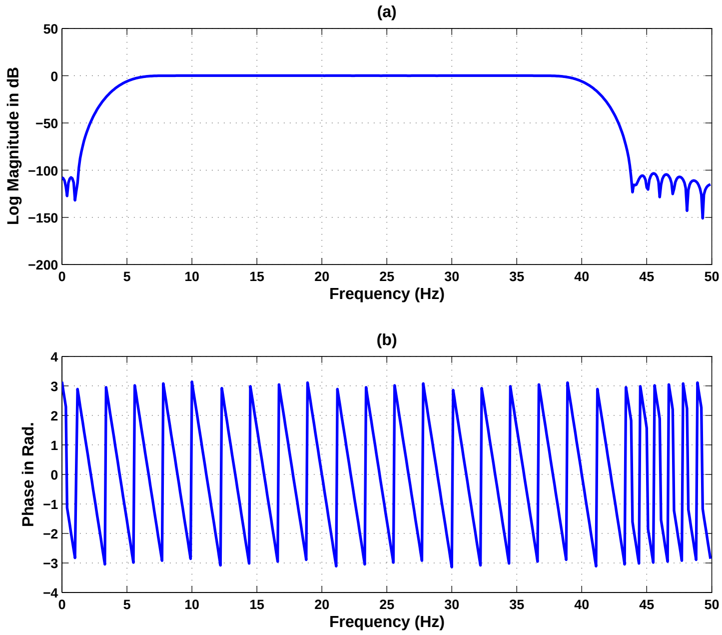

Figure 5.8: (a) Magnitude (b) and phase responses of FIR of band-pass filter

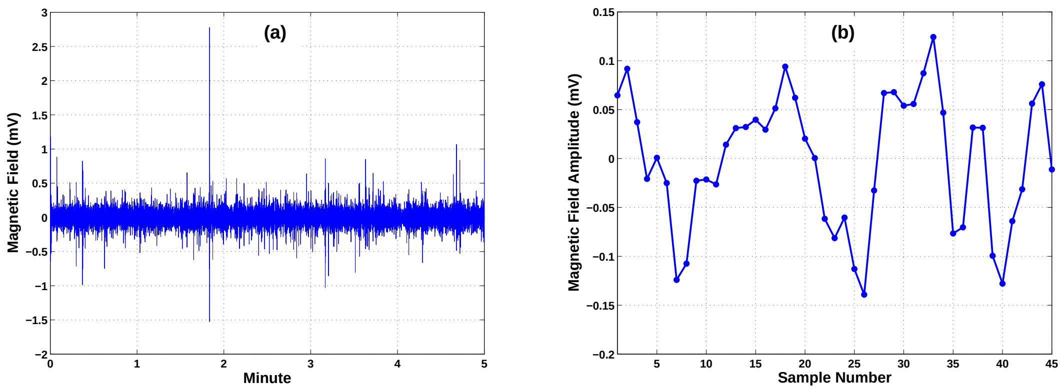

Figure 5.9: (Band-pass filtered signal in time domain (b) Close up view to first 45 samples from the band-pass filtered signal

only if the signal is stationary in wide-sense.

Quoting from [33] “A random process $x(n)$ is said to be *wide-sense stationary* if the following three conditions are satisfied” [33]:

1. The mean of the process is a constant, $m_x(n) = m_x$.
2. The autocorrelation $r_x(k, l)$ depend only on the difference, $k - l$.
3. The variance of the process is finite, $c_x(0) < \infty$

The condition (1) can be proved using a sample data set of B; say 5-min data for 1^{st} of October 2004 containing 30000 individual samples. The data set is divided into 233 subsets with a length of 256 points (by convention to 256 point DFT) each and with %50 overlap and then the mean is calculated for each subset. Figure 5.10 shows the calculated mean values for each subset. As seen in Figure 5.10 the mean values of the data sets are almost around the zero value, which satisfies condition (1).

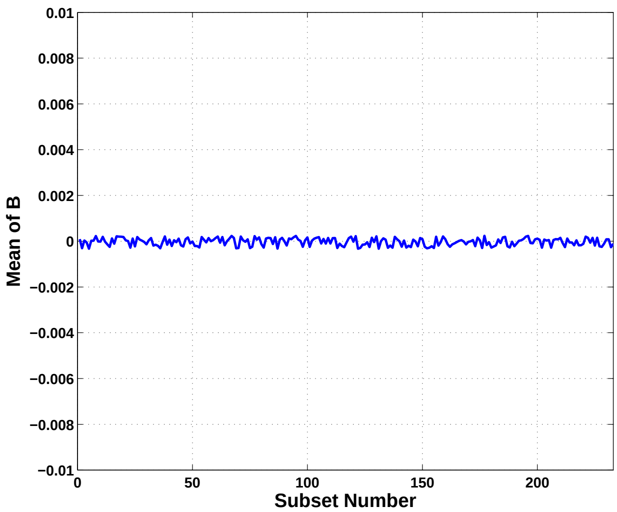

Figure 5.10: Mean values calculated for each 256 point length subset

The second property implies that the correlation function depends only on the difference between t_1 and t_2 [33]:

$$E\{x(t_1)x(t_2)\} = R_x(t_1, t_2) = R_x(t_1 + \tau, t_2 + \tau) = R_x(t_1 + t_2, 0) \; \forall \; \tau \in \mathbb{R} \tag{5.1}$$

This property may be applied to the geomagnetic field, ΔB, data by taking two subsets in the previously used sample data. To demonstrate this idea the following notations can be introduced;

- t_1 : Data subset, B_1, including from 1^{st} to 100^{th} data points,
- t_2 : Data subset, B_2, including from 201^{st} to 300^{th} data points,
- $t_1 + \tau$: Data subset including from 1^{st} to 150^{th} data points, τ being the delay of 100 data points
- $t_2 + \tau$: Data subset including from 201^{st} to 350^{th} data points

Then the correlation coefficients between B_1 and B_2 are calculated by using the MATLAB Software;

$$R_x(t_1, t_2) = 0.082$$
$$R_x(t_1 + \tau, t_2 + \tau) = 0.080$$

The correlation coefficient results obtained above show that the autocorrelation function depends only on τ for the geomagnetic field data, ΔB, thus confirming condition (2). When 256 point length random subsets are chosen from the 5–min data and correlation coefficients are calculated between 566 subsets, one can see that the correlation coefficient oscillates around 0.08, as shown in Figure 5.11.

Finally, to prove that the variance of the geomagnetic process is finite (condition (3)) one can simply calculate the variance of the sample signal by simple MATLAB function *var*(.) and find it; $c_x(0) = 0.0116$ [5].

When the variance is calculated for each subset, B, the results show that the variance stays constant around $c_x(0) = 0.0116$ for the individual subsets (Figure 5.12), which satisfies condition (3).

Since the geomagnetic field data, B, satisfies all 3 conditions listed above, it can be confidently said that the geomagnetic field data, B's, are wide sense stationary data sets and since the signal of interest is wide-sense stationary, the power spectrum for the signal exists.

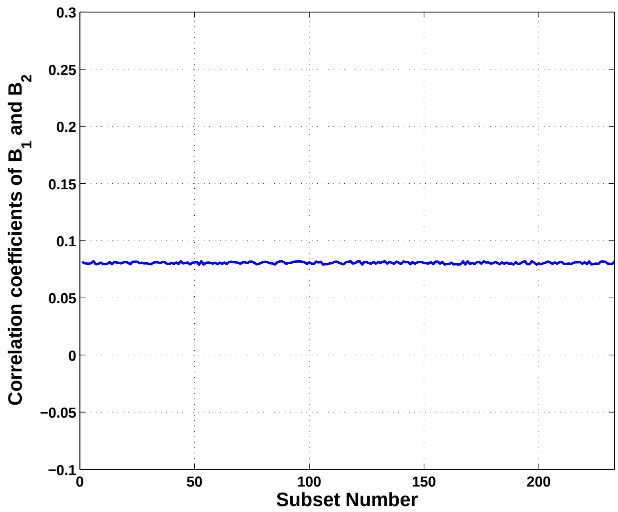

Figure 5.11: Correlation calculated between 256 point length random subsets

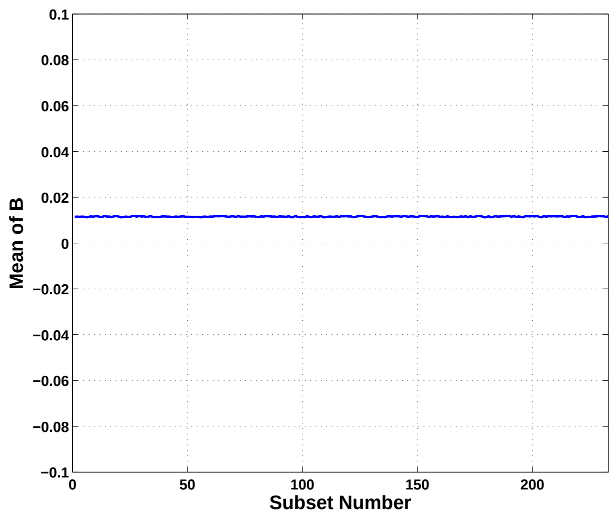

Figure 5.12: Variance calculated for each 256 point length subset

5.2.1 Calculating the Power Spectral Density

Since it is hard to find a model the signal acquired from the geomagnetic field data, in this study mostly non-parametric spectral estimation methods of Chapter 4 are used. However, an example of the parametric methods is given below;

For our purposes we will use the Yule-Walker autoregressive spectral estimation method described in Chapter 4. The order of the model is determined by number of the peak frequencies we are searching for. In the frequency interval of 5-40 Hz there exist 5 Schumann Resonance frequencies (8, 14, 21, 26, and 32). So we chose the model order as 10 (since a peak number of 5 is equal to a pole number of 10). Figure 5.13 shows the power spectrum estimation using Yule-Walker method. It is clear that the estimation of the first two frequencies are relatively better than the others. The first two estimated frequencies are 7.8 and 14.7 Hz which are close to first and second Schumann resonance frequencies (7.8 and 14 Hz).

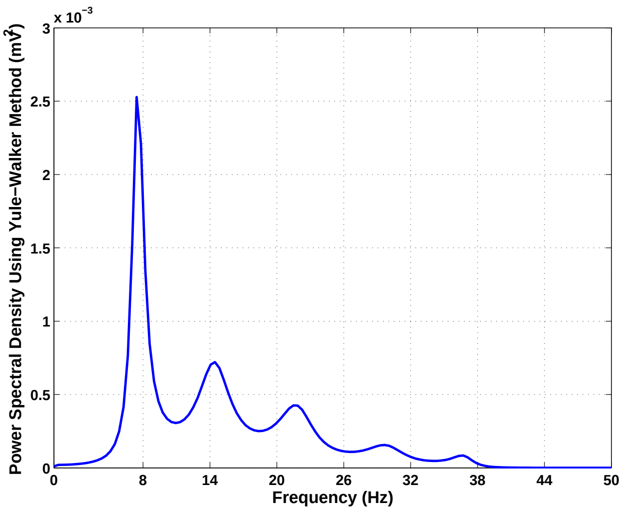

Figure 5.13: Power spectrum estimation via Yule-Walker

However, when the modes get higher the estimation becomes worse. This bad estimation arises because of two reasons;

1. The AR methods tend to adequately describe spectra of data that is "peaky", that is, data whose PSD is large at certain frequencies [33, 5]. Consequently, the Yule-Walker method takes into account the "peaky" spectra; taking into account the peaks in the spectrum even if the spectrum is noisy.

2. As described before, AR methods first model the signal using delay coefficients for time-delayed values. In other words, the method tries to find the coefficients that minimize the error between actual signal and model signal. Throughout this procedure, as the time delay increases the priority of the coefficient decreases; the model is modified in such a way that the error caused by the primary coefficients are decreased. As a result the model performs better for the primary peaks and worse for others.

The method used to acquire the geomagnetic field data is very sensitive to noise coming from the environment. So it is expected to see some burst like peaks in the spectra that the autoregressive methods will identify as poles. This phenomenon may be understood more easily when the order of the Yule-Walker model is increased. Figure 5.14 shows the estimated power spectrum for the same signal sample of Figure 5.13 with a model of order 20.

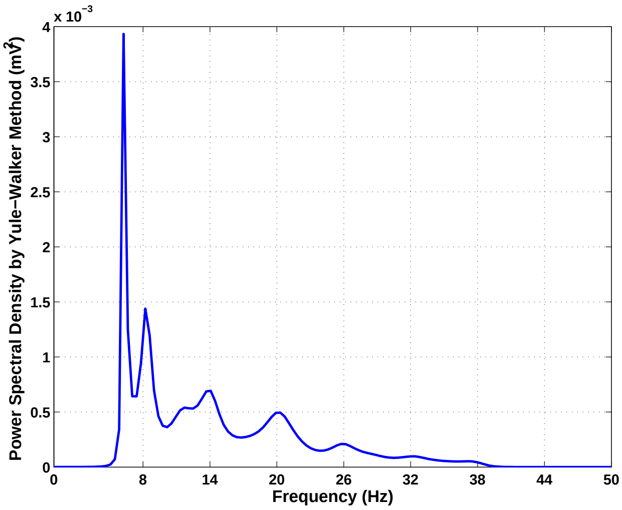

Figure 5.14: Power spectrum estimate by Yule-Walker of order 16

There are a lot of peaks in the spectrum estimated by the model. The model identifies any burst like noise in the signal as a peak in the spectrum. Because of the fact that the changes in the global lightning activity can be seen on the geomagnetic field activity power spectrum as wide peaks near the resonance frequencies, not as individual peaks at some very specific frequencies, it is trivial to identify the source of these noisy peaks as the noise from any electronic device, some technical phenomena from the experimental setup itself or even some anthropological noise. In fact, the identification of these noisy peaks is very complex and will be considered in the future works.

After giving an example to parametric methods, one can now test non-parametric methods in order to analyze the data of interest. As mentioned before in Section Chapter 4, Welch's method is nothing but averaging the estimated modified periodograms. For our purposes Welch's method seems to be the optimum way of estimating the power spectral density. Figure 5.15 shows the PSD estimate in logarithmic scale using a Hamming window function and using 8, % 50 overlapping windows and an FFT length of the same length of each window.

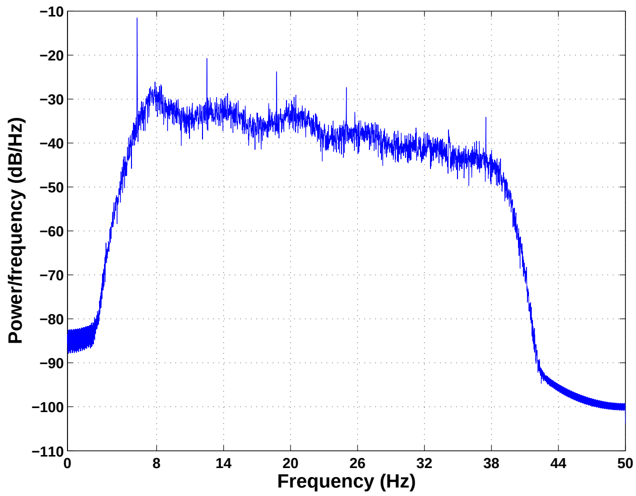

Figure 5.15: Power spectrum estimate via Welch's Method in logarithmic scale

The purpose of using logarithmic scale is to show the peaky values that occur just before the Schumann Resonance frequencies of 8, 14, 21 and 26 Hz. As mentioned in the previous section, these peak frequencies are the ones that one finds when Yule Walker method is used for PSD estimation. These peak values at individual frequencies were identified as noise that may be caused by different sources.

To get better results by getting rid of these peaky values, it is possible to use a filter that serves our purpose. The filtering technique used is the "Median Filtering" defined below;

5.2.1.1 Median Filtering [5]

Median filtering is similar to an averaging filter [2]. However, in median filtering, the value of the output is determined by the median of the neighborhood values, rather than the mean

[2] in average filter each output value is set to an average of the values in the neighborhood of the corresponding input value [5]

[5, 34]. The median is much less sensitive than the mean to extreme values called “outliers” [5, 34, 35]. Median filtering is therefore more successful in removing the outliers without disturbing the sharpness of the signal, which is exactly the kind of filter we want to employ [5, 34, 35]. The dimension of the median filter determines the neighborhood of the corresponding input value [5].

Figure 5.16 shows the PSD of the median filtered signal using a median filter of dimension 7 in the logarithmic scale. As it is seen in this Figure, the noisy peaks are reduced and the sharpness of the signal is still preserved after the filtering process.

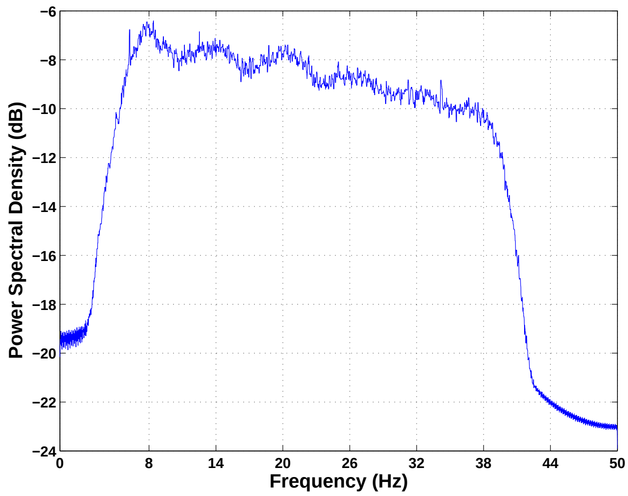

Figure 5.16: Median filtered (of dimension 7) power spectrum estimate via Welch’s Method in logarithmic scale

When the dimension of the filter is increased it is possible to get better results, however increasing the dimension more than some optimum value decreases the sharpness of the signal.

Experiencing different dimensions, by trial and error, it is found that a dimension of 11 is enough to remove the noise from the geomagnetic data. Figure 5.17 shows the PSD estimate using a median filter of order 11. As this figure illustrates, the resulting estimate is good enough to process, in which the Schumann Resonance frequencies are visible and processible.

5.2.1.2 Experiencing with Different Window and DTFT Lengths

The PSD estimate via Welch’s method will give different results for different window lengths and different lengths of FFT. In addition, the results obtained may be different for different

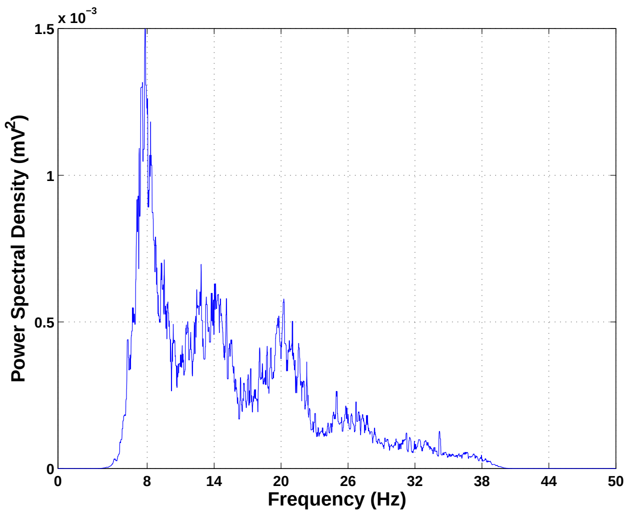

Figure 5.17: Median filtered (of dimension 11) power spectrum estimate via Welch's Method in linear scale

window functions used. Figure 5.18 shows the estimated PSD estimate using 12 windows and a median filter. Furthermore, a Hanning window function is used and FFT length is equal to the length of window. Therefore, all of the parameters of spectral estimation are changed in this example. Figure 5.18 is slightly different from the previous estimates. Since a curve-fitting technique will be employed to determine the SR mode frequencies and corresponding amplitudes, this slight difference in the PSD estimates does not contribute to the calculated values much.

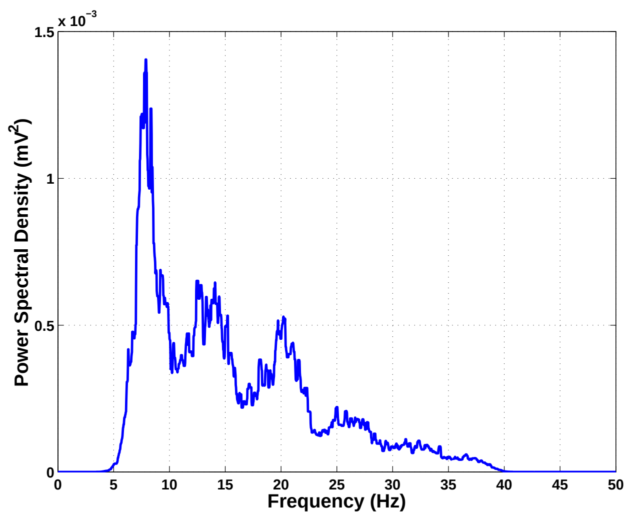

Figure 5.18: Median filtered (of dimension 11) power spectrum estimate via Welch's Method using 12 modified windows with Hanning Window Functions

5.2.2 Lorentzian Curve Fitting

Despite the fact that the SR spectral lines differ from the theoretical Lorentzian functions, it was indicated by several authors that these functions are successful in fitting SR spectral curves [53, 54, 55, 2, 56].

To calculate the SR peak frequencies and peak amplitudes, PSD estimate curves were fit using a curve consisting of 6 Lorentzian functions. The Lorentzian approximating function has the form [2, 56];

$$\sum_{i=1}^{6} L_i(f); \qquad L_i(f) = \frac{A_i}{(\frac{f-f_i}{\omega_i})^2 + 1} \tag{5.2}$$

In Equation 5.2, A_i is the amplitude of mode i as a function of frequency f, f_i is the central frequency of mode i, and ω_i is the half-width of mode i in Hz [2]. A sample spectrum with Lorentzian fit superimposed on are also shown in Figure 5.19.

The first Lorentzian function was used to fit the ELF ($f_i < 5Hz$) background noise which sometimes plays a dominant role in the horizontal magnetic component. The second to sixth Lorentzian functions were used to fit modes 1 to 5 of the SR (8, 14, 20, 26 and 32 Hz) [2].

Least square fitting method was employed during the fitting process. This process requires a model that relates the response data to the predictor data with one or more coefficients [5]. The result of the fitting process is an estimate of the "true" but unknown coefficients of the model [5]. The residual for the i^{th} data point r_i is defined as the difference between the observed response value $\hat{y}_i$ and the fitted response value, and is identified as the error associated with the data [5];

$$r_i = y_i - \hat{y}_i[5]$$

The summed square of residuals is given by;

$$S = \sum_{i=1}^{n} r_i^2 = \sum_{i=1}^{n} (y_i - \hat{y}_i)^2$$

where n is the number of data points included in the fit and S is the sum of squares error estimate [5]. Since Lorentzian Functions are non-linear functions a non-linear least squares fitting method is used.

The spectrum was obtained as the mean of two hours data (24 pieces of 5 minute data). After fitting the spectrum, SR parameters were easily calculated.

5.2.3 Diurnal Variations

As an example, Figures 5.19 and 5.20 shows the monthly smoothed diurnal variations of the powers of the first four SR modes, which are deduced from the $\overrightarrow{H}_{ew}$ component measured during October 2004. As these Figures illustrate, the diurnal variation of the SR data exhibit a maximum around 1400 UT in all of their four modes. The Turkish data thus confirm the fact that the African lightning activity is the main contributing source [24].

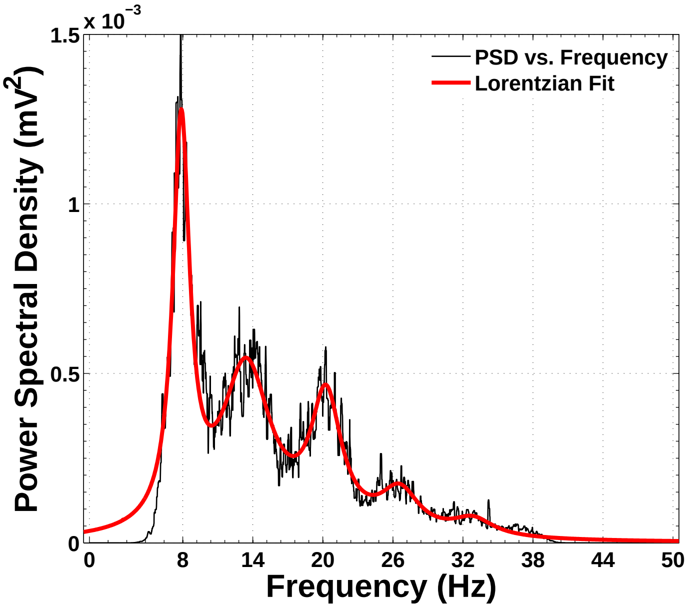

Figure 5.19: Power spectral density of SR versus frequency. Superimposed is the Lorentzian approximation (bold curve)

Figures 5.21-(a, b, c, d) show the monthly mean diurnal variations of the first four SR mode frequencies for the same data. As seen in these figures, the variations observed at the central frequencies of the four SR modes exhibit a complex behavior in comparison with the power variations and hence it is more difficult to explain them. However, this figure is useful to demonstrate the frequency variations of SR in time, in order to be more familiar with the nature of data. Such variations might be an indication of the important characteristics of

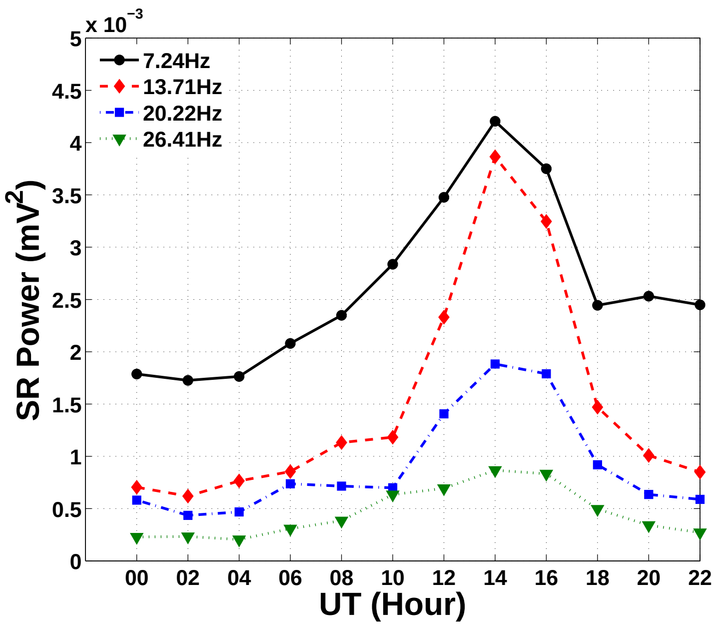

Figure 5.20: Monthly mean diurnal variations of the first four SR Mode powers obtained from the H_{ew} data during October 2004 [12]

the process. The variations of the SR mode frequencies are between 6.9–8.0 Hz for the first mode, between 13.6–14 Hz for the second mode, between 19.6–20.4 Hz for the third mode and between 25– 26.5 Hz for the fourth mode. The coefficients of variation (the ratio of standard deviation to the mean) for the mode frequencies, which allow comparison of the variation of different mode frequencies that have different mean values, are, for the first mode 5.1%, for the second mode 1.3%, for the third mode 1.1% and for the fourth mode 2%.

5.3 Results Based on Data Driven Modeling

5.3.1 Forecasting the Schumann Resonance Intensities

As explained in Chapter 4, the revised METUNN model employed in this work is a feed-forward NN with one hidden layer, using a Levenberg Marquadt Backpropagation algorithm with validation stop during the training process [45, 12] and using a new weight initialization method [47].

The objective of this phase of the investigation is to forecast the first SR mode powers (fS-Rmp) of Şarköy different time steps in advance. However, the first step is to forecast the SR amplitudes two hours in advance and see if the model is successful in doing so. In order to

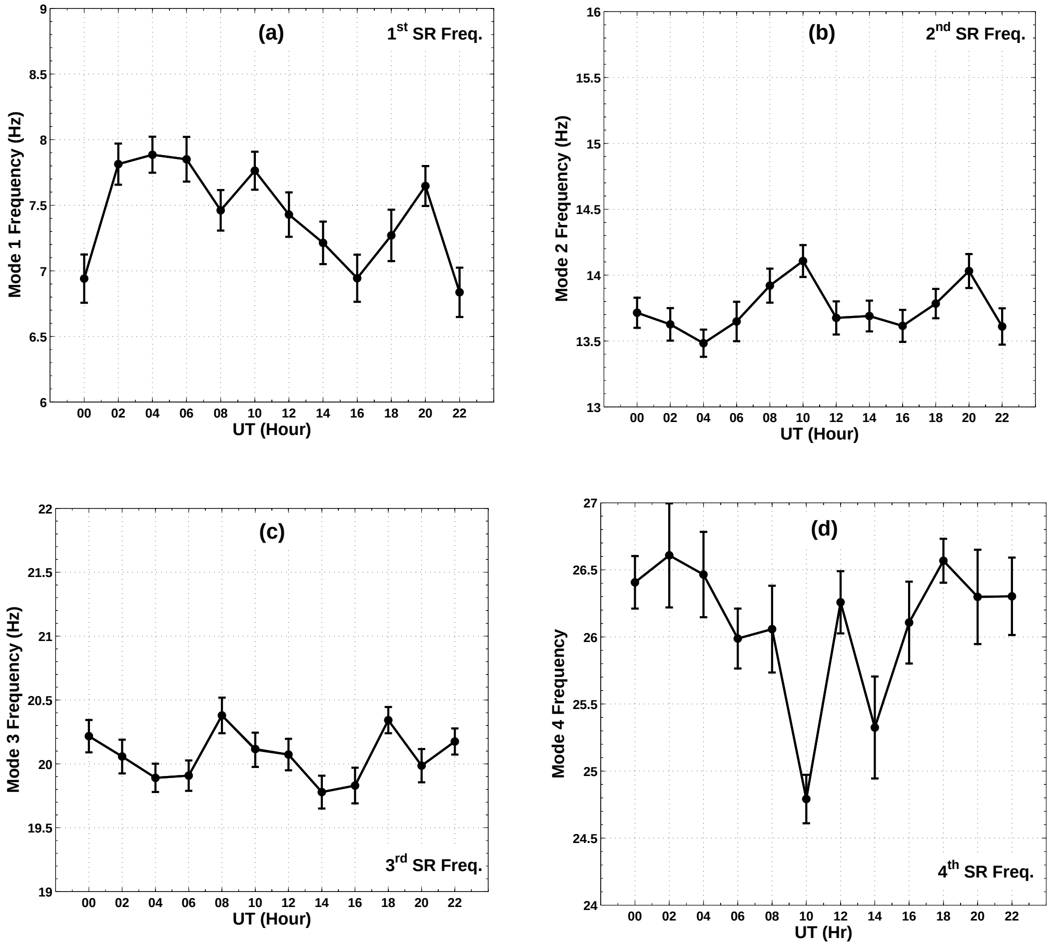

Figure 5.21: Monthly mean dirunal variations of first four SR mode frequencies with error bars indicated on the average values.

achieve this task, the SR data covering the period of 2004, September and October were chosen as the “training data”. The data for the “operation” phase consisted of two data sets, April 2005 and November–December 2004. There were several models constructed. Each one of these models differed from each other in terms of the number of input parameters and number of hidden layer neurons. The output for each of them was the forecast of the first SR mode power two hours in advance.

In this particular application of the revised METUNN, the inputs to the model are the spectral parameters (A_i, f_i) of the SR and some meteorological parameters. In this work, the African Tropical Region precipitable water (PW) values for the entire atmospheric column, specific humidity (SH) and relative humidity (RH) data of 300 *hPa* pressure level are employed as additional inputs into the revised model. Any relative humidity value obtained at different pressure values can be meaningful, since enhanced tropical convection systems are associated with enhanced upper-tropospheric humidity [26] and therefore, based on the know-how and experience of the Group, a “significance of test” [57] has been used in determining the significant inputs based on the smaller output error criteria. In this search, it turned out that the 300 *hPa* RH and SH produce smaller errors in forecasting the SR intensities 2h in advance. The most significant inputs and the number of hidden neurons that will optimize the output of the neural network are determined by using the procedure developed earlier by [57].

Table 5.1 exhibits the results for four selected NN models, the significant input parameters and the output for each of four models. The time of the day is expressed in terms of some trigonometric functions [58]. Diurnal variations of the variables are to be reflected carefully. Trigonometric relations are used to achieve the continuity of the data in time. For example, in these trigonometric relations the adjacency of the last hour of the previous day and the first hour of the present day is taken care of. This procedure simplifies the perception of the inherent characteristics of temporal variations by the NN model and it signifies how important the part of a day as temporal input [12]. Since the meteorological data had been recorded every six hours [59], these data were interpolated to have a compatible set in terms of time resolution with those of the SR measurements. The performance of the Models are quantified in terms of several computed error values and the cross correlation coefficients between the observed and forecast SR values, as illustrated in Table 5.1. Summarizing the results of Table 5.1, both precipitable water and specific humidity seem to be more significant inputs to the model. Therefore, the optimum model is proposed to be that of M4.

Table 5.1: The inputs and performance table for four different METUNN Models ("✓": if the models included those parameters as input; "-": if the models did not include those parameters as inputs)

Model No. / I/put	M1	M2	M3	M4
Time of the day	✓	✓	✓	✓
Amp. of 1^{st} **SR(k):** $A(k)$	✓	✓	✓	✓
Freq. of 1^{st} **SR(k):** $F(k)$	✓	✓	✓	✓
1^{st} **diff.:** $\delta_1(k) = A(k) - A(k-2)$	✓	✓	✓	✓
2^{nd} **diff.:** $\delta_2(k) = \delta_1(k) - \delta_1(k-2)$	✓	✓	✓	✓
Precip. water (kg/m^2)	✓	-	-	✓
Spec. humidity (g/kg)	-	✓	-	✓
Rel. humidity (%)	-	-	✓	-
Nu. of hidden Neurons	8	8	8	8
O/put	SR(k+2)			
Error values and cross correlation coefficients between the observed and forecast SR				
Abs. Err. $(mV^2) \cdot (10^{-4})$	3.5	3	7	3.1
Norm. Err. (%)	17	14	39	13
Cross Corr. Coeff. (%)	85	85	63	88

5.3.1.1 Experiencing with Different Time Horizons

The performance of the system was tested for forecast horizons, Δt, of 0.5, 1, 2, 4, 6, 8, 10, 12, 18, 24, 30 and 36 hours. A semi-synthetic data set, for $0.5h$ and $1h$ cases, was created by linear interpolation. A DFT analysis performed on the SR power data of Figure 5.19 showed that 94% of the power belongs to the harmonics with period greater than $8h$ (Figure 5.22). The interpolation is then considered to be reliable since $1h$ is remarkably smaller than $8h$.

The most profitable number of fSRmp before the time of forecast varies with the time range of forecast. In general, this figure increases with increasing time range. Past fSRmp values were not directly input to the NN. Their differences of multiple orders were used. Let t_0 be the time of forecast. Then, n^{th} order difference at time t_0 is $\delta_n(t_0) = \delta_{n-1}(t_0) - \delta_{n-1}(t_0 - \Delta),\ n = 0, 1, \ldots;$ where $\delta_0(t_0)$ is the fSRmp time at t_0 and $\Delta = \Delta t$ for $0.5h$ and $1h$ cases and $\Delta = 2$ otherwise. The success of a forecast is quantified in terms of absolute and normalized error values and the cross correlation coefficients between the observed and forecast SR values. These figures are given for forecasts of time ranges (Δt) from 0.5h to 36h in Table 5.2. It is seen that all three figures are quite close to each other for forecast ranges of $0.5h$, $1h$ and $2h$. The cross

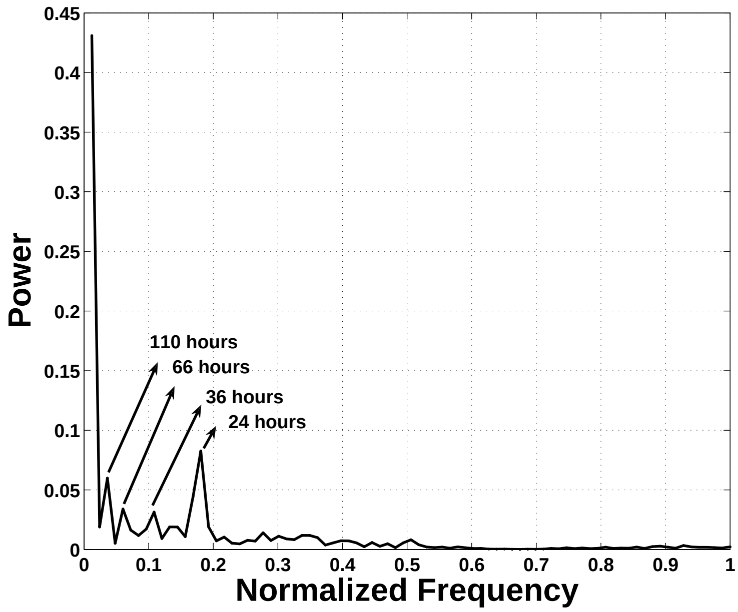

Figure 5.22: Fast Fourier Transfotm analysis of the April 2005 data

correlation values of 2*h* and 4*h* ranges are also close while their absolute and normalized errors get somewhat apart. The figures of 6*h* range are close to that of 4*h* range.

Cross correlation values for forecast ranges greater than 6h are significantly less than 0.8 so beyond this range forecast is not reliable (The confidence levels for all the cross correlation coefficients of Table 5.1 are 95%). However, it is also seen that the error and correlation coefficient values do not change significantly beyond 6*h*. Figures 5.23 and 5.25 show the diurnal variations of the power values of the Şarköy SR measurements over the period of the testing data. Superimposed are the corresponding forecast values for forecast ranges of 2*h* and 6*h* in Figures 5.23 and 5.25, respectively. As seen in Figure 5.23, the observed and forecast values seem to be in good agreement for 2*h* range. For 6*h* range, the observed and the forecast curves are synchronous in their alternations. It is also seen that the 6*h* curve follows gross variation of peaks (dips) to some extent but the model is not so successful in catching the extreme values. Alternation synchrony survives beyond the 6*h* range as well. However, for longer forecast ranges, the peak traces of forecast curves tend to follow a relatively invariant path independent of their actual values.

As seen in Figures 5.27 to 5.44, SR data have quite regular diurnal variations and it is successfully captured by the model via the time input. Accordingly, the forecast curves exhibit

Table 5.2: The performance table for different time horizons (H.O.D.U.: Highest Order of Difference Used)

Δt	**05h**	**1h**	**2h**	**4h**	**6h**	**8h**	**10h**	**12h**	**18h**	**24h**	**30h**	**36h**
H.O.D.U.	2	2	2	2	4	4	5	4	6	6	6	10
Abs. Err. ($\cdot 10^{-3}$ **a.u.**)	0.30	0.32	0.31	0.46	0.51	0.63	0.63	0.62	0.68	0.64	0.64	0.68
Norm. Err. (%)	12	13	13	19	22	25	24	26	26	26	27	27
Corr. Coeff. (R)	0.94	0.91	0.88	0.86	0.78	0.72	0.71	0.74	0.69	0.73	0.74	0.68

Abbreviations: H.O.D.U.: Highest Order of Difference Used, N.E.: Normalized Error, A.E.: Absolute Error, C.C.C.: Cross Correlation Coefficient

an in phase variation with the actual curves. On the other hand, accuracy of the forecast of an extreme value in a diurnal cycle is considered to depend on two factors. The relationship between the meteorological figures (SH and PW) at the end of forecast range and at the time of forecast gets weaker as the forecast range increases. Similarly, the SR value and its differences at the time of forecast become less reliable indicators of the peak values as the forecast range increases. Briefly, the system learns the diurnal variation pattern successfully almost independent of the forecast range, however it fails in following the extreme values as the forecast range increases. Consequently, forecast curves are inclined to have an invariant peak trace as the forecast range increases while keeping their agreement with the diurnal variation. Over $0.5h$, $1h$ and $2h$ forecast ranges, normalized errors do not vary so significantly while cross correlation values experience a moderate decrease. These forecast ranges can be considered as short enough relative to the diurnal cycle so that the SR value and its differences at the time of forecast provide strong indication about the SR value at the end of forecast range.

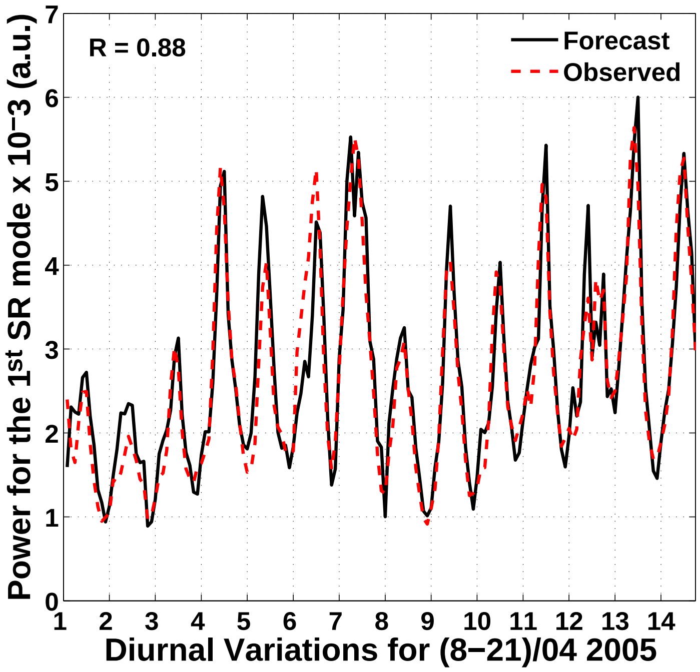

Figure 5.23: Observed (dashed) and 2h in advance forecast (solid) SR values in April 2005

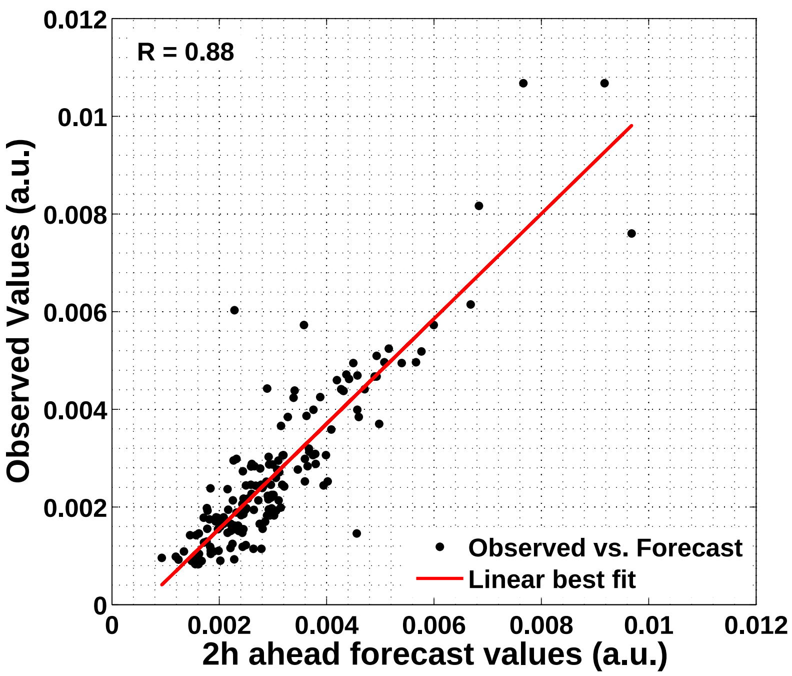

Figure 5.24: The scatter diagram of observed SR powers and the 2 hour ahead forecast values in the same period

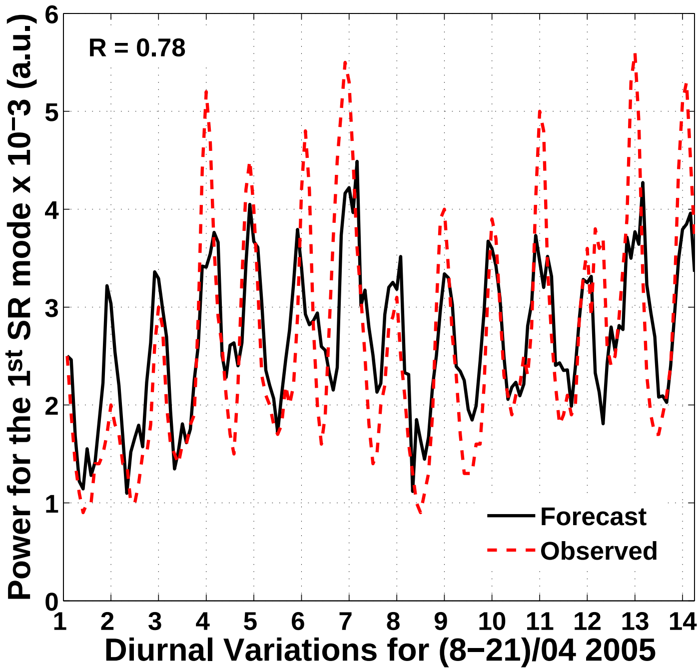

Figure 5.25: Observed (dashed) and 6h in advance forecast (solid) SR values in April 2005

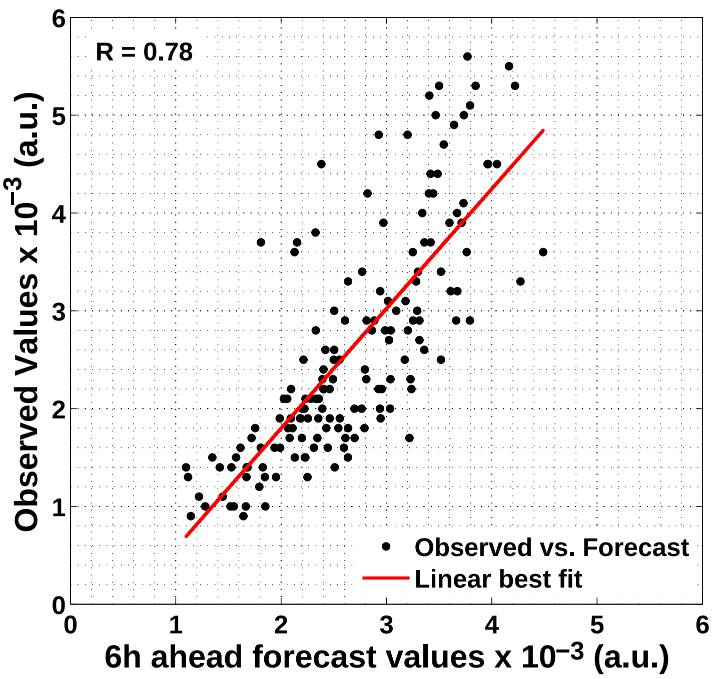

Figure 5.26: The scatter diagram of observed SR powers and the 6 hour ahead forecast values in the same period

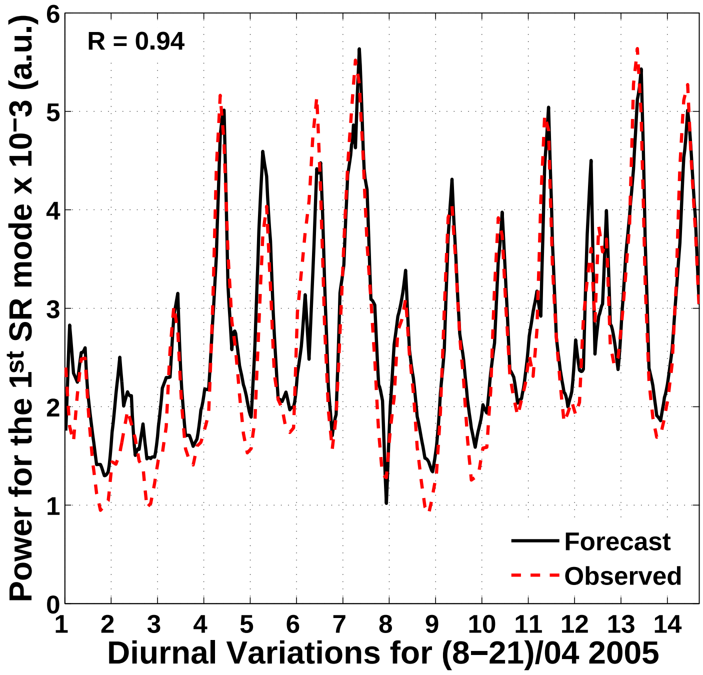

Figure 5.27: Observed (dashed) and 0.5h in advance forecast (solid) SR values in April 2005

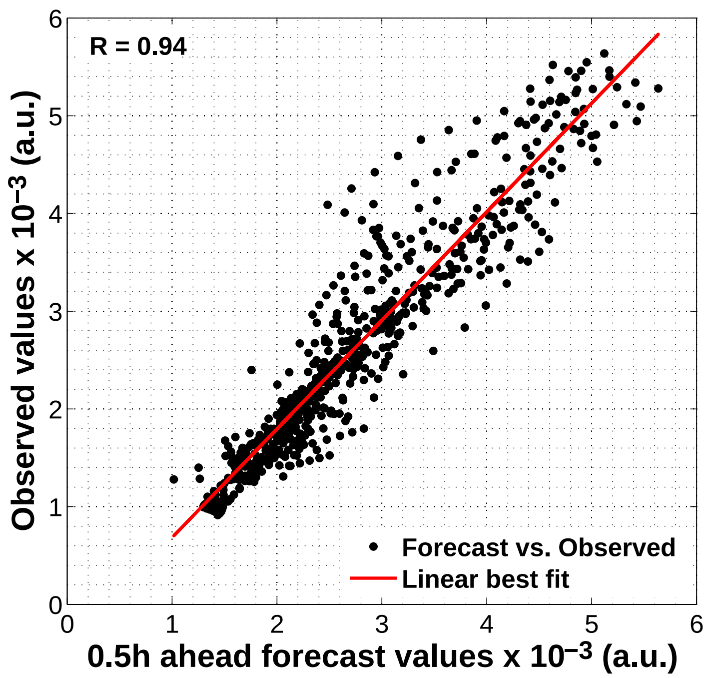

Figure 5.28: The scatter diagram of observed SR powers and the 0.5 hour ahead forecast values in the same period

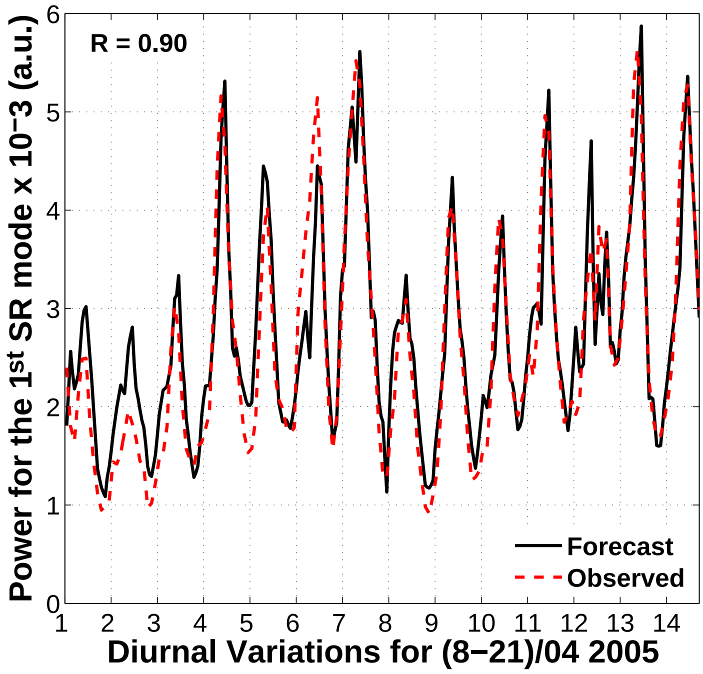

Figure 5.29: Observed (dashed) and 1h in advance forecast (solid) SR values in April 2005

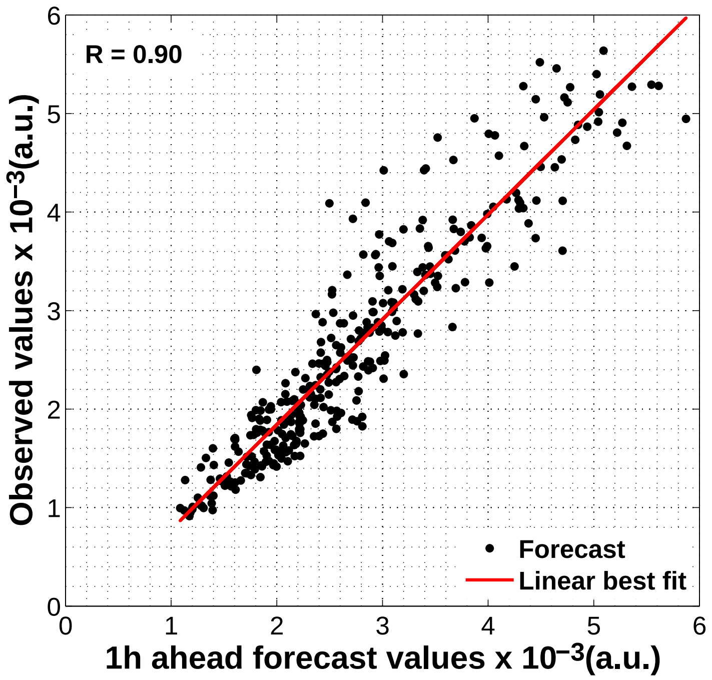

Figure 5.30: The scatter diagram of observed SR powers and the 1 hour ahead forecast values in the same period

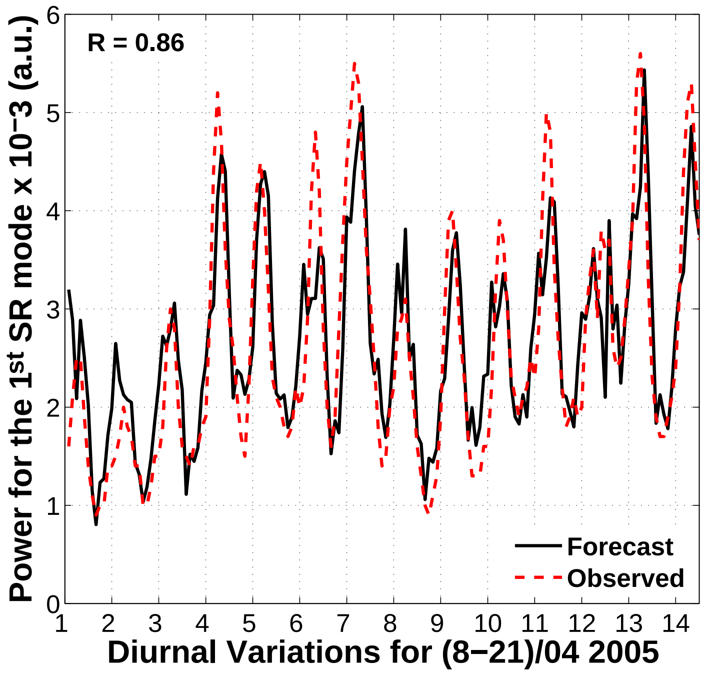

Figure 5.31: Observed (dashed) and 4h in advance forecast (solid) SR values in April 2005

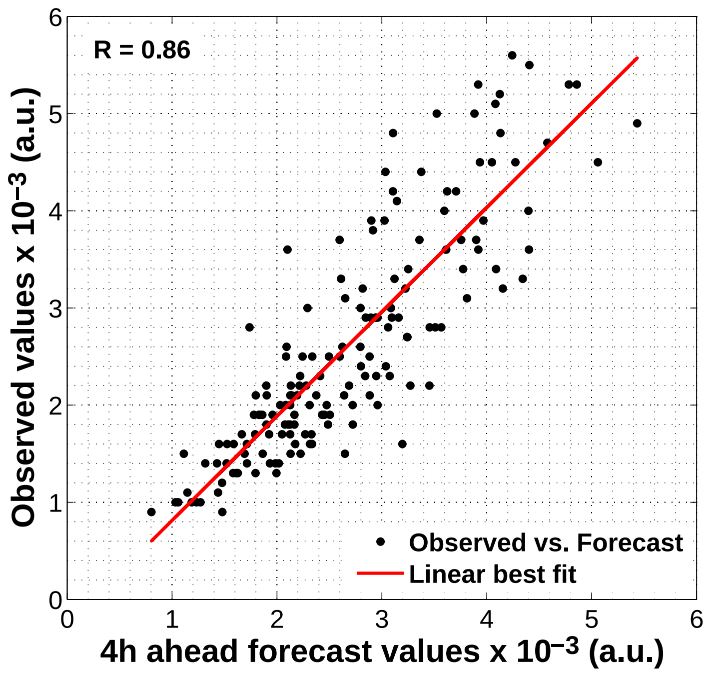

Figure 5.32: The scatter diagram of observed SR powers and the 4 hour ahead forecast values in the same period

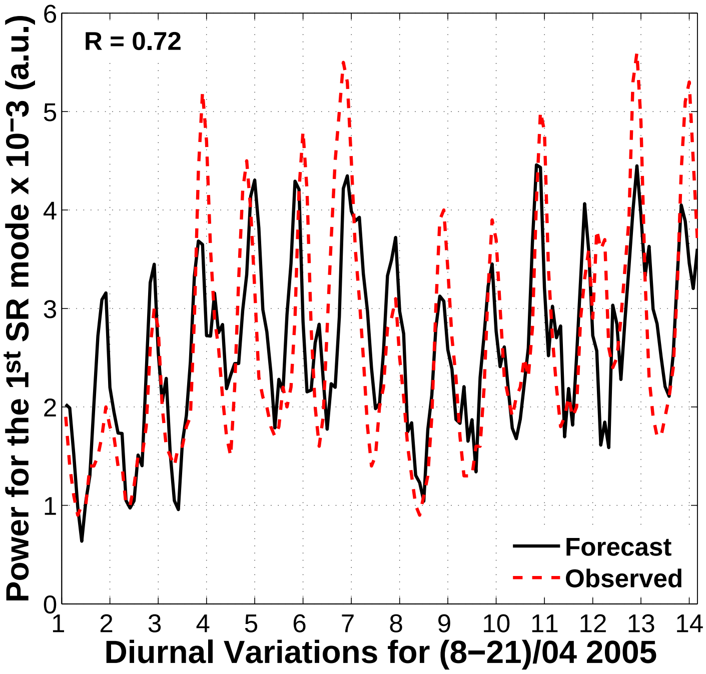

Figure 5.33: Observed (dashed) and 8h in advance forecast (solid) SR values in April 2005

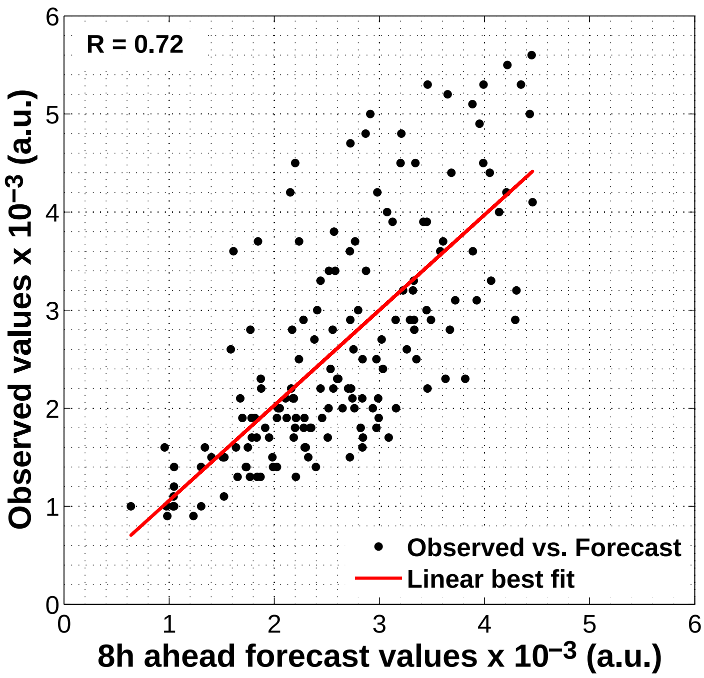

Figure 5.34: The scatter diagram of observed SR powers and the 8 hour ahead forecast values in the same period

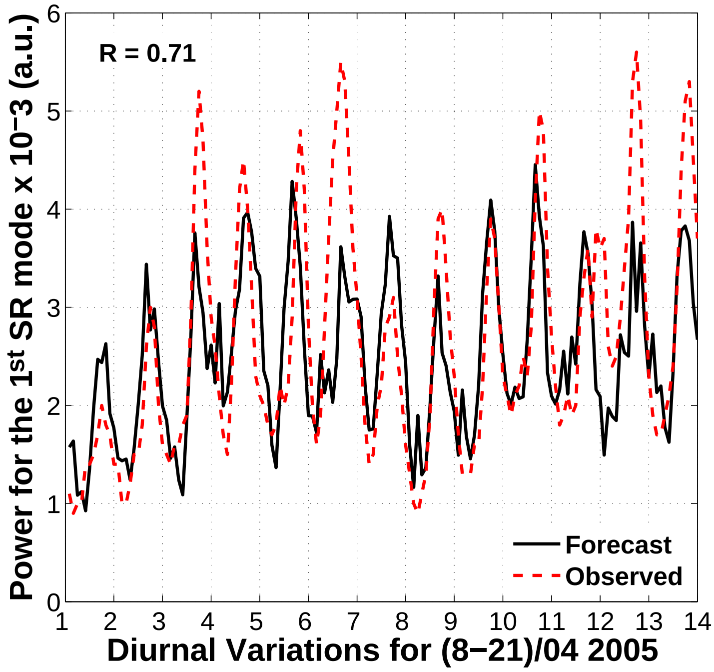

Figure 5.35: Observed (dashed) and 10h in advance forecast (solid) SR values in April 2005

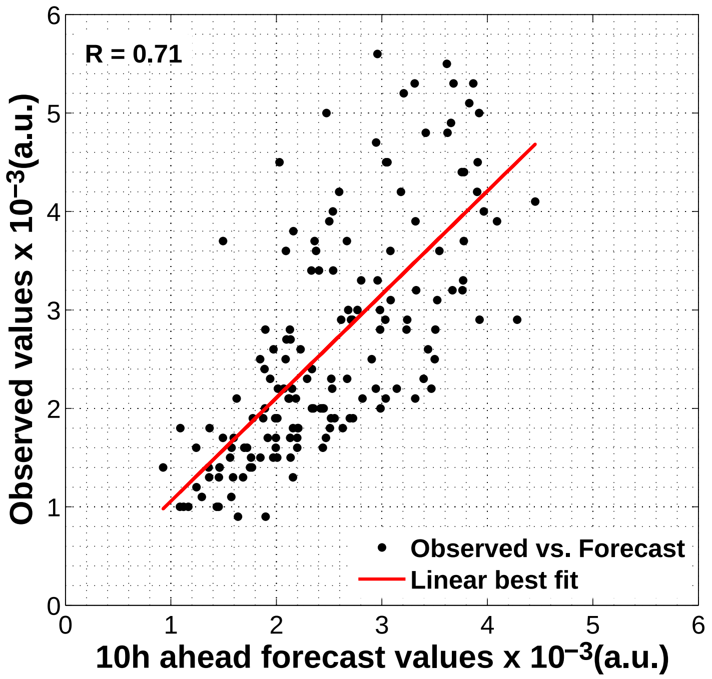

Figure 5.36: The scatter diagram of observed SR powers and the 10 hour ahead forecast values in the same period

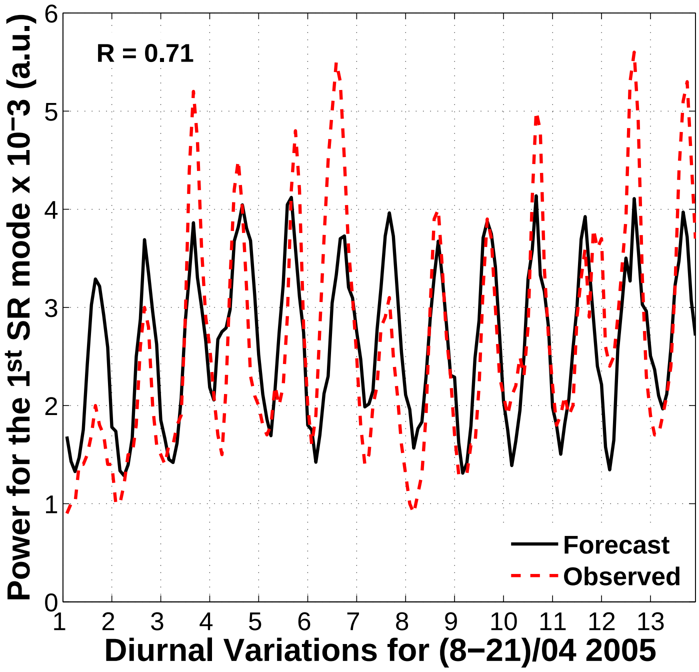

Figure 5.37: Observed (dashed) and 12h in advance forecast (solid) SR values in April 2005

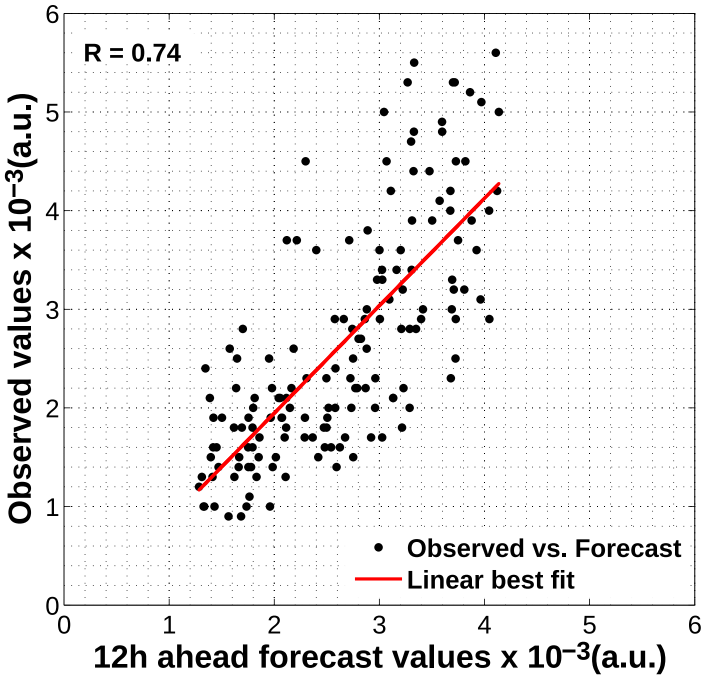

Figure 5.38: The scatter diagram of observed SR powers and the 12 hour ahead forecast values in the same period

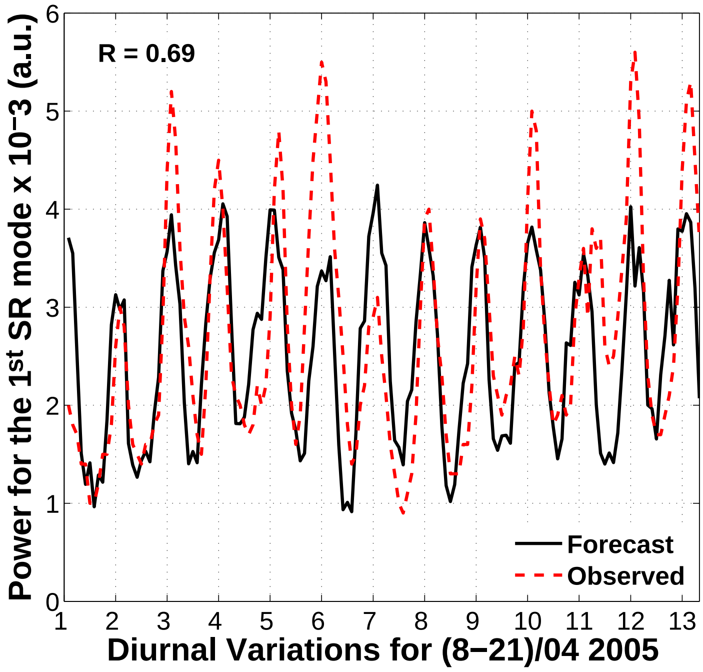

Figure 5.39: Observed (dashed) and 18h in advance forecast (solid) SR values in April 2005

5.3.1.2 Experiencing with a Different Operational Period

To check if the operational period for the NN will make any difference in the forecast procedure, the whole procedure was repeated for a different operational period. Taking into account the quality and quantity of data, the 2^{nd} operational period was chosen to be from 26^{th} of November to 9^{th} of December 2004. Table 5.3.1.2 shows the performance results obtained from the forecast of first SR intensities in the period of November–December 2004. Figures 5.45 to 5.53 show the results of the procedure described in Sections 5.3.1 and 5.3.1.1. As seen in Table 5.3.1.2 and in Figures 5.45 to 5.53 revised METUNN is able to forecast the SR intensities in an independent period of operation.

To the best of author's knowledge, this work has been the first attempt to forecast the SR power amplitudes in advance by a data driven model, such as the proposed NN Model.

It can be concluded that the proposed NN model is able to forecast the power values related to the first SR Modes different time steps in advance within the reasonable error limits as exhibited in Tables 5.1, 5.2 and 5.3.1.2.

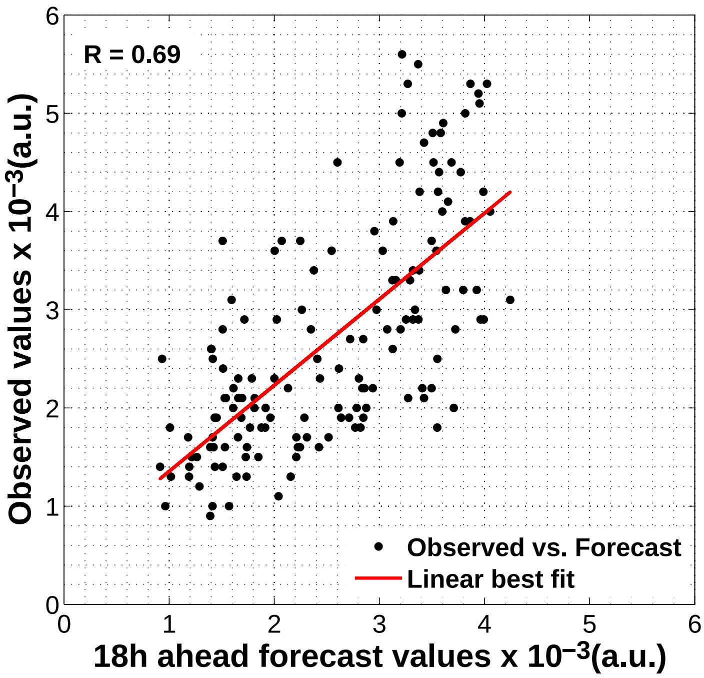

Figure 5.40: The scatter diagram of observed SR powers and the 18 hour ahead forecast values in the same period

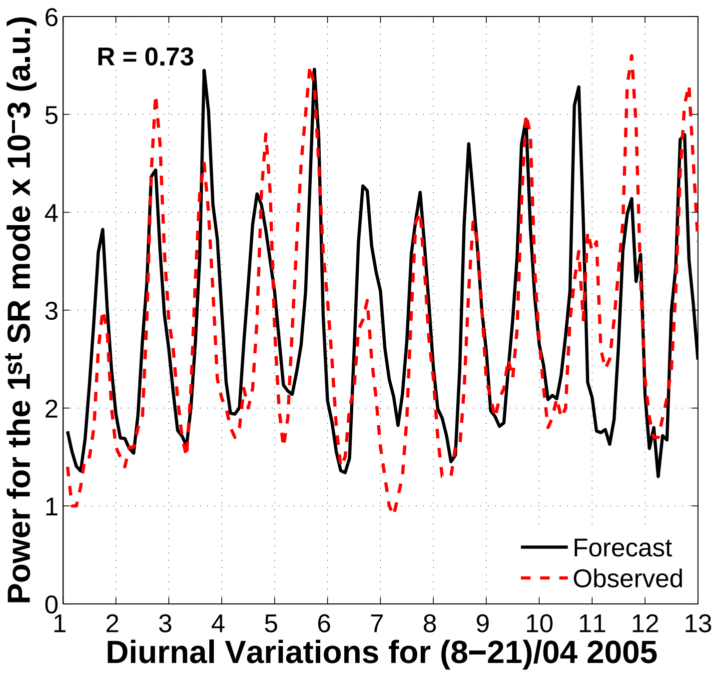

Figure 5.41: Observed (dashed) and 24h in advance forecast (solid) SR values in April 2005

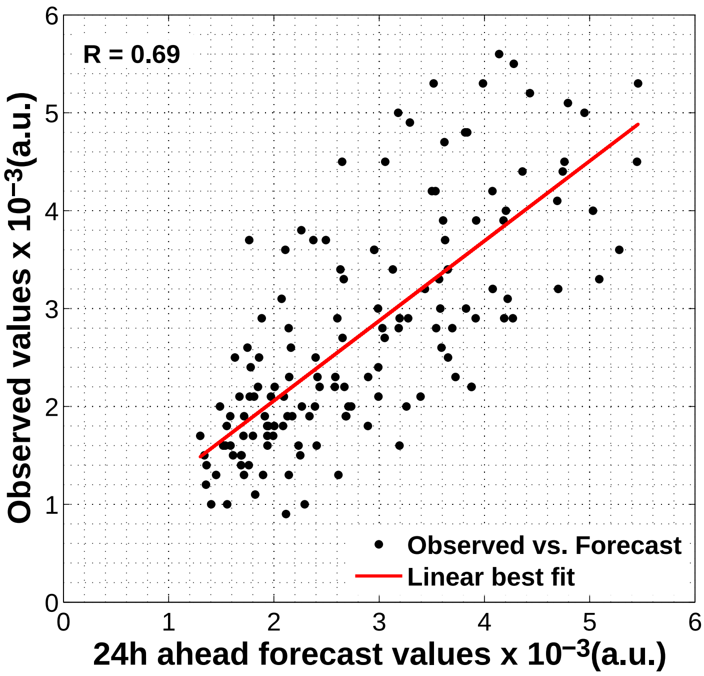

Figure 5.42: The scatter diagram of observed SR powers and the 24 hour ahead forecast values in the same period

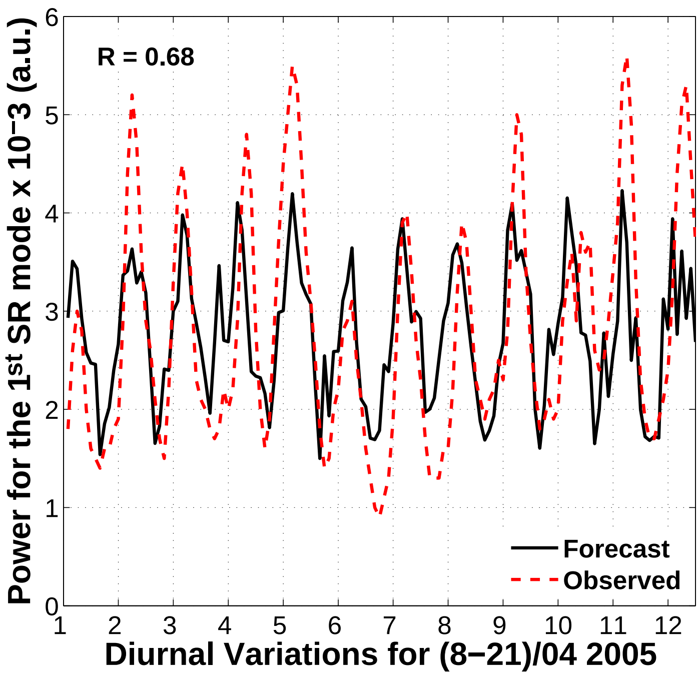

Figure 5.43: Observed (dashed) and 36h in advance forecast (solid) SR values in April 2005

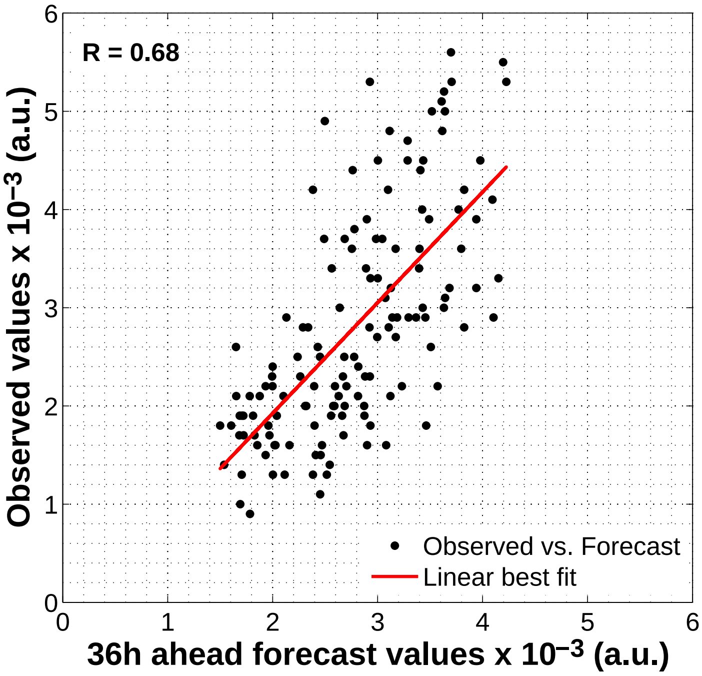

Figure 5.44: The scatter diagram of observed SR powers and the 36 hour ahead forecast values in the same period

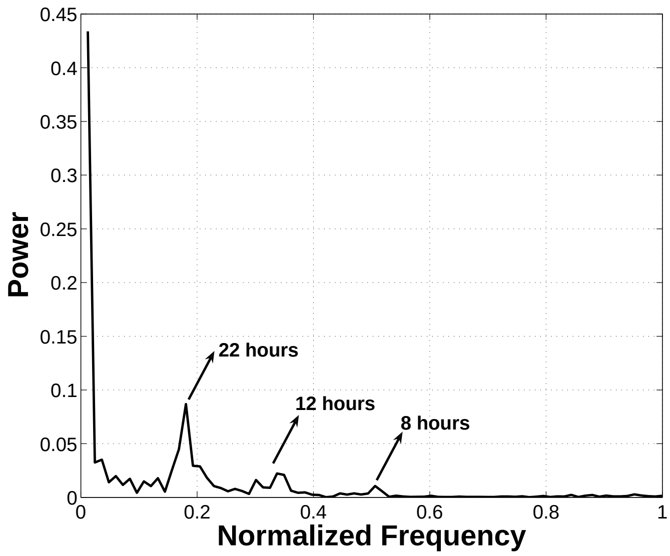

Figure 5.45: Fast Fourier Transfotm analysis of the November-December 2004 data

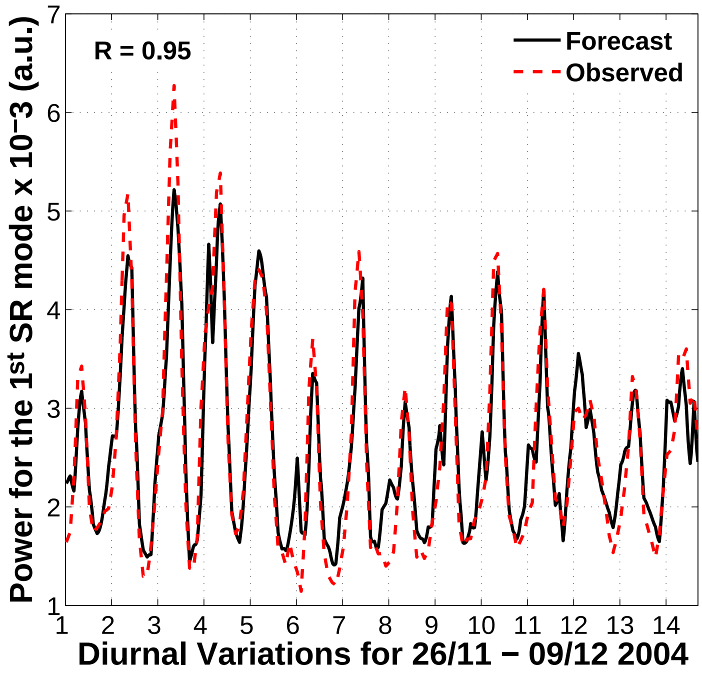

Figure 5.46: Observed (dashed) and 0.5h in advance forecast (solid) SR values in November, December 2004

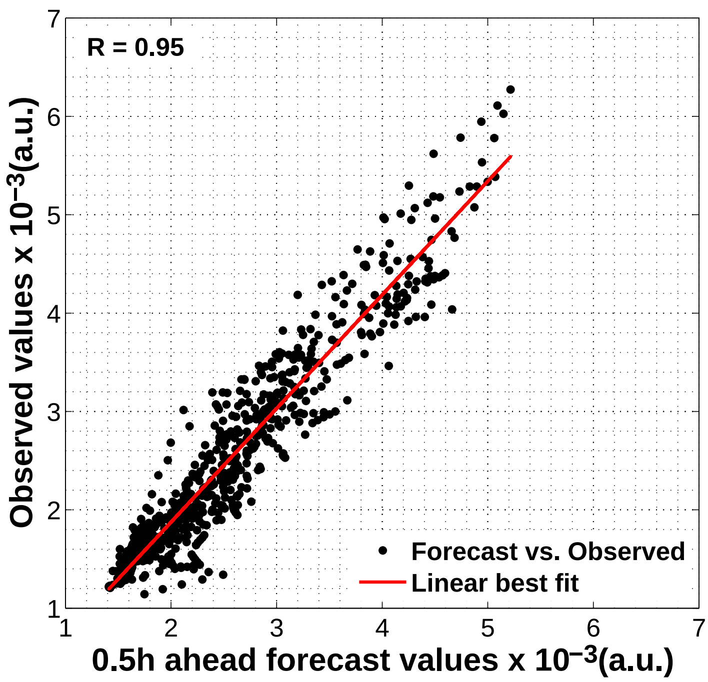

Figure 5.47: the scatter diagram of observed SR powers and the 0.5 hour ahead forecast values in the same period

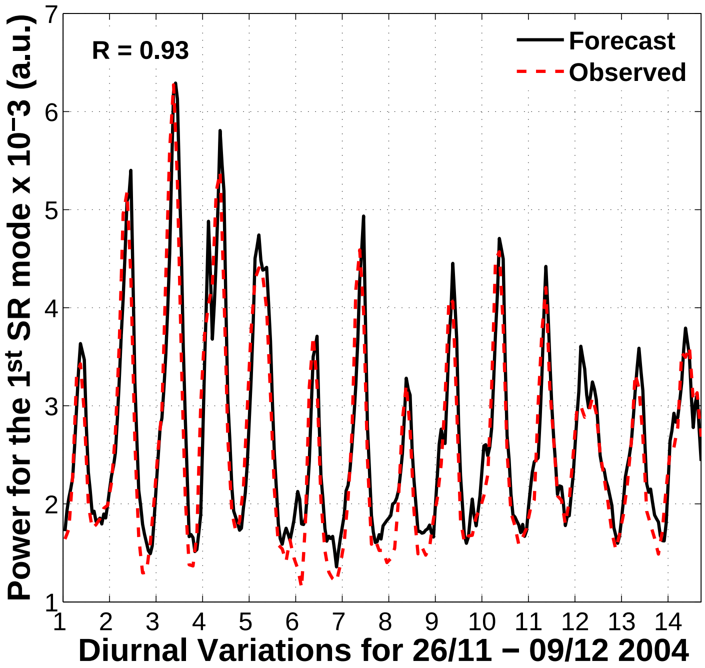

Figure 5.48: Observed (dashed) and 1h in advance forecast (solid) SR values in November, December 2004

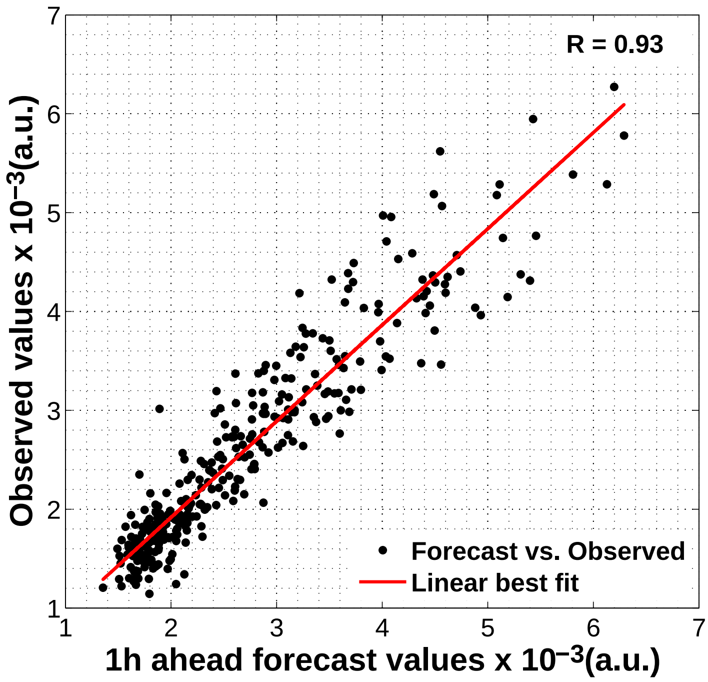

Figure 5.49: the scatter diagram of observed SR powers and the 1 hour ahead forecast values in the same period

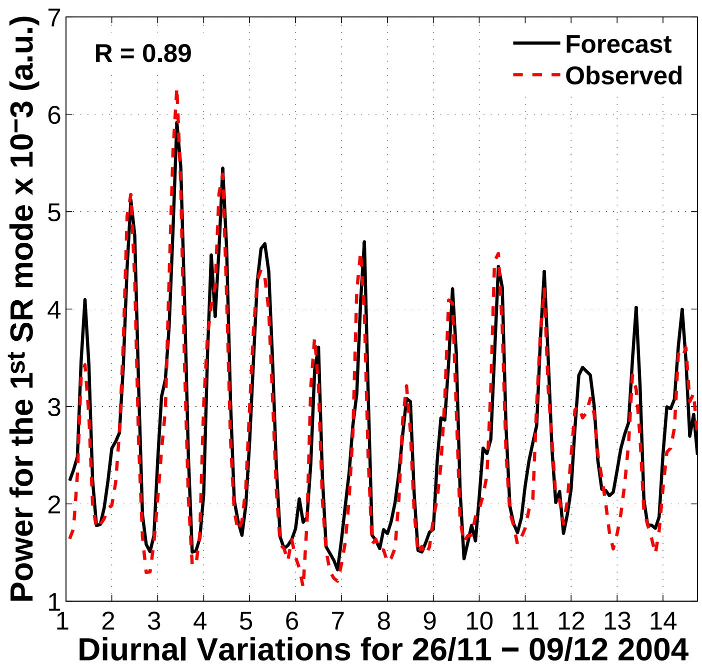

Figure 5.50: Observed (dashed) and 2h in advance forecast (solid) SR values in November, December 2004

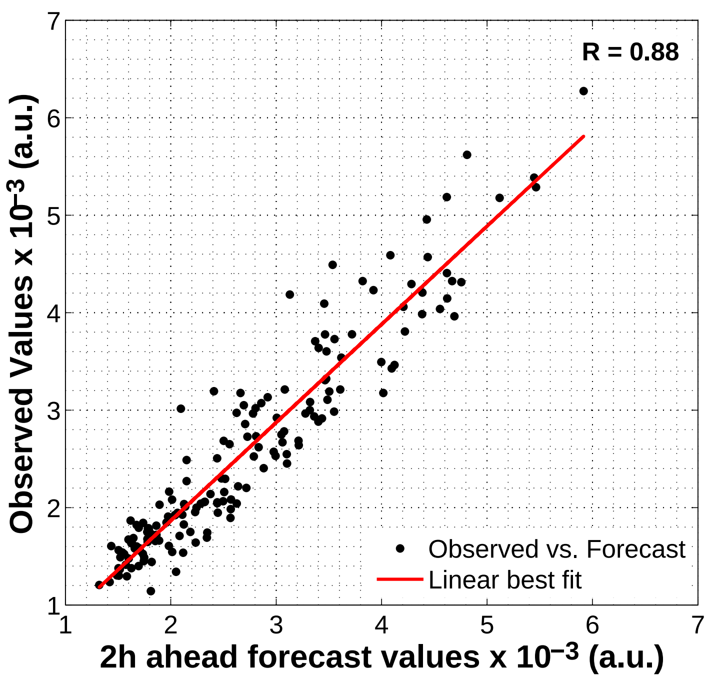

Figure 5.51: the scatter diagram of observed SR powers and the 2 hour ahead forecast values in the same period

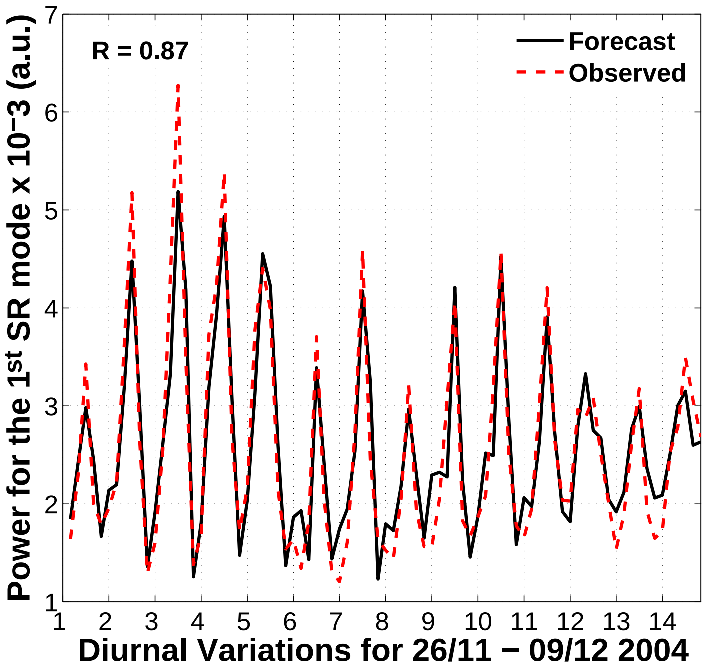

Figure 5.52: Observed (dashed) and 4h in advance forecast (solid) SR values in November, December 2004

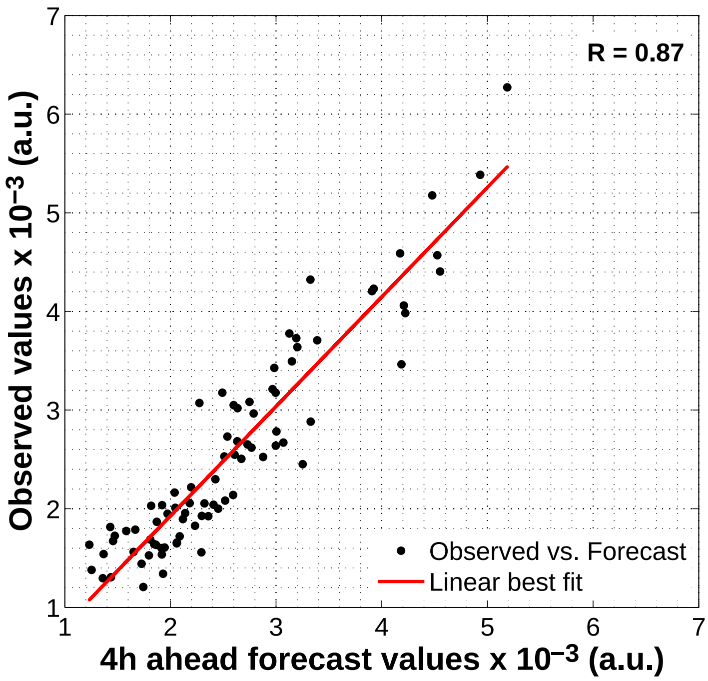

Figure 5.53: the scatter diagram of observed SR powers and the 4 hour ahead forecast values in the same period

Table 5.3: The performance table for different time horizons (H.O.D.U.: Highest Order of Difference Used) for the period of November–December 2004

Δt	05h	1h	2h	4h
H.O.D.U.	2	2	2	2
N.E. (%)	12	13	13	19
A.E. ($\cdot 10^{-3}$ a.u.)	0.30	0.32	0.31	0.46
C.C.C. (R)	0.94	0.91	0.88	0.86

Abbreviations: H.O.D.U.: Highest Order of Difference Used, N.E.: Normalized Error, A.E.: Absolute Error, C.C.C.: Cross Correlation Coefficient

5.4 Application of Fuzzy Neural Networks (FNN) on other Ionospheric Data as a Typical Independent Case Study

HF radio communication requires forecasting the ionospheric critical frequencies. Ionospheric F layer critical frequency, foF2, is a parameter designating the maximum usable frequency. In addition to diurnal, seasonal and solar variability of foF2, during geomagnetically disturbed conditions induced by solar storms, the physics of the ionosphere become more complex and non-linear, therefore the response of ionosphere to such disturbances need to be qualified and quantified for the system designers, operators and users. There are various models constructed to forecast the foF2 using different methods. For example, mathematical modeling using first physical principles, statistical models, data driven models. Although Ionospheric structure and foF2 are highly spatially variable, in addition to diurnal, seasonal and solar-cycle variations [31], the data-driven modeling, such as the Neural Network (NN) based modeling have been shown to be promising in modeling highly complex, nonlinear and time varying processes as the Ionospheric processes [45, 12, 57]. In particular, both multilayer neural networks [60] and fuzzy inference systems (FIS) [61] can approximate any real nonlinear function to an arbitrary degree of accuracy. Hence, they can be employed in complex processes of the real world, where a great amount of imprecision and uncertainty is encountered [48]. In this work a hybrid data-driven modeling approach is introduced. In particular, FNN approach is made to forecast the foF2 values during magnetically disturbed conditions. A new optimization algorithm, FUNCOM (Fuzzy Neural Optimization Method) is used in the training of the Neural Network [48, 49].

Despite the fact that foF2 is a crucial parameter of telecommunication there are limited number of ionosonde stations all over the world. Moreover, during disturbed conditions, at some of the ionosondes, the quality of measurements decrease and missing number of data increases. Thus, there have been attempts to generate foF2 instantaneous maps of Europe [31, 62, 63, 64].

The objective of this part of the work is to forecast foF2 values 1 hour in advance for a specified number of ionosondes during two of the strongest solar storms, the Halloween Storm which occurred between the 28^th and 30^th of October 2003 and the November 2003 Superstorm, which occurred on the 20^th of November. In order to achieve the task, a fuzzy feed-forward Neural Network (NN) model was constructed.

The dates for the construction of Fuzzy Neural Network are selected by their continuity and closeness to the period of October 2003 Halloween Storm in order to eliminate the variability of the inputs with the solar cycle. Considering also the seasonal changes, the data for foF2 is chosen at the last quarters of the years 2002, 2003 and 2004 from three ionosondes (Sofia, Juliusruh/Rugen and Chilton), of which the geomagnetic and geographic coordinates are tabulated in Table 5.4. Table 5.5 presents additional information on data coverage for training and validation phases. The Space Physics Interactive Data Resource (SPIDR) and The CCLRC Rutherford Appleton Laboratory (RAL) databases are used together to have a complete set of data for both foF2 and Kp indices [32, 65].

Table 5.4: Coordinates of Selected Ionosonde Stations

Stations	**G. Lat. (N)(^{o})**	**G. Long. (E)(^{o})**	**Gm. Lat (N)(^{o})**	**Gm. Long (E)(^{o})**
Chilton	51.6	358.7	48.4	77.9
Juliusruh	54.6	13.6	50.9	90.9
Sofia	42.7	23.4	37.0	96.6

Depending on the methods for the fuzzy rules, for this particular case, where a fuzzy neural network model is used to forecast the foF2 values, Mamdani type fuzzy inference system (FIS) is selected. Mamdani is one of the FIS types which is widely used by fuzzy system designers [50]. For this particular study a fuzzy NN model consisting of a fuzzy interference part with two rule spaces and two feedforward neural network models, quiet neural network model (qNN) and disturbed neural network model (dNN) is employed to forecast the one hour

Table 5.5: Input Data Coverage of the Fuzzy-Neural Network to forecast foF2 during Halloween 2003 storm

Dataset	**Year**	**Month**			
		Sept.	**Oct.**	**Nov.**	**Dec.**
Training	2002	—	1–20	—	—
	2004	24–30	1–12; 16–26	—	—
Operation	2003	26–30	1–13; 14–23; 29–31	12–26; 28–30	1–5

ahead values of foF2 values.

The fuzzy inference part of the model consists of three rules, decided by employing expert information on the foF2 values. The inputs to the fuzzy inference are the present 3-hour planetary magnetic activity index value, Kp ($Kp(k)$); its 3-hour previous value ($Kp(k-180)$); and trigonometric component of minute of day ($Sin((k/1440)*\pi)$), where "k" represents the present value of the minute of the day. The trigonometric component of the minute of the day gives a periodicity to the minute data and simply reflects the tendency of change in foF2 between the night and day times. For the sake of simplicity Mamdani type fuzzy rules with triangular and trapezoidal membership functions are used; the fuzzy sets are described by triangular and trapezoidal type membership functions. The fuzzy inference part gives the user the membership values, representing the firing strength of each rule. There are three logical fuzzy rules employed for the system, that is, depending on the present and 3-h previous values of Kp index and on the minute of the day, the time period which is decided to be geomagnetically disturbed or not, and the firing strength of the rules are calculated accordingly.

The neural network part of the model consists of 2 feed forward neural networks. The parameters of each NN are adapted by the optimization algorithm so that, the qNN gives information on the geomagnetically quiet time ($Kp \leq 3$) period and the dNN gives information on geomagnetically disturbed ($Kp > 3$) time period. The fuzzy inference part of the model gives 2 outputs, the membership function value corresponding to qNN (μ_q) and the membership function value corresponding to dNN (μ_d). In the defuzzification part of the model, the output of the model is determined using weighted average defuzzification method.

The firing strength of each NN is determined by the fuzzy rules and the defuzzified output gives the user the final result. The optimization algorithm employed is a constrained optimization algorithm during training process for fuzzy neural networks, namely FUNCOM, which is adapted from [48, 49] and explained in Chapter 4, Section 4.3.

The inputs to the neural network models are,

1. Present value of the foF2, $f(k) = foF2(k)$,
2. First Difference of the foF2, $\Delta_1(k) = f(k) - f(k-m)$,
3. Second Difference, $\Delta_2(k) = \Delta_1(k) - \Delta_1(k-m)$,
4. Relative Difference, $R\Delta(k) = \Delta_1(k)/f(k)$,
5. Cosine component of the minute, k, of a day, $Cm = -Cos(2 \cdot \pi \cdot k/1440)$
6. Sine component of the minute of a day, $Sm = Sin(2 \cdot \pi \cdot k/1440)$
7. Cosine component of the day, d, of a year, $Cd = -Cos(2 \cdot \pi \cdot d/366)$, and
8. Sine component of the day of a year, $Sd = Sin(2 \cdot \pi \cdot d/366)$

Among the various Neural Network structures the best configuration is found to be the one with one hidden layer with 10 hidden neurons. The general representation of the FNN model and the architecture of the feedforward NN models are shown in Figures 4.6 and 4.6 of Chapter 4 where FUNCOM algorithm is employed in the training part. In these Figures, the inputs to the fuzzy inference part and the feedforward neural network part are represented by $u_f(k)$ and $u(k)$ respectively, $y_d(k)$ and $y_q(k)$ represents the outputs of the feedforward neural networks, dNN and qNN and final defuzzified output is represented by y(k).

The fuzzy neural network model described is trained using the data consisting of both geomagnetically quiet and disturbed time periods. The training data covers the periods, 1-20 November 2004 which is a geomagnetically disturbed period and 24 September-12 October and 16-26 October 2004, corresponding to a geomagnetically quiet time period. Data is retrieved from three stations. The training lasted for 150 epochs, finally reaching a normalized error of 11%.

The trained fuzzy NN model was simulated using the data at the time period of Halloween storm of 2003 (26 Sep-13 Oct.; 14-23 Oct.; 29-31 Oct; 12-18 Nov.; 25-26 Nov.; 28 Nov-5

Dec) and particularly at the November 2003 Superstorm (12-24 Nov.) time periods. The data from three different stations were used to simulate the model and forecast the foF2 values one hour in advance for three different geomagnetic coordinates. Figures 5.54 to 5.65 show the simulation results of the forecast and observed values of foF2 for three stations for the time period of Halloween 2003 and November 2003 Superstorm. One can see from these figures that the observed and forecast values seem to be in good agreement. The scatter diagrams are good confirmations of the agreement between the observed and forecast foF2 values. At a confidence level of $\alpha = 0.05$ for the correlation coefficients, the forecast values are within the acceptable error limits and therefore are significant enough to be employed in practice.

Table 5.6: Forecast Performance Parameters for Different Stations for the Halloween 2003 storm Period

Stations/Performance	**Chilton**	**Juliusruh**	**Sofia**
Abs. Err. (MHz)	0.4	0.3	0.5
Norm. Err. (%)	10	9	8
Cr.corr. coeff. ($\cdot 10^{-2}$))	96	98	95

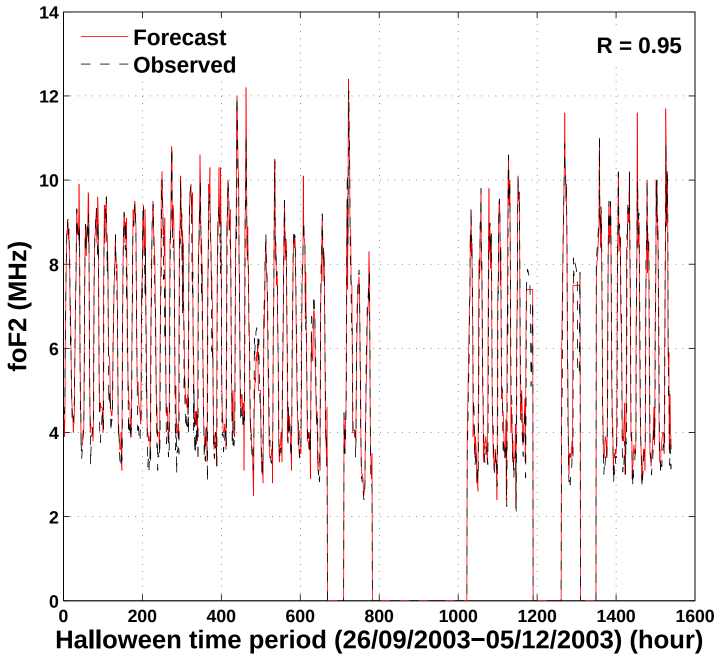

Figure 5.54: Superimposed are the observed nd 1-h in advance forecast value of foF2 for Sofia between 26 September and 5 December 2003

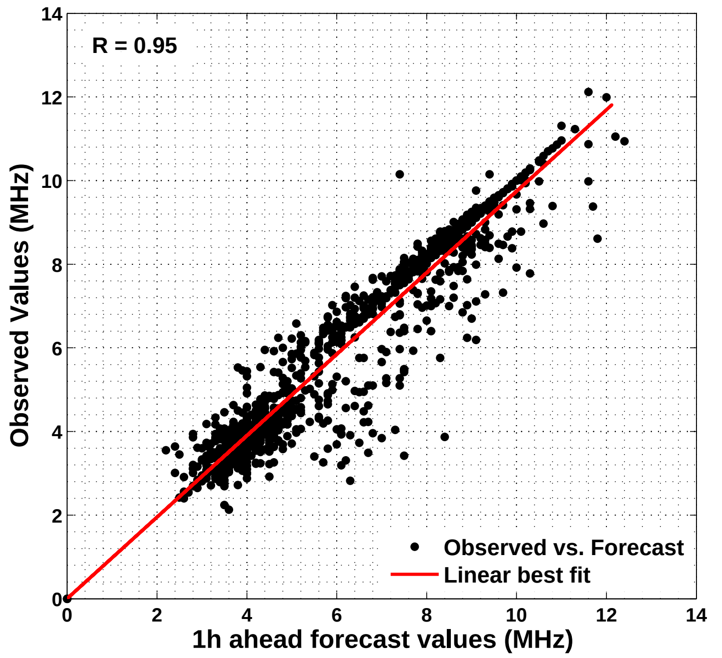

Figure 5.55: Scatter diagram of the observed and 1-hour ahead forecast foF2 values and the best fit line for Halloween 2003 time period for Sofia station

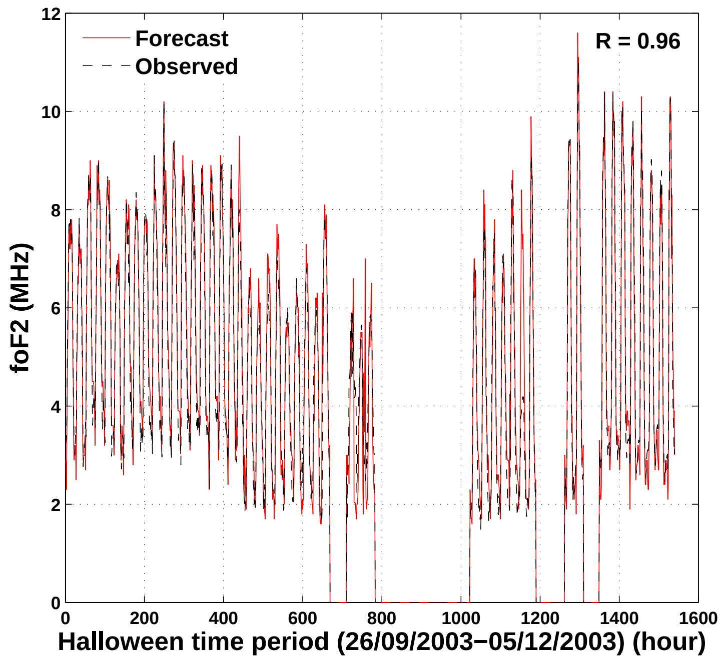

Figure 5.56: Superimposed are the observed nd 1-h in advance forecast value of foF2 for Chilton between 26 September and 5 December 2003

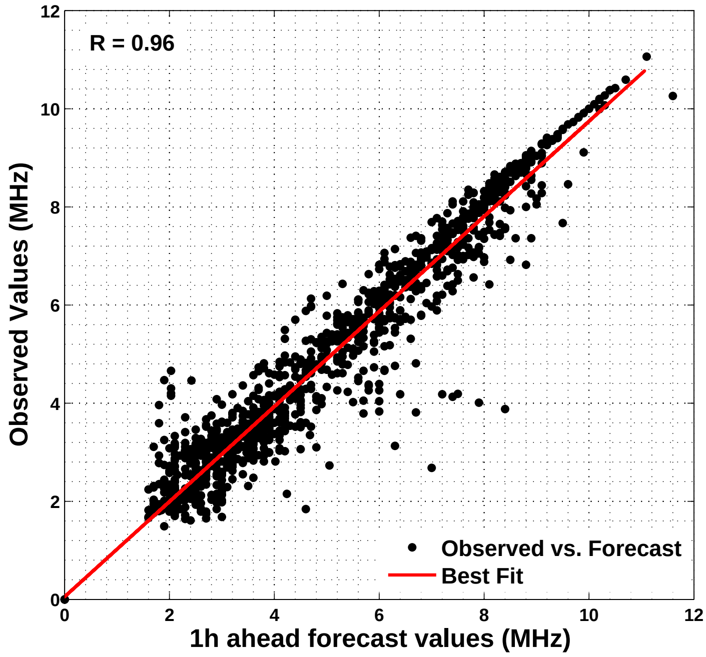

Figure 5.57: Scatter diagram of the observed and 1-hour ahead forecast foF2 values and the best fit line for Halloween 2003 time period for Chilton station

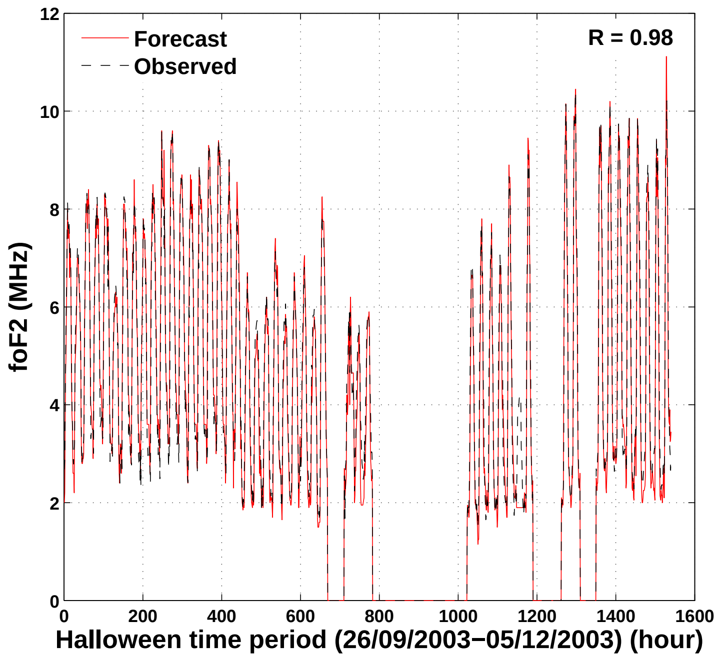

Figure 5.58: Superimposed are the observed nd 1-h in advance forecast value of foF2 for Juliusruh between 26 September and 5 December 2003

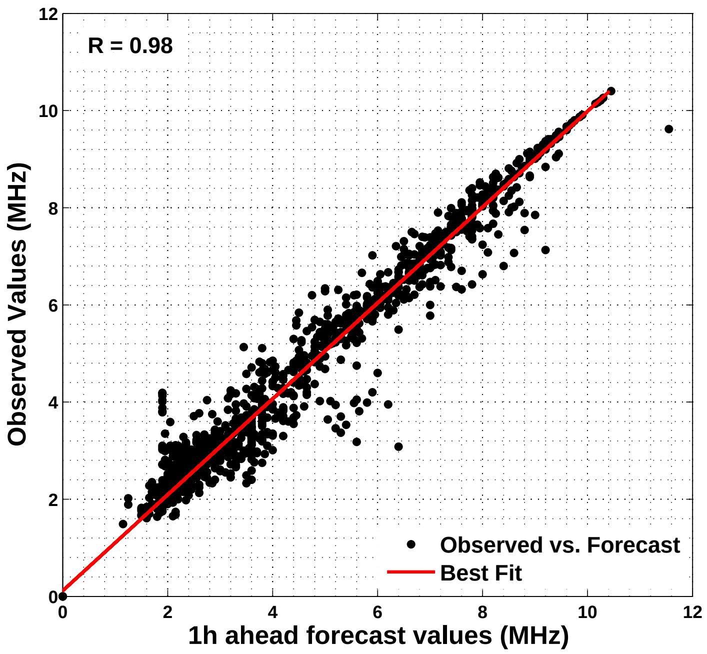

Figure 5.59: Scatter diagram of the observed and 1-hour ahead forecast foF2 values and the best fit line for Halloween 2003 time period for Juliusruh station

Table 5.7: Forecast Performance Parameters for Different Stations for the November 2003 Superstorm Period

Stations/Performance	**Chilton**	**Juliusruh**	**Sofia**
Abs. Err (MHz)	0.4	0.5	0.8
Norm. Err (%)	9	10	8
Cr.corr. coeff. ($\cdot 10^{-2}$))	98	98	98

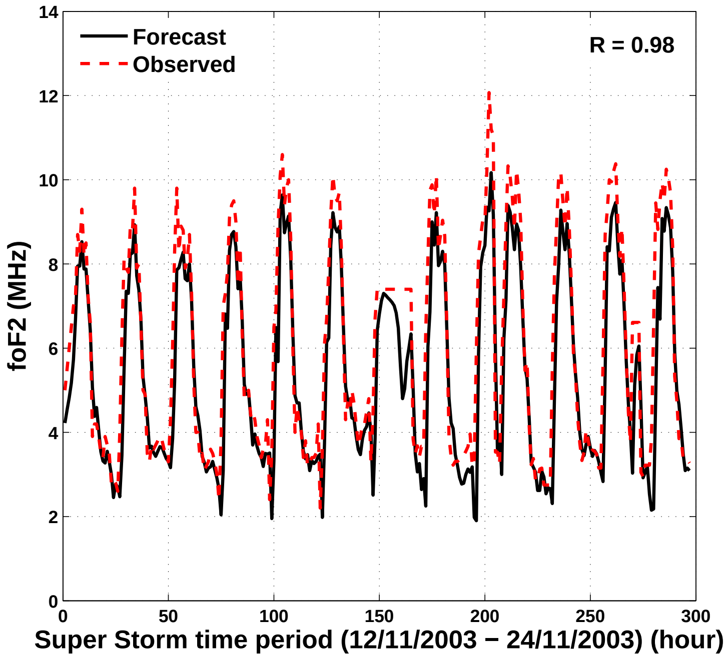

Figure 5.60: Superimposed are the observed nd 1-h in advance forecast value of foF2 for Sofia between 12–24 November 2003

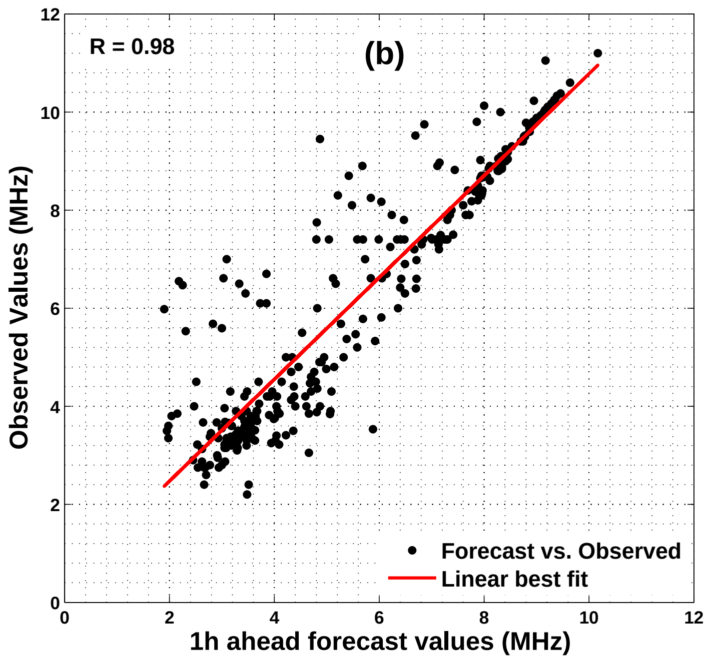

Figure 5.61: Scatter diagram of the observed and 1-hour ahead forecast foF2 values and the best fit line for Superstorm 2003 time period for Sofia station

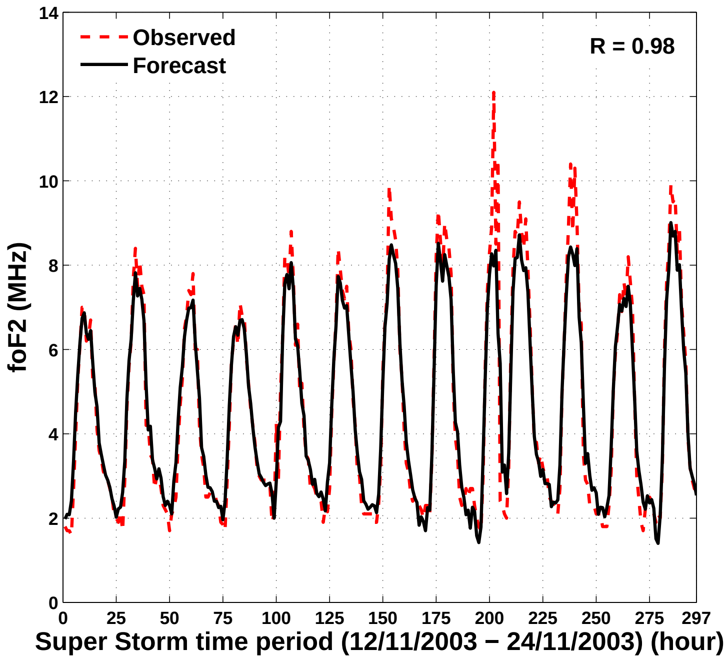

Figure 5.62: Superimposed are the observed nd 1-h in advance forecast value of foF2 for Chilton between 12–24 November 2003

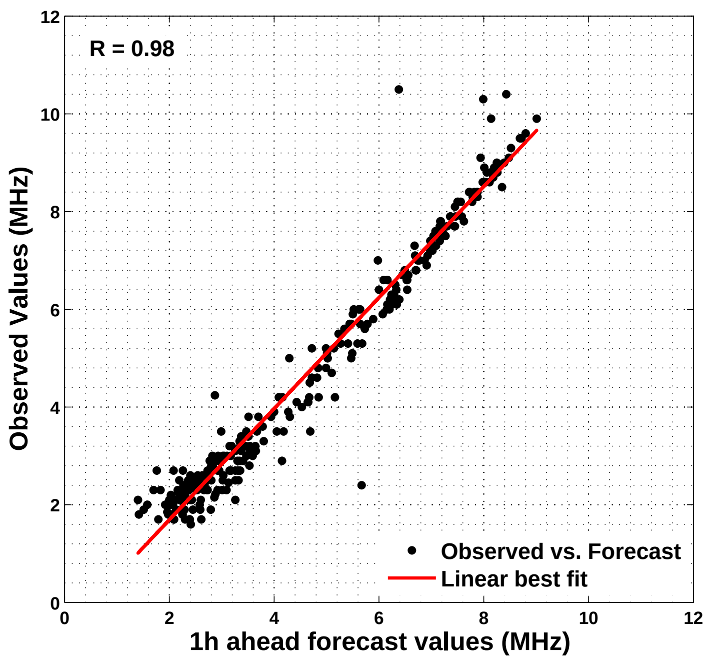

Figure 5.63: Scatter diagram of the observed and 1-hour ahead forecast foF2 values and the best fit line for Superstorm 2003 time period for Chilton station

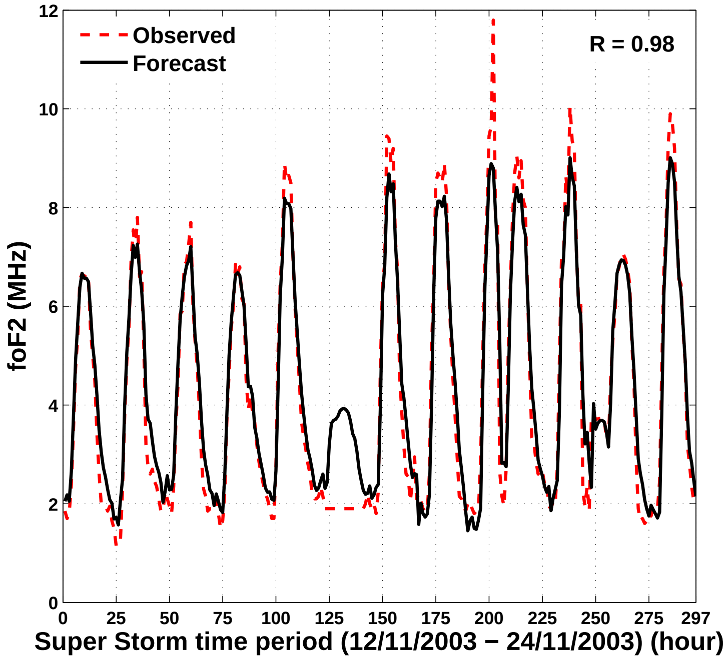

Figure 5.64: Superimposed are the observed nd 1-h in advance forecast value of foF2 for Juliusruh between 12–24 November 2003

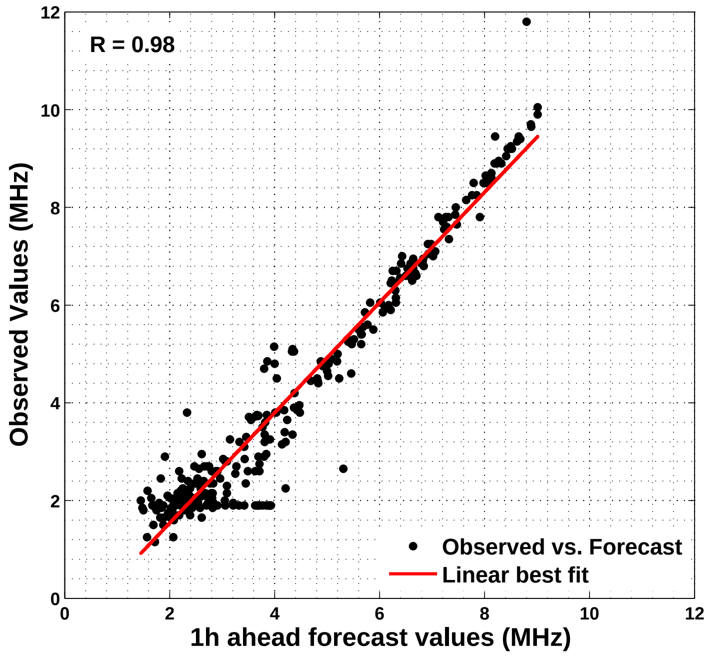

Figure 5.65: Scatter diagram of the observed and 1-hour ahead forecast foF2 values and the best fit line for Superstorm 2003 time period for Juliusruh station

To conclude, the simulation results show that the feedforward neural fuzzy system using the FUNCOM optimization algorithm is able to learn the shape of the nonlinearities in foF2 data during the disturbed geomagnetic activity. The results are good enough to employ in practice with a confidence level of $\alpha = 0.05$ for the correlation coefficients.

CHAPTER 6

CONCLUSIONS AND FUTURE WORK

As the technology began to improve further, and as it is a part of our lives now, the investigation of hazards of space weather to technology gained importance. In this work the characterization of SR parameters, improvement of a neural network model (METUNN) to forecast SR mode intensities and development of a fuzzy neural network model to forecast the Near Earth Space Processes have been the main objective.

In Chapter 1, ”Near Earth Space” and ”Space Weather” concepts and the importance of investigation of space weather effects on our daily lives are briefly introduced. Particular importance was given to ionosphere, since the ionosphreric phenomena called Schumann Resonances is the part of the main objective. In Chapter 2, some brief information of ELF band and some application areas were given. Formulation of the EM waves and SR were presented. In Chapter 3, the data used in this work were explained. Some detailed information on the data acquisition and the experimental setup were introduced.

In Chapter 4, the methods used to process the data were described in detail. It was decided that the non–parametric methods, especially Welch's periodogram analysis was the most suitable method to reveal the peak frequencies and powers of Schumann modes. In addition, the author has explained the theory behind neural network modeling, in particular feed–forward neural network modeling, which will serve our purposes the best for forecasting the Schumann Resonance intensities different time horizons in advance. Fuzzy neural network modeling using a new optimization algorithm [48, 49] which will be employed in the future studies was introduced as an alternative tool for an independent case study.

The significant results arose from this work may be summarized as follows;

In order to prepare the inputs for the METUNN, spectral analysis of the Şarköy SR data was conducted as a processing phase. The spectral analysis of the data revealed the diurnal variability on the frequencies and amplitudes of the first four SR modes. The result of this phase of study are listed as follows;

- A significance of input test was performed using a variety of input parameters to the model including some meteorological parameters. The results listed in Table 5.1 illustrated that both precipitable water and specific humidity together are significant inputs to the model.

- The selected model was tested for 2*h* of time step. Figures 5.23 and 5.24 showed that the model was able to forecast first mode SR intensities with a normalized percentage error of 13%.

- The selected model was tested for different time horizons of 0.5, 1, 2, 4, 6, 8, 10, 12, 18, 24, 30 and 36 hours. The FFT analysis of the operational period revealed the fact that 94% of the power belonged to the harmonics with period greater than 8*h*. At this phase of the work a new parameter, H.O.D.U, designating the higher order of time differences for the input, was introduced. This parameter is fed into the model to reflect the past history of the fSRmp.

- From the results listed in Table 5.2 it is observed that all the performance parameters were quite close to each other for forecast ranges of 0.5*h*, 1*h* and 2*h*. The cross correlation values of 2*h*, 4*h* and 6*h* ranges were also close while their absolute and normalized errors were somewhat different. After 6*h* of range the cross correlation coefficients were found to be less than 0.8.

- Furthermore, it was observed that beyond 6*h* range, the model is not so successful in catching the extreme values and the peak traces of forecast curves tend to follow a relatively invariant path independent of their actual values.

- Investigation of the results revealed that the forecast curves exhibit an in phase variation with the actual curves because of the fact that SR parameters have regular diurnal variations. It was observed that the accuracy model in catching an extreme value depends on the relationship between the meteorological parameters and the fSRmp. In other words, as the forecast range increases, the meteorological parameters and SR values become less reliable indicators of the peak values. Therefore, the model learns the diurnal variation pattern successfully for any time range, however it fails in following the extreme values as the forecast range increases.

The independent case study of Chapter 5 included forecasting ionospheric F2 layer critical frequency, foF2, which is a crucial parameter in telecommunication at high frequencies. The significant results found are listed as follows;

- The developed model was tested during two of the strongest Solar Storms, Halloween 2003 storm and November 2003 Super storm.
- The inputs for the fuzzy part of the model were selected by employing expert information.
- The introduced training algorithm (FUNCOM) is employed in order to transfer the training process into a constrained optimization problem and then solve the problem.
- The model results for 1 hidden layer with 10 hidden neurons are listed in Tables 5.6 and 5.7. It is observed that the model is able to catch the actual foF2 curves for geomagnetically quite times and need to be improved further for geomagnetically disturbed times. Nevertheless, even with this state of weights, the results are good enough to employ in practice with normalized percentage errors of order 10%.
- This problem may be solved in the future with the recurrent fuzzy neural network with a similar training algorithm, D-FUNCOM (Dynamical Fuzzy Neural Constrained Optimization Method) which is being developed by Mr. Emre Altuntaş.

In future, hopefully, the author of this thesis, will investigate the effects of Space Weather on our technology and aerospace technologies further. A number of new data driven modeling techniques will be employed to forecast the Near Earth Space processes such as recurrent fuzzy neural network modeling and evolutionary algorithm techniques. The forecasting of Near Earth Space processes will make us available to forecast the possible hazards of Space Weather on our technology and on aerospace applications.

REFERENCES

[1] A. P. Nickolaenko and M. Hayakawa. *Resonances in Earth-Ionosphere Cavity*. Kluver Academic Publishers, Dordrecht, Boston, London, 2002.

[2] C. Price and A. Melnikov. Diurnal, seasonal and inter-annual variations in the Schumann Resonance parameters. *Journal of Atmospheric and Solar Terrestrial Physics*, **66**:1179–1185, 2004.

[3] A. P. Nickolaenko, G. Sàtori, B. Zieger, L. M. Rabiniwicz, and I. G. Kudintseva. Parameters of global thunderstorm activity deduced from long-term Schumann Resonance records. *Journal of Atmospheric and Solar Terrestrial Physics*, **60**:387–399, 1998.

[4] Schlumberger Technology Corp. EMI Technology Center, California, USA. *MT24/LF System Operation and Maintenance Manual*, 2004.

[5] MATLAB, the language of technical computing. Version 7.0, 2004.

[6] NASA, living with a star program. http://lws.gsfc.nasa.gov/, last accessed on 17/07/2007.

[7] T. Gombosi. *Physics of the Space Environment*. Cambridge Atmospheric and Space Science Series. Cambridge University Press, Cambridge, USA, 1998.

[8] Construction and deployment of an ULF receiver for the study of Schumann Resonance in Iowa. http://www.iihr.uiowa.edu/projects/schumann/Index.html, last accessed on 17/07/2007.

[9] P. V. Bliokh and A. P. Nickolaenko. Global electromagnetic resonances. *Priroda*, **4**:3–15, 1986.

[10] Bell Laboratories. http://www.bell-labs.com/, last accessed on 17/07/2007.

[11] J. Richards. Propagation at VLF, VHF, ELF. Presentation at RSISE ANU.

[12] Y. Tulunay, E. Tulunay, and E. T. Senalp. The neural network technique - 1: A general exposition. *Advances of Space Research*, **33**:983–987, 2004.

[13] Jr. O. Mendes, A. M. da Costa, and M. O. Domingues. Introduction to planetary electrodynamics: A view of electric fields, currents and related magnetic fields. *Advances in Space Research*, **35**:818–828, 2005.

[14] N. J. Crosby, M. J. Rycroft, and Y. Tulunay. Overview of a graduate course delivered in Turkey, emphasizing the Solar–Terrestrial physics and space weather. *Surveys in Geophysics*, **27**:319–364, 2006.

[15] The National Oceanic and Atmospheric Administration (NOAA) Space Environment Center (SEC). http://www.sec.noaa.gov/, last accessed on 17/07/2007.

[16] J. M. Goodman. *Space Weather and Telecommunications*. Springer, USA, 2005.

[17] T. Pulkkinen. Space weather: Terrestrial perspective. *Living Reviews in Solar Physics*, **4**, 2007.

[18] W. G. Prolss. *Physics of the Earth's Space Environment, an Introduction*. Springer, Berlin, Germany, 2004.

[19] Oulu Space Physics Textbook, Solar wind–magnetosphere–ionosphere–thermosphere coupling. http://www.oulu.fi/ spaceweb/textbook/coupling.html, last accessed on 17/07/2007.

[20] P. V. Bliokh, A. P. Nickolaenko, and Yu. F. Filippov. *Schumann Resonances in the Earth–ionosphere cavity*. Oxford Press, New York, USA, 1980.

[21] L. J. Lanzerotti. Space weather effects on technologies. *American Geophysical Union Geophysical Monograph Series: Space Weather*, **125**:A2+, 2002.

[22] D. Porrat and C. F. Smith. Propagation at extremely low frequencies. Stanford University Electrical Eng. Dept. Star Laboratory, Stanford University, USA, February 10 2003.

[23] W. O. Schumann. On the radiation free self-oscillations of a conducting sphere which is surrounded by an air layer and an ionospheric shell. *Zeitschrift und Naturfirschung*, **7a**:149–154, 1952.

[24] G. Sàtori and B. Zieger. El Nino related meridional oscillation of global lightning. *Geophysical Research Letters*, **26**:1365–1368, 1999.

[25] E. R. Williams. Lightning and climate: A review. *Atmospheric Research*, **75**:272–287, 2005.

[26] C. Price and M. Asfur. Can lightning observations be used as an indicator of upper-tropospheric water vapor variability? *Bull. Amer. Meteor. Soc.*, **87**:291–298, 2006.

[27] C. Price, M. Finkelstein, Y. Tulunay, and E. Tulunay. Site investigation for future ULF/VLF station in turkey. ITU, UUBF, 2001.

[28] T. Cantwell. *Detection and Analysis of Low-Frequency Magnetotelluric Signals*. PhD thesis, Massachusetts Institute of Technology, Cambridge, Massachusetts, 1960.

[29] C. Price. Evidence for a link between global lightning activity and upper tropospheric water vapor. *Letters to Nature*, **406**:290–292, 2000.

[30] Nasa Climate Data Center (CDC). http://www.cdc.noaa.gov/, last accessed on 05/06/2007.

[31] P. A. Bradley, Juchnikowski, H. G., Rothkaehl, and I. Stanislawska. Instantaneous maps of the european middle and high-latitude ionosphere for HF propagation assessments. *Advances in Space Research*, **22/6**:861–864, 1998.

[32] SPIDR, Space Physics Interactive Data Resource. http://spidr.ngdc.noaa.gov/spidr/index.jsp, last accessed on 17/07/2007.

[33] M. H. Hayes. *Statistical Digital Signal Processing and Modeling*. John Wiley and Sons, 1996.

[34] S. M. Kay. *Modern Spectral Estimation*. NJ: Prentice Hall, Englewood Cliffs, 1988.

[35] P. Stoica and R. L. Moses. *Introduction to Spectral Analysis*. Prentice Hall, 1997.

[36] C. E. Shannon. A mathematical theory of communication. *Bell System Technical Journal*, **27**:379–423,623–656, 1948.

[37] H. Dym and H. P. McKean. *Fourier Series and Integrals*. Probability and Mathematical Statistics. Academic Press, USA, 1972.

[38] P. D Welch. The use of Fast Fourier Transform for the estimation of power spectra: A method based on time averaging over short, modified periodograms. *IEEE Trans. Audio Electroacoustics*, **AU-15**:70–73, 1967.

[39] E. Tulunay and Y. Tulunay. Data driven modeling in space weather applications. *COST 724 WG 4 Specific Paper on Data Driven Models Relevant for the Final Report*, 2006.

[40] E. Tulunay, E. T. Senalp, Lj. R. Cander, Y. K. Tulunay, and A. H. Bilge. Development of algorithms and software for forecasting, nowcasting and variability of TEC. *Annals of Geophysics*, **47**:1201–1214, 2004.

[41] D. E. Rumelhart, J. L. McClelland, and the PDP Research Group. *Parallel Distributed Processing, Explorations in the Microstructure of Cognition*, volume **1** of *Foundations, A Bradford Book*. The MIT Press, Cambridge, Mass, and London, 1986.

[42] J. H. Jackson. *Evolution and Dissolution of the Nervous System, Speech, Various Papers, Addresses and Lectures*, volume **2** of *Selected writings, Basic Books*. New York, 1958.

[43] A. R. Luira. *Higher Cortical Functions in Man*. Basic Books. Kluwer Academic / Plenum Publishers, New York, 2nd edition, 1966.

[44] S. Haykin. *Neural Networks: A Comprehensive Foundation*. Prentice-Hall, Inc., New Jersey, USA, 2 edition, 1999.

[45] E. Tulunay. *Introduction to Neural Networks and their Application to Process Control*, pages 241–273. Neural Networks, Advances and Applications, edited by E. Gelenbe. Elsevier Science Publishers B.V., 1991.

[46] U. Halici. Artificial neural networks. EE 543 Neurocomputers Lecture Notes, 2006.

[47] J. S. Wang and Y. P. Chen. A fully automated recurrent neural network for unknown dynamic system identification and control. *IEEE T. Circuits Syst.I, Regular Papers*, **53**:1363–1372, 2006.

[48] P. A. Mastorocostas and J. B. Theocharis. FUNCOM: A constrained learning algorithm for fuzzy neural networks. *Fuzzy Sets and Systems*, **112**:1–26, 2004.

[49] P. A. Mastorocostas and J. B. Theocharis. A recurrent fuzzy-neural model for dynamic system identification. *IEEE Transactions on Systems*, **31**:176–190, 2002.

[50] E. H. Mamdani and S. Assilian. An experiment in linguistic synthesis with a fuzzy logic controller. *International Journal of Man-Machine Studies*, **7(1)**:1–13, 1975.

[51] S. Z. Qin, H. T. Su, and T. J. McAvoy. Comparison of four neural net learning methods for dynamic system identification. *IEEE Trans. Neural Networks*, **3**:122–130, 1992.

[52] K. S. Narendra and K. Parthasarathy. Identification and control of dynamical systems using neural networks. *IEEE Trans. Neural Networks*, **1**:4–27, 1990.

[53] D. D. Sentman. Magnetic elliptical polarization of Schumann resonance. *Radio Science*, **22**:595–606, 1987.

[54] V. C. Mushtak and E. R. Williams. ELF propagation parameters for uniform models of the Earth ionosphere waveguide. *Journal of Atmospheric and Solar Terrestrial Physics*, **64**:1989–2001, 2002.

[55] V. C. Roldugin, Y. P. Maltsev, A. N. Vasiljev, A. V. Shvets, and A. P. Nickolaenko. Changes in the Schumann Resonance parameters during the solar proton event of 14 July 2000. *Journal of Geophysical Research*, **108 (A3)**:1103,2–1–2–7, 2003.

[56] E. R. Williams, V. C. Mushtak, and A. P. Nickolaenko. Distinguishing ionospheric models using Schumann Resonance Spectra. *Journal of Geophysical Research*, **111**:D16107, 2006.

[57] E. Tulunay, A. Kumluca, and S. Arslan. Relatve significance of inputs to a neural network with reference to juice extraction. *Proceedings of CONTROLO'98,* 3^{rd} *Portugese Conference on Automatic Control*, 9–11 Sep, 1998.

[58] L. A. Williscroft and A. W. V. Poole. Neural networks, foF2, sunspot number and magnetic activity. *Geophysical Research Letters*, **23**:3659–2662, 1996.

[59] Kalnay and Coauthors. The NCEP/NCAR 40–year reanalysis project. *Bull. Amer. Meteor. Soc.*, **77**:437–470, 1996.

[60] K. Hornik, M. Stinchcombe, and H. White. Multilayer feedforward networks are universal approximators. *Neural Networks*, **2**:359–366, 1989.

[61] L.-X. Wang and J. M. Mendel. Back-propagation fuzzy system as nonlinear dynamic system identifiers. *Proc. IEEE Int. Conf. on Fuzzy Systems*, pages 1409–1418, 1992.

[62] B. Lazo, A. Calzadilla, K. Alazo, M. Rodriguez, and J. S. Gonzalez. Regional mapping of f2 peak plasma frequency by spherical harmonic expansion. *Advances in Space Research*, **33**:880–883, 2004.

[63] I. Stanislawska, T. L. Gulyaeva, D. Altadil, Juehnikowski G. Bencze, P., Yu. N. Korenkov, G. Sole, and Z. Zbyszyniski. Instantaneous mapping of ionospheric characteristics using 5-minute measurements for the day of the total solar eclipse of 11 august 1999. *Phys. Chem. Earth (C)*, **26/5**:335–339, 2001.

[64] I. Stanislawska, D. Bureshova, and H. Rothkaehl. Stormy ionosphere mapping over Europe. *Advances in Space Research*, **33**:917–919, 2004.

[65] RAL, The CCLRC Rutherford Appleton Laboratory. http://www.ukssdc.ac.uk/wdcc1/iono_menu.html, last accessed on 17/07/2007.

APPENDIX A

Binary to ASCII Converter

Geomagnetic field data used in this work are originally stored an internal flash memory on a binary data format. Data are stored on binary files, which are comprised of fixed size (4096 bytes) header block and successive fixed size data blocks (1536 bytes long).

Figure A.1 shows the easy to use converter program employed in converting the binary files to ASCII format. The single files or multiple files are easily opened using the "select file" button and converted into ASCII format using the "convert" button.

The programming logic is to extract the header blocks of 4096 bytes and to convert 1536 bytes long fixed data blocks to ASCII format.

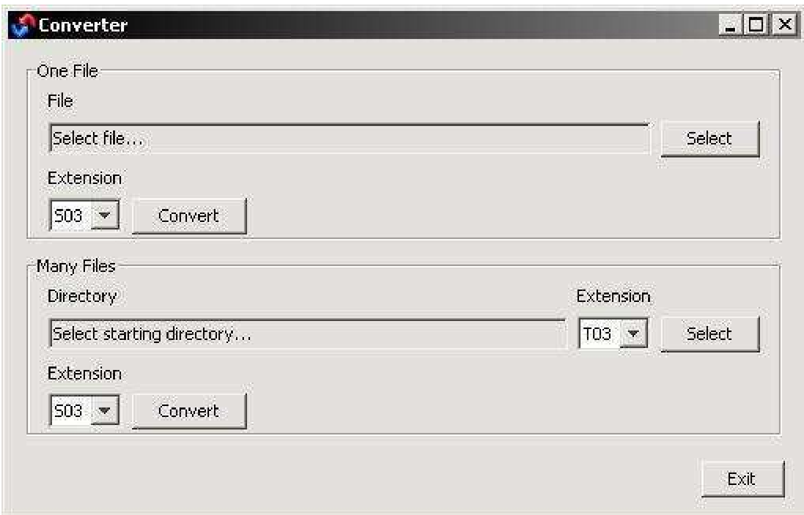

Figure A.1: The program that converts binary files into ASCII files

APPENDIX B

Diurnal Variations of Schumann Mode Characteristics

B.1 Diurnal Variations of Schumann Mode Powers

Figures B.1 and B.2 show the Monthly mean diurnal variations of the first four SR Mode powers obtained from the H_{ew} data during October 2004 for Gönen and Şarköy respectively. These figures allowed the author to compare the diurnal characteristics of Schumann mode powers for two different stations. Since the station coordinates are close to each other, the power values for two stations are close to each other.

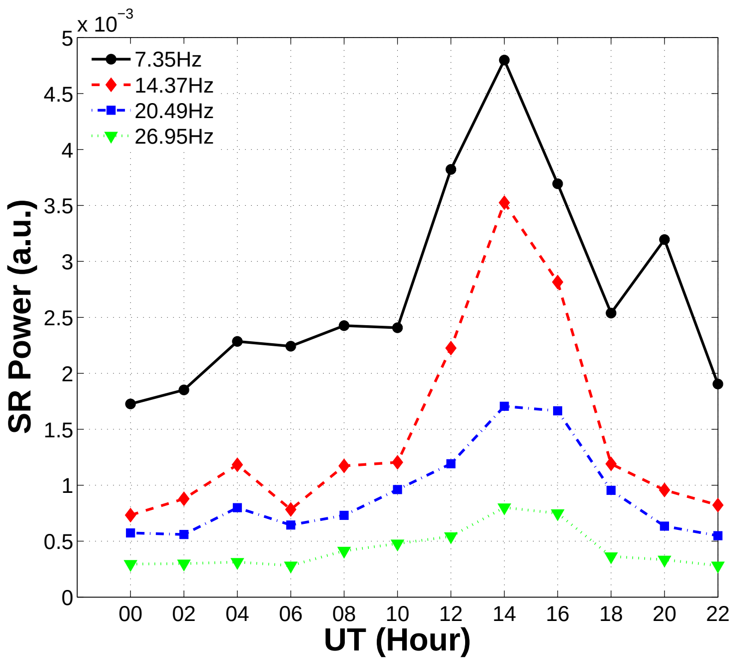

Figure B.1: Monthly mean diurnal variations of the first four SR Mode powers obtained from the H_{ew} data during October 2004 for Gönen

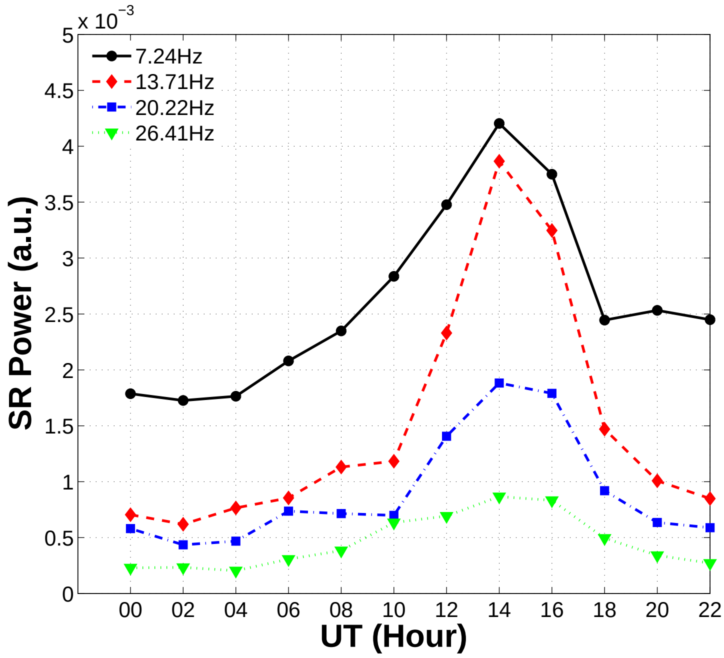

Figure B.2: Monthly mean diurnal variations of the first four SR Mode powers obtained from the H_{ew} data during October 2004 for Şarköy

B.2 Diurnal Variations of Schumann Mode Frequencies

Figures B.3 and B.4 show the Monthly mean diurnal variations of the first four SR Mode frequencies obtained from the H_{ew} data during October 2004 for Gönen and Şarköy respectively.

B.3 Diurnal Variations of Schumann Mode Q-Factors

Figures B.5 and B.6 show the Monthly mean diurnal variations of the first four SR Mode Q-factors obtained from the H_{ew} data during October 2004 for Gönen and Şarköy respectively.

B.4 Diurnal Variations of Schumann Mode Powers for the operation periods

Figures B.7 and B.8 show the Monthly mean diurnal variations of the first four SR Mode powers obtained from the H_{ew} data during selected days for operation periods in April 2005 and November–December 2004 for Şarköy respectively. These figures illustrate that the selected periods for operation cover good quality data.

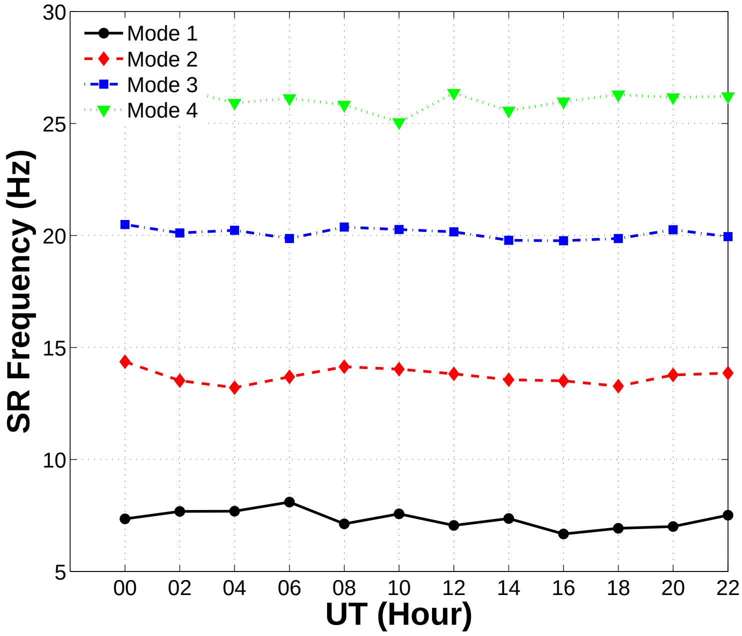

Figure B.3: Monthly mean diurnal variations of the first four SR Mode frequencies obtained from the H_{ew} data during October 2004 for Gönen

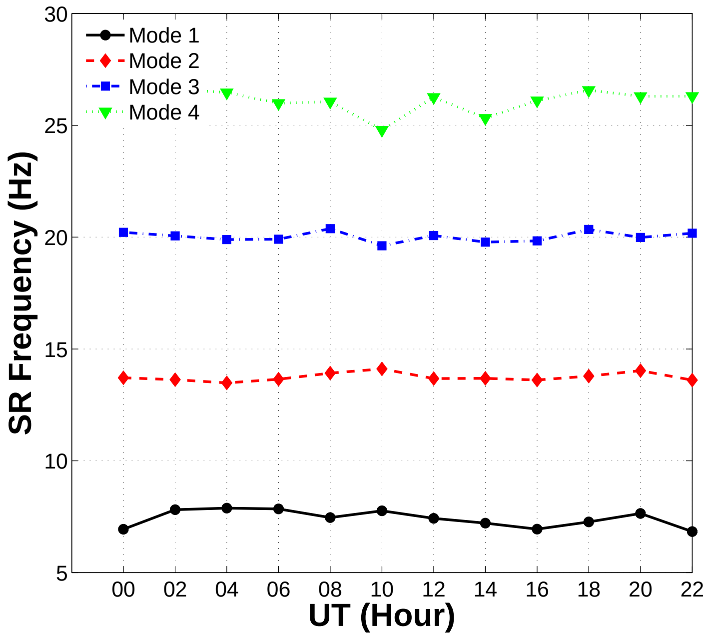

Figure B.4: Monthly mean diurnal variations of the first four SR Mode frequencies obtained from the H_{ew} data during October 2004 for Şarköy

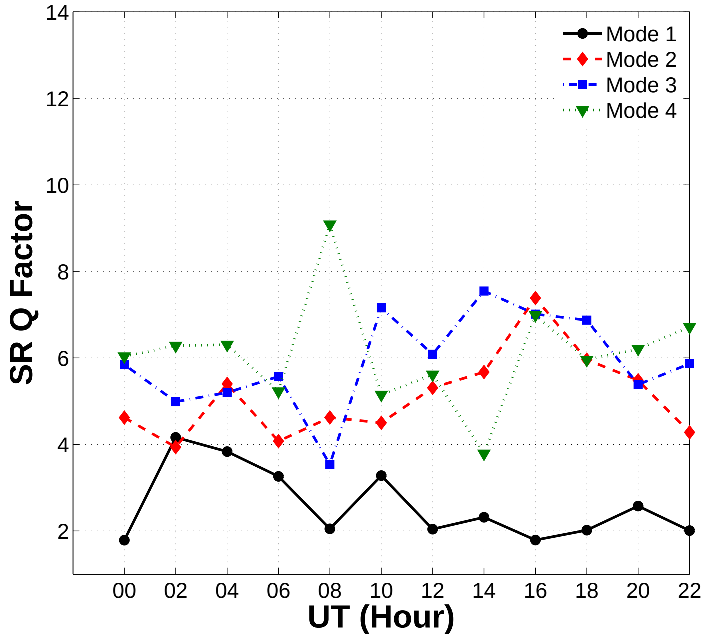

Figure B.5: Monthly mean diurnal variations of the first four SR Mode Q-factors obtained from the H_{ew} data during October 2004 for Gönen

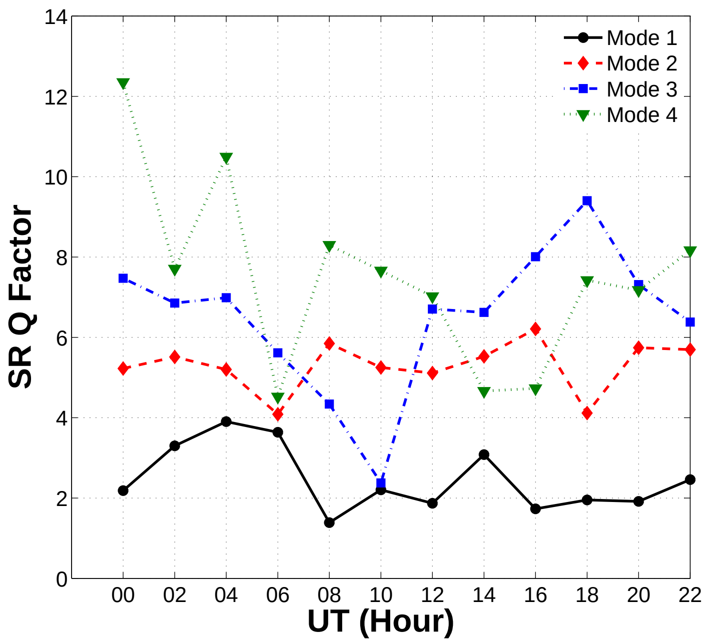

Figure B.6: Monthly mean diurnal variations of the first four SR Mode Q-factors obtained from the H_{ew} data during October 2004 for Şarköy

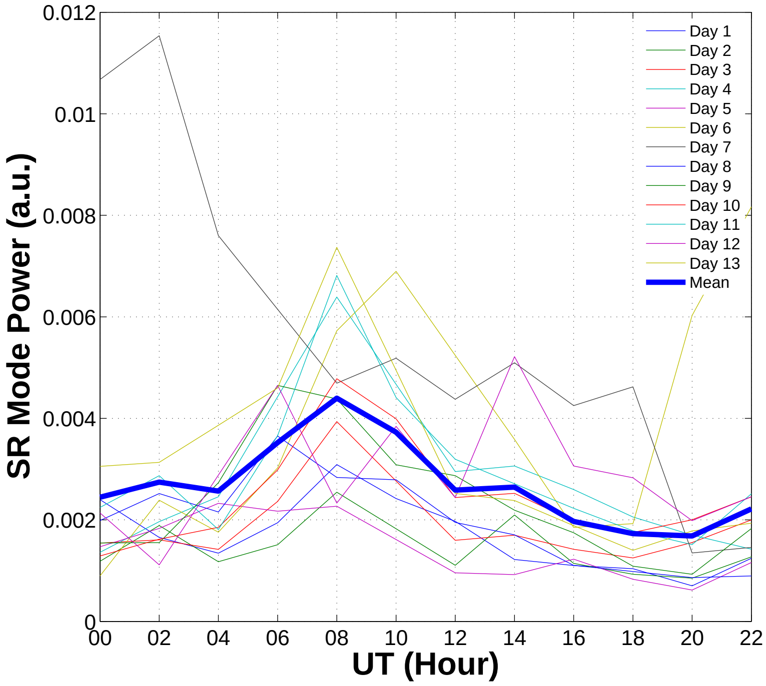

Figure B.7: Daily and monthly mean diurnal variations of the first four SR Mode powers obtained from the H_{ew} data during April 2005 for Şarköy

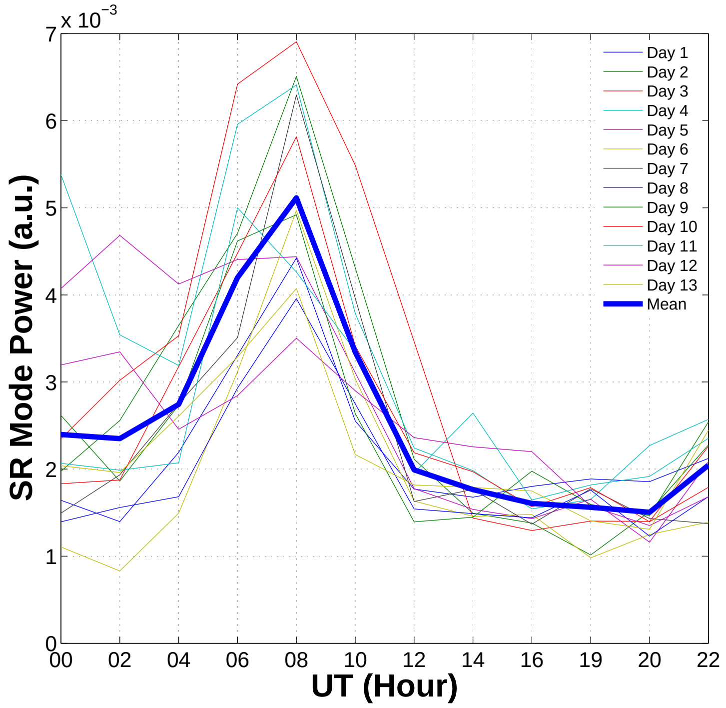

Figure B.8: Daily and monthly mean diurnal variations of the first four SR Mode powers obtained from the H_{ew} data during November–December 2005 for Şarköy

Figure B.9 shows the comparison of two sets of operation period data.

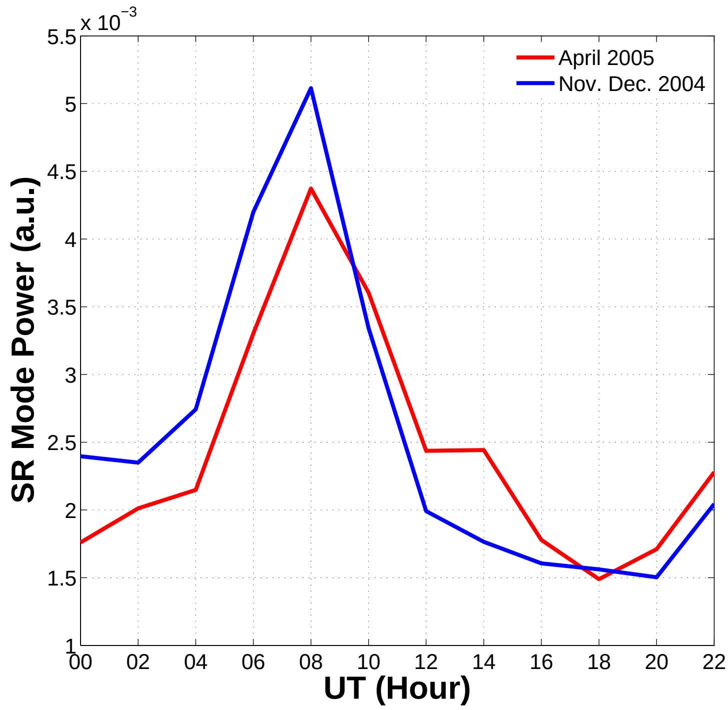

Figure B.9: Monthly mean diurnal variations of the first four SR Mode powers obtained from the H_{ew} data during November–December 2004 and April 2005 for Şarköy

APPENDIX C

Relevant Publications and Activities

C.1 International Publications

- “A Case Study on the ELF Characterization of the Earth-Ionosphere Cavity: Forecasting the Schumann Resonances, Journal of Atmos. And Solar-Terrestrial Physics (accepted, 2007).
  Yurdanur Tulunay, Emre Altuntaş, Ersin Tulunay, Colin Price, Tolga Çiloğlu, Erdem Turker Şenalp, Yıldırım Bahadirlar.
- “Near Earth Space Activities: A Turkish Initiative - ”IHY 2”, Sun and Geosphere, Vol 1(2), pp 56-60, 2006.
  Yurdanur Tulunay, Ersin Tulunay, Emre Altuntas, Tolga Yapici

C.2 International Conferences

- “The ELF Characterization of the Earth - Ionosphere Cavity: Forecasting of Schumann Resonances, International Symposium on Recent Observations and Simulations of the Sun-Earth System, 17-22 September 2006, Varna, Bulgaria.
  Emre Altuntas, Yurdanur Tulunay, Yildirim Bahadirlar, Ersin Tulunay, Erdem Turker Senalp
- “The ELF Characterization of the Earth-Ionosphere Cavity, 8th COST 724 MCM and WG Meetings, 27-30 March 2006, Antalya, Turkey.
  Yurdanur Tulunay, Yildirim Bahadirlar, Emre Altuntas, Ersin Tulunay
- “COST296 WG2.2 Activity Report : Radio Propagation Measurements During the 29 March 2006 Total Eclipse Week, 4th COST 296 MCM and WG meetings, 27-29 April

2006, Neustrelitz, Germany
Ersin Tulunay, Mike Warrington, Yurdanur Tulunay, Yıldırım Bahadırlar, Ahmet Serdar Turk, Tolga Yapici, Erdem Turker Şenalp, Emre Altuntas, Ozgur Sarı, Olcay Buyukpapuşcu

- "Neural Network Modeling in Forecasting the Near Earth Space Parameters: Forecasting of the Solar Radio Fluxes, COST 724 MCM, 10-13 Oct. 2005, Athens.
  Tulunay Y., Messerotti M., Senalp E.T., Tulunay E., Molinaro M., Ozkok, Y.I., Yapici T., Altuntas E., Cavus N.

- "A Hybrid Approach In Fof2 Forecast Mapping Including Disturbed Conditons, IFAC DECOM 2007, 17-18 May 2007, Cemse, (submitted, 2007).
  Emre Altuntas, Tolga Yapıcı,Yurdanur Tulunay, Ersin Tulunay, Zeynep Kocabas, Erdem Turker Senalp.

- "A Hybrid Approach In Fof2 Forecast Mapping Including November 2003 Superstorm, (to comply with the call of Prof. L. Cander on the SWWT Joint report, submitted, 2007).
  Emre Altuntas, Tolga Yapıcı,Yurdanur Tulunay, Ersin Tulunay, Zeynep Kocabas

- "Neural Network Forecasting Of Schumann Resonances In The Near Earth Space, Third European Space Weather Week (ESWW3), 13-17 November 2006, Royal Library of Belgium, Brussels, Belgium.
  Emre Altuntas, Yurdanur Tulunay, Yildirim Bahadirlar, Ersin Tulunay

- "foF2 Forecast 1-h in Advance During Disturbed Conditions by Using A Recurrent Fuzzy Neural Network, IRI/COST 296 Workshop, Ionosphere - Modelling, Forcing and Telecommunications, 10-14 July 2007, Prague, Czech Republic.
  Yurdanur Tulunay, Emre Altuntas, Ersin Tulunay, Zeynep Kocabas

C.3 National Conferences

- "Yer-İyonosfer Kovuk Değişiminin Schumann Rezonanslarına Dayali İncelenmesi, I. Ulusal Havacilik ve Uzay Konferansi, 21-23 September 2006, Ankara, Turkey,
  Emre Altuntas, Yurdanur Tulunay, Ersin Tulunay, Erdem Turker Senalp, Yildirim Bahadirlar

- ” Yer-İyonosfer Kovuk Değişiminin Schumann Rezonanslarına Dayali İncelenmesi, Kayseri VI. Havacılık Sempozyumu, 12-14 May 2006, Nevşehir, Turkey,
  Emre Altuntas, Yurdanur Tulunay, Yildirim Bahadirlar, Ersin Tulunay

C.4 Scientific Activities

- EU COST 724 Developing the Scientific Basis for Monitoring, Modelling and Predicting Space Weather, Researcher, 2005-
- EU COST 724 Short Term Scientific Mission (STSM); Number of Occurrence of Solar Radio Bursts, from 01/07/2006 to 08/07/2006, Astronomical Observatory of Trieste, Trieste, Italy.
  - Analysis of INAF Astronomical Observatory Solar Radio Flux Data
  - Improvement of the performance of the METU-NN modeling on predicting the number of occurrence of Solar Radio Bursts,
  - Preparation of the input for METU-NN

C.5 Outreach Activities

- COST 724 (Developing the Scientific Basis for Monitoring, Modelling and Predicting Space Weather) International Heliophysical Year (IHY) Project Outreach Activities
- EU SWEETS (Space Weather and Europe–an Educational Tool with the Sun) Project Outreach Activities